



HAL
open science

Grain boundaries in high temperature superconducting ceramics

Jeanne Gilberte Ayache

► **To cite this version:**

Jeanne Gilberte Ayache. Grain boundaries in high temperature superconducting ceramics. Philosophical Magazine, 2006, 86 (15), pp.2197-2243. 10.1080/14786430600640494 . hal-00513675

HAL Id: hal-00513675

<https://hal.science/hal-00513675>

Submitted on 1 Sep 2010

HAL is a multi-disciplinary open access archive for the deposit and dissemination of scientific research documents, whether they are published or not. The documents may come from teaching and research institutions in France or abroad, or from public or private research centers.

L'archive ouverte pluridisciplinaire **HAL**, est destinée au dépôt et à la diffusion de documents scientifiques de niveau recherche, publiés ou non, émanant des établissements d'enseignement et de recherche français ou étrangers, des laboratoires publics ou privés.



Grain boundaries in high temperature superconducting ceramics

Journal:	<i>Philosophical Magazine & Philosophical Magazine Letters</i>
Manuscript ID:	TPHM-05-Jun-0285.R1
Journal Selection:	Philosophical Magazine
Date Submitted by the Author:	13-Dec-2005
Complete List of Authors:	AYACHE, Jeanne; CNRS, CSNSM-IN2P3
Keywords:	superconducting materials, grain boundaries
Keywords (user supplied):	



Grain boundaries in high temperature superconducting ceramics

Jeanne AYACHE

Centre de Spectroscopie Nucléaire et Spectrométrie de Masse

CSNSM-CNRS-IN2P3, Bâtiment 108, 91405 Orsay Campus, France.

ayache@csnsm.in2p3.fr, Tel :33 01 69 15 52 19, Fax : 33 01 69 15 52 68

Abstract

The aim of this paper is to review the different types of grain boundaries found in $\text{YBa}_2\text{Cu}_3\text{O}_{7-d}$ superconducting ceramics which have been investigated over the past decade. A variety of samples covering a wide range of current density J_c values are examined including: classical bulk ceramics, melt-textured bulk ceramics, bulk and thin film bicrystals with specific orientations, thin films and single crystals. From electronic coupling, J_c is expected and found to decrease with increasing grain boundary (GB) misorientation. From the magnetic behaviour, the critical current density $J_c(H)$ is expected to increase with the number of pinning centres. The properties of the various types of GB's are discussed. All the studies reviewed lead to the conclusion that grain boundaries in YBCO materials cannot be understood without specific information about their local composition, structure and electronic state. They confirm that research on bicrystals is crucial for high-temperature superconductor development.

1. Introduction

Before 1987, most of the superconducting materials were characterized by a low critical temperature (T_c) close to liquid helium temperature (4.2K). They were metal or intermetallic compounds (Nb_3Ge for instance with $T_c=23\text{K}$). New high temperature superconducting cuprates (HTSC) with high T_c (above liquid nitrogen at 77K) based on lanthanides (Y, Ho, Nd for example), baryum and copper oxides were then discovered and found useful for industrial applications. Among them, $\text{YBa}_2\text{Cu}_3\text{O}_{7-d}$ (YBCO) ceramics, with a T_c close to 90K, was synthesized and extensively studied [1], [2]. At present, other compounds like Bi-Sr-Ca-Cu-O ($T_c =108\text{K}$) [2] and Tl-Sr-Ca-Cu-O ($T_c =135\text{K}$) [3] have become well known.

All these HTSC's are complex layered copper oxides, separated by CuO_2 layers which are

1
2
3 mainly responsible for the superconductivity. One of the applications of the superconducting
4 state makes use of the variation of the electrical resistance as a function of temperature, i.e. at
5 the critical temperature the resistivity drops suddenly to zero, due to condensation and
6 coupling between the superconducting electron Cooper pairs. The critical transport current
7 density (J_c) property dictates the type of application which can be achieved with a particular
8 superconductor. The value of J_c is proportional to the percolation paths, and depends strongly
9 on the quality of grain boundaries (GB's) in these ceramics. Understanding and controlling
10 GB's is found to be crucial for bulk material and thin film applications. Among the structural
11 defects formed in ceramics, GB's are especially interesting, because they act as Josephson
12 junctions [4], [5] and thus are good candidates for elucidating the mechanism of
13 superconductivity.
14
15
16
17
18
19
20
21
22
23
24
25
26
27
28
29
30
31
32
33
34
35
36
37
38
39
40
41
42
43
44
45
46
47
48
49
50
51
52
53
54
55
56
57
58
59
60

Jc is found to be maximum in single crystals and thin films and decreases with increasing GB content. Figure 1 shows a comparison of the different types of superconducting ceramics having been investigated over the past decade and of the corresponding ranges of Jc values measured for classical bulk ceramics, melt-textured bulk ceramics, bulk and thin film bicrystals with specific orientations, thin films and single crystals. The maximum Jc values obtained in synthesized bulk ceramics via solid-state diffusion do not exceed 10^3 A/cm² at 77K. When the number of GB's decreases, as in melt-textured ceramics, Jc increases ($10^4 < Jc < 10^5$ A/cm² at 77K) and reaches a maximum for some preferential orientations, as in epitaxial thin films ($10^6 < Jc < 10^7$ A/cm² at 77K). Beside the aspect of grain boundary transport, two fundamental steps of great importance make it difficult to obtain a material with good superconducting properties. The first difficulty is to achieve the formation of the single superconducting phase YBa₂Cu₃O_{7-d} in spite of the complex Y-Ba-Cu-O phase diagram [6]. The second difficulty lies in the phase transformations and their consequences on the superconducting properties and the oxygen content. One of the most important challenges for these ceramics is to obtain high quality grain boundaries for both general and special orientations. As an example, the short coherence length ($\xi = 1nm$) in these compounds requires very clean and sharp grain boundaries on the atomic scale. This is a limiting step for industrial applications. A high current density Jc value can be obtained inside a grain, due to the formation of twins as a result of the tetragonal to orthorhombic transition from high to low temperatures. On the other hand, a very low GB current density Jc can also be found, depending on the GB quality (clean versus degraded) and on the species involved.

2. Superconducting properties and their consequences for applications

A determining characteristic for HTSC's is their magnetic behaviour at the critical temperature Tc. They are characterized by the coexistence of superconducting and non-superconducting areas in the sample between the two critical magnetic fields Hc₁ and Hc₂. Such zones, resulting from the penetration of the applied magnetic field (H_{appl}), are described as vortex centres. Each of them carries a magnetic flux H. As a result, supercurrents are produced around each vortex, leading to the expulsion of the magnetic flux (Meissner effect). The resulting critical current density Jc is proportional to the number of pinning centers; the higher the number of vortices, the higher is the critical density Jc. Consequently, structural defects like point defects, dislocations, GB's and interfaces, will act as pinning centers and favour the increase of Jc due to the pinning energy dissipation. This property will compensate for the Jc limiting effect of weak-link coupling at grain boundaries. Consequently, GB Jc

1
2
3 values can be deduced from hysteresis loop magnetic measurements at low magnetic fields
4 (see section 5).

5
6 Generally, properties of devices based on GB Josephson junctions are strongly influenced by
7 the GB microstructure, due to the tunneling phenomenon itself, and also due to the presence
8 of a thin interface layer between two superconductors. This layer can have either normal
9 metal (S/N/S), insulating (S/I/S) or weakly superconducting properties. The superconducting
10 state of Cooper pair electrons across the interface is characterized by a pseudo-wave function
11 which depends on the phase ΔF of the superconducting order parameter Δ (OP). The
12 Josephson effect is very sensitive to the phase shift ΔF of this order parameter ($J_c = J_1 \sin \Delta F$).
13 For conventional low T_c superconductors, the OP is characterized by « s-wave symmetry »
14 with isotropic properties. As a result, phase and current are both constant. For HTSC's, the OP
15 presents a « d-wave symmetry » characterized by anisotropic properties and an internal phase
16 whose value depends on crystallographic orientation, in the same way as the current $I_c =$
17 $f(\Delta F)$ does. This latter is maximum only along some crystallographic orientations and null
18 outside. This characteristic is fundamental for the understanding of GB properties. Figure 2
19 schematizes a S/I/S junction with its characteristics for both types of superconducting
20 mechanisms. In low- T_c superconductors (LTS) the coherence length $\xi = 10^2 - 10^3$ nm is large
21 and isotropic, compared to HTSC's for which ξ is of the order of the interatomic d-spacing
22 ($\xi \approx 1$ nm) and anisotropic. Such a small value makes the OP amplitude and phase very
23 sensitive to the effect of a local structural change. Consequently, any change in GB
24 misorientation on the atomic scale will strongly affect the coupling between the two grains,
25 leading to a local decrease of J_c , as shown for bicrystal thin films (see section 8).

26
27 Thus, it is the grain boundary misorientation which controls the macroscopic J_c characteristic,
28 due to decreasing coupling between the two grains. The higher the misorientation angle, the
29 lower the coupling is expected to be. Hence, J_c is expected to have a defined value for a
30 specific misorientation between the two grains. High angle grain boundaries (HAGB) act as
31 Josephson junction weak-links. Consequently, a HAGB in the microstructure introduces a
32 network of weak-links (corresponding to regions of reduced J_c) into a superconducting path
33 which otherwise would have J_c characteristics appropriate for applications. Nevertheless, it
34 was shown that some HAGB's are strongly coupled, leading to rather good properties as in the
35 BSCCO system, although YBCO ceramics show a weak-link character with locally oxygen
36 deficient GB areas. It has become increasingly clear from electromagnetic measurements and
37 microstructural studies that weak-link boundaries are heterogeneous on various scales. The
38 characteristic properties of Josephson junctions, like weak-links, include a strongly magnetic
39 field dependent $J_c(H)$ which can decrease by more than an order of magnitude for weak fields
40
41
42
43
44
45
46
47
48
49
50
51
52
53
54
55
56
57
58
59
60

of just a few (1-10) millitesla. Such $J_c(H)$ characteristics clearly pose a serious problem for magnetic applications (energy storage systems, motors, generators,...). As a result, a great number of HAGB's represent an obstacle to the development of bulk materials for such applications. Improvement of the J_c limiting effect of weak-link coupling at grain boundaries can be achieved, either by improving the J_c of individual grain boundaries, or by texturing the materials in order to reduce the number of weak-link grain boundaries in the current path. The high sensitivity of J_c to weak magnetic fields, at grain boundary Josephson junctions, enables HTSC applications in electronic materials and particularly in thin films (squids).

The anisotropy of coherence length values in the YBCO superconducting plane ($\xi_{ab} = 1-2\text{nm}$) and in the c-axis direction ($\xi_c = 0.3\text{nm}$) leads to a dependence of various superconducting properties on the crystallographic orientation of the sample. Based on the $d_{x^2-y^2}$ symmetry [7], [8] of the superconducting order parameter, a strong coupling is expected along [100] and [103] orientations, while [001] and [110] will present a weak coupling. Thus, as schematized in figure 3, only some orientations will carry the supercurrent. Among them, GB's containing (001) superconducting planes will be the most favourable.

From electronic coupling, it can be expected that J_c will decrease with increasing GB misorientation. This effect is used to study Josephson junction applications based on thin films. From the magnetic behaviour, the critical current density $J_c(H)$ is expected to increase with the number of pinning centres, such as structural defects (point defects, dislocations, twins, clean interfaces). This particular property is used for high current transport applications in bulk ceramics. Among these cuprates, YBCO is the one that has been most extensively studied in bulk ceramics, thin films and heterostructures. Because of its particular interest, YBCO has been chosen as a model for understanding structure and superconductivity mechanisms.

The aim of this paper is to review the different types of grain boundary configurations and properties found in the YBCO system for bulk ceramics, melt-textured ceramics, thin films, bicrystals and single crystals used in the field of superconduction research and applications.

3. YBaCuO system properties and their consequences on grain boundary structure

3.1. Structure and properties

YBCO superconducting ceramics, like almost all HTSC, have a complex layered structure of perovskite blocks containing one or a few CuO_2 layers which are currently considered to be mainly responsible of the superconductivity. In these layers, the copper atoms form a square network, whereas the oxygen atoms are placed along the copper-oxygen chains (fig. 3a). As

1
2
3 $\text{YBa}_2\text{Cu}_3\text{O}_{7-d}$ has an orthorhombic structure based on that of perovskite oxides, it belongs to
4 the class of compounds displaying, for copper atoms, a mixed valence which leads to a
5 flexible chemistry. Another particular aspect of this system is the possible variation in
6 cationic and oxygen stoichiometry.
7
8
9

10 The formation of the YBCO superconducting phase (also called the (123) phase referring to
11 the cationic content in Y, Ba, and Cu atoms) involves a second order reaction transforming
12 the high temperature tetragonal insulating $\text{YBa}_2\text{Cu}_3\text{O}_6$ phase into the low temperature
13 orthorhombic superconducting structure. The crystallographic structure of YBCO strongly
14 depends on oxygen stoichiometry. The lower O_d , the higher is T_c . Its maximum value is
15 obtained for an oxygen deficiency $d = 0.03$. For $d = 1$, the structure becomes tetragonal
16 corresponding to an insulating material. Within this range, crystal structure and physical
17 properties undergo changes. Two orthorhombic structures have been characterized, called
18 "Ortho I" and "Ortho II". The first one refers to the fully oxygenated superconducting phase.
19 The second one contains vacancies along the O-Cu-O chains and particularly one oxygen
20 vacancy every two structural unit cells. The first one corresponds to an oxygen content in the
21 range O_7 - $O_{6.9}$ with a critical T_c remaining at 91K. The second one is characterized by an
22 oxygen content of $O_{6.6}$ or $O_{6.7}$, for which T_c drops to a plateau at 60K and finally to zero
23 between $O_{6.5}$ and $O_{6.4}$. These various oxygen concentrations and related YBCO structures are
24 summarized in Table 1. For special oxygen contents ($0.15 < d < 0.6$), various types of oxygen
25 vacancy ordering occur. They have been extensively studied by Transmission Electron
26 Microscopy (TEM) and electron diffraction patterns by Alario-Franco et al [9, 10]. Other
27 authors [11, 12] give numerous details on oxygen vacancy ordering near $O_{6.5}$. A review of
28 YBCO and its derived structures can be found in reference [13]. These experimental results
29 are in good agreement with theoretical calculations reported by Ceder [14] and Matic et al
30 [15] and more recent studies based on first principle calculations which predict all possible
31 oxygen vacancy orderings [16].
32
33
34
35
36
37
38
39
40
41
42
43
44
45
46
47

48 Figure 4 shows that lattice parameters change as a function of oxygen deficiency d for various
49 oxygen partial pressures [6]; note the change of the transformation temperature from 798K to
50 943K. This corresponds to an oxygen gain along the Cu-O chains of the tetragonal structure
51 (fig.3 and fig.4). It generates an increasing strain in the crystal due to the simultaneous
52 increase of lattice parameter b and decrease of lattice parameter a . Twins are formed and
53 induce stress relaxation. The higher the number of twins formed, the higher is the stress.
54 Twins are grain boundaries of special symmetry lower than that of the single crystal. Due to
55 their origin, they are found in all superconducting YBCO crystals, bulk ceramics, melt-
56 textured ceramics and thin films. Their presence increases J_c inside each grain, because they
57
58
59
60

act as pinning centres for the vortices. Twins are not the subject of this review and will not be described here.

For Peer Review Only

1
2
3
4
5
6
7
8
9
10
11
12
13
14
15
16
17
18
19
20
21
22
23
24
25
26
27
28
29
30
31
32
33
34
35
36
37
38
39
40
41
42
43
44
45
46
47
48
49
50
51
52
53
54
55
56
57
58
59
60

3.2. Phase diagram and stoichiometry

The important characteristic in the Y-Ba-Cu-O system is the non-congruent melting behaviour of the $\text{YBa}_2\text{Cu}_3\text{O}_{7-d}$ compound which favours the formation of secondary phases such as CuO, Y_2O_3 , BaO, BaCuO_2 and Y_2BaCuO_5 . The cationic non-stoichiometric (123) phase was observed in many RBCO ceramics, as well as secondary phases with specific properties. An understanding of the phase diagram has been mainly sought in order to determine the conditions of formation of the (123) phase and that of the secondary phases which also affect the physical properties of the bulk and of the interfaces. These secondary phases are formed outside of the thermodynamic growth conditions of the (123) superconducting phase. Cationic non-stoichiometry can be understood from the complex Y-Ba-Cu-O ternary phase diagram associated to the BaO- Y_2O_3 -CuO system (fig. 5). The diagram contains different domains of coexistence of solid-solid and solid-liquid phases. It shows the most likely domains for non-superconducting secondary phases to be (132), (211), beside the (123) phase. Among the secondary phases formed out of equilibrium, one may find barium, copper oxides or deficiency phases which are not superconducting such as (234), (235), and (113) [17], [18] and [19]. These authors observed in various ceramics synthesized by classical sintering, like RBaCuO (R=Y and Ho), a large variety of cationic non-stoichiometric ceramics. The (123) superconducting phase can be formed either by solid-solid diffusion (close to the domain of the (132) phase) or by solid-liquid diffusion in the region of the (211) phase. Depending on thermodynamic conditions, the resulting (123) phase will have specific microstructures and properties. At high temperature, the YBCO phase decomposes (above 1233K), due to non-congruent melting. Depending on oxygen partial pressure, solid-solid diffusion takes place between 1193K and 1233K. Grain growth governed by solid-solid atomic diffusion should lead to clean grain boundaries. Between the domain of BaCuO_2 -CuO and the (211) region, there is formation of a liquid with the diffusion governed by a liquid-solid process. At still higher temperatures near the peritectic reaction ($T=1288\text{K}$ in atmospheric conditions) YBCO decomposes in a liquid-rich phase containing CuO, BaCuO_2 and (211) precipitates. During this step, solid-liquid diffusion occurs leading to dissolution of the (211) precipitates into the liquid. This reaction is used to grow melt-textured ceramics. Grain growth governed by solid-liquid diffusion can lead to grain boundaries with secondary phases due to recrystallization of the liquid. This will be detailed in the section dealing with grain boundaries in melt-textured ceramics (see section 6).

The role of oxygen partial pressure should also be stressed in connection with the structural phase diagram. This diagram highlights the effect of oxygen partial pressure and of oxygenation temperature on the formation of the (123) oxygen stoichiometric phase, as

1
2
3 reported in figure 6. In particular, it shows the narrowness of the domain in which the
4 optimum oxygen content for the (123) phase is achieved. It can be noticed that both the
5 oxygen content at the orthorhombic-tetragonal transition and the transition temperature
6 decrease with decreasing oxygen partial pressure [6].
7
8

9
10 Finally, the complexity of this system makes intrinsically difficult the formation of a single
11 YBCO phase with oxygen and cationic stoichiometry. Improving YBCO growth has led to a
12 better knowledge of the structures and superconducting properties. As a consequence, an
13 increasing number of applications have been developed with bulk ceramics (for high current
14 transport), thin films (electronic device applications, squids) and heterostructures
15 (ferroelectric device applications, hard memories, ...).
16
17
18
19
20
21

22 **4. Grain boundaries in bulk ceramics**

23
24 Conventional ceramic sintering leads to a current density with a maximum value
25 $J_c=10^3 \text{ A/cm}^2$ at 77K (fig. 1) which is one thousand times less than that obtained for thin films
26 and single crystals ($J_c=10^6 \text{ A/cm}^2$). This large difference has various origins :

- 27 (i) The strong dependence of J_c on crystallographic orientation which is due to the
28 intrinsic anisotropic properties of the YBCO structure;
- 29 (ii) The oxygen content due to oxygen self-diffusion;
- 30 (iii) The oxygen content dependence on GB misorientation;
- 31 (iv) The quality of the grain boundaries, either clean or damaged;
- 32 (v) Last but not the least, the type of processing used to make bulk samples ready for
33 applications and leading to high quality GB's.

34
35
36 All these parameters are interacting simultaneously inside the grains and for each GB in the
37 ceramic. Therefore, J_c results from a combination of these phenomena.
38
39
40
41
42
43
44
45

46 **4.1. Oxygen diffusion as the limiting step for grain boundary properties in polycrystals**

47 An important challenge for obtaining good superconducting properties is to control the
48 elaboration process in order to reach the maximum oxygen content $O_{6.9-O_7}$. This problem
49 can be dealt with by considering oxygen self-diffusion in ceramics. Sabras et al [20]
50 investigated oxygen self-diffusion and its effects on grain boundary oxygen content by means
51 of Secondary Ion Mass Spectroscopy (SIMS). From diffusion profiles using oxygen O^{18} as a
52 tracer and from oxygen ion images, these authors found a heterogeneous distribution of the
53 tracer in the material, as well as an influence of microcracks on oxygen diffusion. On
54 polycrystalline ceramics exhibiting various grains sizes and an inhomogeneous grain size
55 distribution, they find an oxygen diffusion coefficient along grain boundaries of the same
56
57
58
59
60

1
2
3 order as in the bulk. Figure 7 depicts these experimental results and those found in the
4 literature. Figure 7a shows oxygen diffusion depth profiles on a sample polished according to
5 a small angle ($\alpha = 1.56^\circ$, $T = 823\text{K}$, $p_{\text{O}_2} = 22\text{kPa}$). It exhibits the presence of microcracks in
6 the ceramic. In Figure 7b an ion image obtained from O^{18} species shows the heterogeneous
7 distribution of the tracer in the material, as well as the influence of microcracks on the
8 oxygen diffusion. The results reported in references [20], [21], [22] are gathered on Figure 7c
9 where Arrhenius plots of oxygen self-diffusion are drawn, corresponding to Arrhenius plots
10 of volume and GB diffusion along the (ab) planes and parallel to the c axis in single crystals.
11 All these data are in general agreement with the oxygen diffusion behaviour in a ceramic,
12 suggesting that oxygen diffusion in a polycrystal is clearly governed by GB diffusion. This
13 latter is the limiting step, because the diffusion coefficient in the CuO_2 superconducting (ab)
14 planes is 10^6 times larger than along the c axis i.e. the direction perpendicular to the (001)
15 superconducting planes. This strong anisotropy of diffusion was observed and quantified for
16 the first time on single crystals by Rothman et al [21] and on polycrystals by Routbort and
17 Rothman [23].

18 An additional anisotropy of oxygen diffusion exists in the (ab) planes : the faster diffusion
19 being along the b axis, i.e. along the O-Cu-O chains which carry the oxygen vacancies.
20 Therefore, the anisotropic oxygen diffusion in the (001) planes and along the [001] direction
21 of the lattice will strongly affect oxygen diffusion inside each grain of the ceramic during
22 processing. Therefore, the sample geometry will strongly affect the final properties of the
23 ceramics. This explains the smaller critical density values found in bulk samples, compared to
24 thin films which are deposited according to a favourable orientation.

42 **4.2. Sintering parameters**

43 Generally, sintering requires a high temperature step for the growth, followed by cooling to
44 room temperature. In these conditions, the (123) phase obtained is not superconducting and is
45 generally oxygen deficient. It requires a second step of annealing around 823K in order to
46 optimize the oxygen content. Even if the initial powder is stoichiometric, the synthesized(123)
47 phase contains oxygen vacancies. Consequently, there may be local changes in the
48 microstructure and in properties which are related to the oxygen content, such as critical
49 temperature, lattice parameters.

50 Various sintering parameters are exploited to densify the material, to reach the maximum
51 oxygen content of the (123) orthorhombic phase and to produce various microstructures with
52 specific features. The challenge in synthesizing dense materials is to avoid microcracks due to
53 an inhomogeneous distribution of grain sizes and to keep an adequately interconnected
54
55
56
57
58
59
60

1
2
3 porosity inside the material, which ensures oxygenation into the bulk.

4
5 Four main steps are involved in the growth of the (123) phase:

- 6
7 (i) The first one is the preparation of the starting powders from different materials:
8 oxides, nitrates or carbonates. According to their nature and quality, various kinds of
9 ceramics may be obtained. These initial powders must consist of a high purity single
10 phase to ensure the formation of the single(123) phase as reported in reference [24].
11
12 (ii) The second step, sintering at high temperatures, requires well-defined experimental
13 conditions concerning the heating rate, the annealing time for the grain growth and
14 the oxygen gas flow. These conditions will determine either solid-solid or solid-
15 liquid diffusion reactions.
16
17 (iii) The third step is the cooling stage from high temperature, which is performed either
18 with a low cooling rate or by quenching under oxygen gas flow, depending on the
19 nature of the study. Slow cooling stabilizes the structure and morphology of the (123)
20 phase. Quenching is the only way of preserving metastable high temperature phases.
21
22 (iv) The fourth step is the oxygenation of YBCO : it is performed by annealing between
23 753K and 823K under oxygen gas flow. This step, and particularly the choice of the
24 annealing time at this temperature, will determine the superconducting properties.
25
26
27
28
29
30
31

32 As these parameters act simultaneously, all these steps are critical and have to be controlled,
33 because they strongly influence the physical properties, microstructure and chemical
34 composition of the synthesized ceramics.
35
36

37 Various types of sintering were investigated for the synthesis of bulk ceramics. Among them
38 we find classical sintering [25], [17], hot-press sintering [26], [27], [18], [19], and melt-
39 textured sintering [28], [29], [30], [31]. For classical sintering, powders are pressed into
40 pellets at room temperature under uniaxial or isostatic pressure, and then sintered. In hot-press
41 sintering, an isostatic pressure from 5 Kbars to 40Kbars [18] is maintained during sintering.
42 In the melt process, pellet sintering is performed with a thermal gradient applied to the
43 substrate [30], [32], under a magnetic field [31] or using flux growth from a seed [33], [34].
44 Thermodynamic equilibrium and out-of-equilibrium states vary from one type of sintering to
45 the other one and can also vary inside a given ceramic from one point to another . Considering
46 all the types of sintering which have been investigated, it appears that hot-press processing
47 and the melt-textured process are the best means to increase J_c . The former implies solid-
48 solid and the latter solid-liquid diffusion.
49
50
51
52
53
54
55
56
57
58
59
60

5. Grain boundaries from solid-solid diffusion

5.1. Influence of processing on grain boundary microstructure and properties

Studies by Ayache et al [25, 35] have reported the influence of sintering conditions on microstructure and physical properties. They described the effects of the high temperature annealing stages, of the oxygenation step, and those of either a new annealing using classical sintering, or of hot-press sintering under various conditions. Initially, two samples were hot-pressed and sintered at 1199K during respectively 13h (sample A₀) and 96h (sample B₀). Next, they were submitted to an oxygenation step at 753K (respectively for 24h and 72h). Several effects of the high temperature stage were observed: increase of the density from 88% to 92%, of the grain size from 3 μ m to 5 μ m, of the critical temperature T_c from 43K to 63K, of J_c by a factor of 3 from 130 to 393 A/cm², and a decrease of the width Δ T_c from 16K to 12K. A second sintering (samples A₁ and B₁) favoured the increase of T_c and a decrease of Δ T_c, improves the magnetic property of the grains, i.e. the shielding efficiency was much better in the second sample inside the grain, although J_c became smaller. It was also shown, from a grain boundary study of YBCO sintered under quasi-isostatic pressure, that a small change in the oxygenation temperature during the final step produces a drastic change in the microstructure (density, grain size, oxygen content from O₇ to O₆) of different types of GB's (clean versus damaged GB) and in the superconducting properties.

5.2. Influence of microstructure on transport properties

The superconducting transition can be observed by plotting the resistance as a function of temperature. The transition profile can be separated in two regimes [36], [37], [38]. The first one, called the main transition regime, corresponds to the drop of the resistance in the grains. It depends mainly on the chemical composition and on the oxygen stoichiometry of these grains. The second one, lying immediately below the main one and covering the range down to zero resistance, is the tail regime. Transport in this regime is controlled by the grain boundaries (weak-links) and corresponds to the temperature range where the Josephson coupling energy of the weak-links is insufficient to overcome the thermal energy. This regime becomes broader with the presence of defects in the grain boundaries (intergranular phases, misorientations, GB oxygen deficiency, or GB cationic deficiency). Figure 8 shows the experimental R(T) measurements obtained from sintered samples A₀, A₁, B₀ and B₁. The results show clearly an increase in the transition width as T_c decreases, revealing a low oxygen content and a low homogeneity in the ceramic, and also the presence of secondary phases at grain boundaries. The curves also indicate that an additional sintering of sample A₀ and B₀ improves the transition. The semi-conducting behaviour of sample A₀ has disappeared

1
2
3 in sample A₁ which still exhibits a wide ΔT_c and a tail region. In sample B₁, the oxygen
4 content is optimum, but the tail effect has increased compared to sample B₀.

5
6 Such an additional annealing increases the oxygen content and improves the quality of the
7 weak-links, as shown by TEM analysis of sample A₁ (figure 9) . This figure shows a grain
8 surrounded by four other grains and particularly by different clean GB's (fig. 9a) with various
9 misorientation angles : a small angle GB (4°) characterized by (001) planes in the two grains
10 (fig. 9b), a clean triple junction showing twinning inside the grains (fig. 9c) and a faceted
11 HAGB exhibiting (001) planes in one grain (fig. 9d).

12
13 GB TEM analysis of sample B₀ indicates the presence of second phases like BaO (and/or
14 CuO) in HAGB (fig. 10). The presence of a second phase is often an indication of a local
15 liquid state in the ceramic [35] . Figure 10a shows the HAGB change from a symmetric
16 faceted GB (fig. 10b) to an asymmetric GB (fig. 10c) in the vicinity of an intergranular defect
17 (fig. 10a). Such a GB has a special orientation close to the coincident site lattice (CSL) $\Sigma 13$
18 GB and contains (001) CuO₂ superconducting planes which are favourable in terms of
19 current. Even with a high angle misorientation of 67°- 69°, the GB could act as a Josephson
20 junction weak-link. As this GB contains a second phase, it is not superconducting.

21
22 For sample B₁, R(T) has been seriously improved in the first part of its profile (fig. 8), but the
23 second part of this curve, corresponding to the tail regime where the transport is controlled by
24 grain boundary weak-links, becomes broader due to the presence of intergranular phases and
25 GB oxygen deficiency. TEM analysis of this sample shows strong changes of the
26 morphology, structure and chemistry on different scales. Figure 11 illustrates the resulting
27 grain size gradient observed by polarized optical microscopy, scanning electron microscopy
28 (SEM) and TEM. This ceramic contains elongated crystals 5 μ m to 100 μ m in length. This
29 elongated shape (fig. 11a and fig. 11b), generally found in these ceramics, is due to the fact
30 that the direction of maximum grain growth is parallel to the (ab) planes (anisotropic
31 direction). The presence of cavities or microcracks, whose size ranges between 10 μ m to
32 20 μ m, is due to an inhomogeneous grain size distribution and to grain misorientations. The
33 external part is well oxygenated as can be seen from the splitting of the 110 reflections in the
34 electron diffraction pattern (right part of fig. 11c). The inner part is characterized by a higher
35 density, a lower oxygen content and the absence of splitting of 110 reflections (right part of
36 fig. 11d). The oxygen gradient clearly affects the lattice parameters deduced from the
37 diffraction patterns and also the twinning morphology. In particular, the twins present in the
38 external part (left part of fig. 11c) of the ceramic are fully relaxed and the lattice parameters
39 correspond to an orthorhombic structure with an oxygen content close to O₇. The twins of the
40 inner part are ferroelastic-like (left part of fig. 11d), and are not completely relaxed by the
41
42
43
44
45
46
47
48
49
50
51
52
53
54
55
56
57
58
59
60

1
2
3 phase transformation. The lattice parameters are those of a tetragonal (123) phase with an
4 oxygen content close to $O_{6.5}$. The microstructure of this inner part explains the remaining tail
5 region in the $R(T)$ curve of figure 8.
6
7

8 9 10 **5.3. Magnetic measurements and weak-link behaviour**

11 The use of hysteresis loop measurements under increasing magnetic field (from 0-250 mT to
12 $H_{\text{appl}} > H_{c2}$) was investigated on ceramics by [39] in order to measure the current density. J_c
13 was calculated from Bean's Model [40]. The J_c versus field behaviour was very similar to that
14 described by a simple self-field limitation hypothesis [41]. These authors found a good
15 agreement between J_c values deduced from this model and from transport current
16 measurements. Magnetic hysteresis loops under low magnetic fields at 4.2K are directly
17 correlated to the GB weak-link behaviour. The higher the hysteresis area, the higher is the
18 shielding efficiency of the weak-links [39]. The shielding effect improves after a new
19 annealing revealing a better magnetic behaviour inside the grains. Figure 12 gathers the J_c
20 results calculated from Bean's model for samples A_0 , A_1 , B_0 and B_1
21
22
23
24
25
26
27
28
29

30 **5.4. Critical current density and grain size dependence**

31 Bulk ceramics show a strong dependence of J_c on grain size [25], with an exponential
32 decrease, comparable to that found in J_c curves as a function of misorientation in the case of
33 bulk bicrystals and thin film bicrystals (see paragraph 8). J_c values, calculated from magnetic
34 hysteresis loops measurements, as a function of grain size are related to grain boundary
35 transport in ceramics. The smaller the grain size, the higher is J_c . In figure 12 the results of
36 classical sintering (ceramic C) and hot-press sintering (ceramics A_0 , A_1 , B_0 and B_1) are
37 compared. The highest value of J_c is obtained by classical sintering which gives the lowest
38 porosity (78%), the maximum oxygen content (O_7) and the minimum grain size ($2\mu\text{m}$). The
39 smallest value corresponds to the largest grain size (from 5 to $100\mu\text{m}$) with an
40 inhomogeneous distribution, a high density (96%) and an oxygen gradient between the inner
41 and external parts of the material. Compared to classical sintering, the hot-press process has
42 the advantage of giving the highest density ceramics. The drawback is the limited oxygen
43 diffusion due to higher compacity.
44
45
46
47
48
49
50
51
52
53

54 There is a competition between density, grain size and oxygen content. Oxygen diffusion is
55 favoured by porosities which play a possible role as diffusion paths. High density ceramics
56 will have more difficulty to reach the maximum oxygen content, as compared to low density
57 ceramics which will be fully oxygenated. The presence of a grain size gradient, as observed in
58 sample B_1 , prevents the connection between grains and makes the J_c value decrease strongly
59
60

1
2
3 (figure 12).
4
5
6
7

8 **6. Grain boundaries from solid-liquid diffusion : Melt-textured ceramics**

9
10 Melt-textured processes allow the synthesis of YBCO ceramics with highly improved
11 transport properties in the presence of a large magnetic field, due to aligned microstructures
12 almost free of weak-link grain boundaries [42], [43]. Melt-processing involves the peritectic
13 melting of the YBCO phase well above the peritectic temperature (1288K in air), yielding a
14 solid phase Y_2BaCuO_5 plus a liquid phase (called «m1») having an approximate
15 stoichiometry Y/Ba/Cu : 1/16/27 [44]. On subsequent slow cooling through the peritectic
16 temperature, directional solidification of YBCO occurs. It was demonstrated from TEM
17 chemical analysis of melt-textured samples that the YBCO phase grows directly from an
18 undercooled yttrium-bearing liquid and not from heterogeneous nucleation sites on
19 Y_2BaCuO_5 crystals [45], [46]. The growth rate limiting factor is expected to be yttrium
20 diffusion at the liquid-YBCO interface. The difference between the growth rate parallel to
21 (001) superconducting planes and that along the perpendicular direction c , induces a
22 microstructure characterized by aligned platelets separated by gaps [47]. These growth-
23 induced defects are filled with secondary phases which have solidified from the trapped
24 liquid. The knowledge of the stable and metastable equilibrium phases at high temperatures,
25 especially in the YBCO primary solidification region, has proved essential to determine the
26 effective conditions for both single crystal growth and YBCO peritectic crystallization. Until
27 now, the solid-state equilibrium, the melting temperatures, the extension of the primary
28 crystallization fields of the solid phases and their dependence on oxygen pressure have been
29 extensively studied [48], [49], [50], [51]. A review of the chemical principles of the
30 preparation of metal-oxide superconductors can be found elsewhere [52].
31
32
33
34
35
36
37
38
39
40
41
42
43
44
45
46
47

48 **6.1. Influence of processing on microstructure**

49 The advantage of melt-textured ceramics is the large extent of a single crystallographic
50 domain, comparable in size to a single crystal. Therefore, they can be used for direct
51 measurements of transport properties. Compared to ceramics made by a solid-solid diffusion
52 process, melt-textured ceramics contain far less GB's due to directional melt growth. They
53 look-like quasi «single-crystals» which contain, in addition, residual gaps from the
54 crystallization of the liquid. These gaps appear as lines in optical microscopy images. Their
55 microstructure also contains Y_2BaCuO_5 (211) precipitates resulting from the peritectic
56 transformation.
57
58
59
60

1
2
3 In these materials, J_c is mainly due to the pinning energy of the vortices at the interfaces
4 between precipitates, (211) and (123) phases, and at twin grain boundaries. The striking
5 feature of these melt-textured ceramics is that a single grain can extend over the whole length
6 of the sample, particularly when the melt process is performed under a magnetic field. Such
7 conditions favour the alignment of the superconducting planes parallel to the applied field
8 [31], so that the sample contains only one or two large domains of the order of a few
9 millimeters (10-30mm), separated by low angle GB's. As an example of YBCO melt-grown
10 under magnetic field, figure 13a shows an optical polarized image with two large domains
11 exhibiting a small misorientation of about 10° . TEM images (fig.13b) show that twins
12 crossing the growth defect are either coherent or incoherent. The growth defect corresponding
13 to a gap filled by the liquid during (123) growth, keeps the same orientation in the sample,
14 parallel to the (001) superconducting planes. The (123) phase also keeps the same orientation
15 across the (211) precipitates.

16 Besides, the melt-process is also commonly used [32] on substrates like MgO single crystals
17 or polycrystalline Y_2O_3 , Y_2BaCuO_5 or Al_2O_3 . In these cases, the growth of YBCO gives rise to
18 a higher proportion of grain boundaries compared to the magnetic field process which takes
19 place without any support. Figure 13c shows an optical micrograph of YBCO melt-textured
20 on a Y_2O_3 polycrystalline substrate. In the centre of the image, one can observe four different
21 domains with a large GB misorientation of 67° . Here again the single domain extends over a
22 few millimeters. The TEM image [46] of figure 13d exhibits characteristic clean interfaces
23 between two (211) precipitates and the (123) phase.

24 Twins are the main GB's present in these materials. Figure 14a shows a polarized light
25 micrograph of a melt-textured ceramic grown on a Y_2O_3 substrate, exhibiting white bands as a
26 result of the twinned microstructure. The light lines correspond to (110) and $(\bar{1}10)$ twin
27 domains. The twin width distribution appears non-uniform. In its centre, a long 89° tilt grain
28 boundary corresponds to a HAGB with an angle departing by 1° from 90° because of the two
29 variants of the orthorhombic (123) structure. Figure 14b shows a TEM micrograph of this
30 [001] tilt grain boundary with evidence of faceting of the (100) and (110) planes. Such a GB
31 contains areas with symmetrical 90° tilt GB's and asymmetrical tilt GB's. The symmetrical
32 one is not energetically favoured, which explains oscillations between these two structures.

33 **6.2. Influence of the substrate on microstructure and physical properties**

34 Melt-growth under a magnetic field is directly performed on a (123) bulk ceramic. Applying
35 a magnetic field gives the best results for J_c . In the case of melt-growth, with or without a
36 thermal gradient, the ceramic is lying on a substrate whose reactivity determines the final
37
38
39
40
41
42
43
44
45
46
47
48
49
50
51
52
53
54
55
56
57
58
59
60

1
2
3 superconducting properties. Because melt-growth results from the crystallization of a liquid
4 brought at a high temperature, any interaction of the liquid with the substrate during the
5 formation of the (123) phase can decrease J_c or, in the worst conditions, can destroy the
6 microstructures and properties. Thus, J_c of melt-textured ceramics will be maximum only if
7 no secondary chemical interaction takes place with the substrate. If the chemical composition
8 of the substrate belongs to the phase diagram (Y_2O_3 or Y_2BaCuO_5), there will be no
9 additional phases. In the case of Al_2O_3 or MgO substrates, chemical reactions lead to
10 secondary phases and damaged microstructures. In particular, the use of MgO single crystal
11 leads to the formation of a non-superconducting YBCO carbonate phase which can be found
12 at the (123)-(211) interfaces as was reported by Gotor et al [53]. The carbon contained in
13 MgO substrates diffuses into the liquid and alters the fabrication process. Long time pre-
14 annealing of MgO substrates at high temperatures can cure this effect.

15
16
17 Two YBCO ceramics were synthesized by the melt-growth method. The first one (D), was
18 prepared on a MgO substrate using a thermal gradient for texturing [54]. The second one (E)
19 was grown on a sintered polycrystalline Y_2O_3 substrate which reacts with part of the liquid
20 stemming from the melt. It forms an orientated layer of the Y_2BaCuO_5 (211) phase, which
21 acts as a seed for the growth of (123) [55]. In both cases, after the high temperature cycle, a
22 low temperature sintering was carried out to obtain the superconducting (123) phase with the
23 good oxygen content and J_c was directly measured (see Table 2). Despite the long annealing
24 time used for oxygenation, sample (D) exhibits a low critical temperature and a large
25 transition width. Such a ΔT_c indicates a low oxygen content, so as the presence of oxygen
26 non-stoichiometry and secondary phases. Susceptibility measurements on sample (D) reveal
27 both intragranular and intergranular magnetic behaviours denoting the presence of defects at
28 grain boundaries and/or the formation of secondary phases in the melt-textured ceramic. TEM
29 imaging (fig. 15) displays damaged interfaces between (211) and (123) phases due to carbon
30 impurity diffusion proceeding from the MgO substrate [55]. The magnetic behaviour of
31 sample (E) is the same as that of a superconducting single crystal, in which only the
32 intragranular properties are visible, indicating that (123) GB's and (123)-(211) interfaces are
33 clean as can be seen from figure 13d. The magnetic behaviour indicates a good shielding
34 effect for both samples (D) and (E), although the GB current transport is null in sample (D)
35 and high in sample (E).

6.3. Melt-textured process as a means of studying YBCO grain boundary bicrystals

36
37
38
39
40
41
42
43
44
45
46
47
48
49
50
51
52
53
54
55
56
57
58
59
60
The use of seed melt-processing allows the fabrication of larger samples with domain lengths
as large as 20-50mm. In a TEM study aimed at high magnetic field applications, Zhang [34]

1
2
3 found a twist component which forms the faceted boundary segments, in addition to the
4 well known symmetrical 90° tilt domain boundaries, and to the asymmetrical 90° tilt
5 boundaries. These GB's are expected to improve current transport in these materials.
6
7

8 The melt-textured process has also been applied to the synthesis of GB bicrystals in order to
9 study their properties for specific orientations. Among these studies, Field et al [56] extended
10 their investigations to transport properties and magnetic resistance properties across high-
11 angle bicrystals using melt-textured $\text{YBa}_2\text{Cu}_3\text{O}_{6+x}$. More recently, characterization of natural
12 and artificial low-angle boundaries in YBCO melt-textured samples were investigated by
13 Delamare et al [57]. Results obtained from a study of controlled bicrystal misorientation, by
14 use dual seeding using single crystals of $\text{Nd}_{1+x}\text{Ba}_{2-x}\text{Cu}_3\text{O}_y$. Todt et al [58] have been reported,
15 giving J_c values very comparable to those observed in thin film bicrystals.
16
17
18
19
20
21
22
23
24

25 **7. Grain boundaries in epitaxial thin films**

26 Since the synthesis of $\text{YBa}_2\text{Cu}_3\text{O}_{7-d}$ thin films, there has been a tremendous interest in
27 epitaxial thin films for fundamental studies of the pairing mechanism, using Josephson
28 and tunnelling junctions [7], [59], [60] and for electronic applications. Due to the short
29 coherence length of these materials, high quality tunnel and Josephson junctions require
30 S/N/S or S/I/S interfaces that are very sharp on the atomic scale, and therefore a surface
31 roughness close to the lattice parameters.
32
33
34
35
36
37
38

39 **7.1. Influence of processing on epitaxial growth**

40 Perfect control of the growth is necessary to guarantee a reliable correlation between physical
41 properties and film structure, especially for a contribution to the understanding of the
42 superconducting mechanism. In particular, it is essential to define the optimum conditions for
43 growing a single phase (123) superconducting thin film orientated along a specific direction,
44 without secondary phases and without any oxygen deficiency which would strongly affect the
45 study of its intrinsic properties. YBCO film morphology and microstructure are strongly
46 dependent on the sintering process. The optimization of the deposit and the understanding of
47 the dependence of its orientation on temperature, are related to the growth mechanism and to
48 the nature of the substrate [61].
49
50
51
52
53
54
55

56 The most usual growth process for HTSC films is pulsed laser deposition which corresponds
57 to a high energy process favouring out-of-thermodynamic-equilibrium conditions. It is
58 difficult to accurately control the microstructure in such a process. In particular, the formation
59 of high roughness, of out-growths, which are secondary phases produced during the process,
60

1
2
3 are very critical and can change from one film to another. For example, in YBCO
4 heterostructures grown by this process, the layer roughness increases with increasing
5 thickness [62], [63] can reach the value of 5nm deteriorating the local properties.
6
7 Nevertheless, a lot of studies on bicrystal-based Josephson junctions, or on interface
8 Josephson junctions, produced optimized films for the study of electronic properties [64],
9
10 [65], [66], [67] studied in YBCO films the effects of cooling time on the electrical properties
11 of grain boundary Josephson junctions with 24° and 36.8° tilt misorientations. A particular
12 study of the effect of sintering, under various oxygen atmospheres, on the weak-link
13 behaviour of YBCO by [68] demonstrated an improvement of the properties of the junctions.
14
15 In the case of thermal evaporation, a low energy process (in the 10eV range), the growth rate
16 can be very low (10^{-1} - 10^{-2} nm/s) which allows a longer time for surface diffusion. This leads
17 to a growth close to the thermodynamic conditions with no or only very few out-growths, and
18 to a surface roughness as low as 0.3nm for some orientations [69].

19
20 YBCO films grown by reactive co-deposition on SrTiO₃ substrates have been recently used to
21 make *in-situ* planar tunnel junctions Pb/YBCO of high electronic quality and reproducible
22 properties [70]. This process is optimized for a very low deposition rate (0.00625nm/s) on a
23 substrate heated at 1023K. These conditions yield films of high crystalline quality. X-ray
24 diffraction rocking curves on the intense 005 reflection and atomic force microscopy (AFM)
25 measurements detect a low mosaicity of the film with FWHM $\approx 0.26^\circ$ and a surface roughness
26 as low as 3.5nm on a $1\mu\text{m}^2$ scale. The junctions grown in these conditions exhibit good
27 conduction properties ($T_c=89\text{K}$, $\Delta T_c=1\text{K}$ for 50nm thickness) [71]. Using the same process,
28 the best conditions to grow YBCO on a MgO substrate are different due to 3D island growth,
29 whereas on a SrTiO₃ substrate 2D growth takes place. The optimum temperature on MgO is
30 1003K. Far from the optimum conditions, the roughness of the film increases drastically
31 within a 10K range and out-growths form on both SrTiO₃ and MgO substrates [69]. It is
32 important to point out the difficulty of preparing a pure [001] thin film without forming also
33 another orientation, because of the closeness of the interfacial energies. In particular, [100]
34 precipitates are often present in [001] YBCO thin films. They introduce 90° planar and
35 vertical GB's which behave as weak-link GB's and decrease J_c .

36
37 The anisotropy of the coherence length makes it difficult to obtain high quality interface
38 junctions with specific orientations such as [100] and [110]. As an example, the growth of a
39 film with a single [110] orientation is extremely difficult to achieve without forming also the
40 [103] orientation. Only the use of special X-ray experiments for controlling the different steps
41 in the formation of (123), makes it possible to obtain a single orientation [100] or [110] [69].
42
43
44
45
46
47
48
49
50
51
52
53
54
55
56
57
58
59
60

7.2. Influence of YBCO growth on film microstructure

A SrTiO₃ single crystal (cubic structure, $a=0.3905\text{nm}$) is the usual substrate for obtaining HTSC films and devices because of its dielectric constant and good matching with YBCO. When YBCO is grown on STO, [001] and [100] zone axes can be formed, depending on thermal conditions. YBCO growth on MgO leads to the formation of misorientations in the films due to 3D island growth and also due to the fact that commercial MgO is not a true single crystal as it contains numerous sub-grain boundaries. Consequently, YBCO epitaxial growth leads to strong planar misorientations around the [001] axis. Those observed from various studies are: 35°, 30.6° and 62.7° [71], [72], [73], [74]. These particular values correspond in fact to coincidence site lattices (CSL) at YBCO GB's. Marshall and Ramesh [75] studied the effect of synthesis conditions on film orientation for different substrates like STO, LaAlO₃, MgO and Y-ZrO₂ (YSZ). They found that STO was the best concerning lattice mismatch, orientation and T_c. MgO and YSZ were the poorest substrates. On MgO they observed 8°, 18°, 26° and 45° misorientations. Other studies of YBCO grown on a YSZ single crystal substrate showed also various misorientated grain boundaries in the thin film [77]. These authors found misorientations of small angle (6.5°), high angle (29°, 45°) and also 90° GB's which correspond to the (ab) plane twinning.

The morphology of YBCO thin films consists of growth islands with terraces of either spherical or square shape, faceted or not, depending on growth conditions. The resulting surface may be either flat (2D growth) or rough (3D growth). Figure 16 shows YBCO thin films grown by a co-evaporation process respectively on STO (a, b, and c) and on MgO substrates (d, e and f). Figures 16a and figure 16d show AFM images of growth islands. Figures 16b and Figure 16e show TEM planar view images of a large area with a single [001] orientation on a STO substrate, and various GB misorientations around the [001] direction on a MgO substrate. The GB rotation angles of 35°, 30.6° and 62.7° about the [001] direction are visible by the rotation angles between the twins of the two grains. Both films exhibit 90° grain boundaries corresponding to (001) plane twinning. The Moires of figures 16c and 16f correspond to the superposition of YBCO 100 and 010 reflections of the (123) phase with those of the substrates. For a MgO substrate there is only one kind of Moire, whereas for STO there are chevron-like Moire structures exhibiting various d-spacings. Those formed on MgO have a constant value, indicating full relaxation in the film. The morphology of YBCO films on STO reveals a residual strain in the vicinity of the substrate.

All YBCO thin films contain growth defects induced by the epitaxial growth, and others resulting from the YBCO structure itself. Stacking faults due to the local chemistry (double

CuO planes are often formed), antiphase grain boundaries created by the presence of steps located either near the surface of the substrate or along the island terraces, are observed. An other type of defect, always observed in c -axis films, is the formation of local a -axis nuclei or grains formed mainly at the interface with the out-growths [71]. Their growth always competes with that along the c -axis as described by Granozio et al [77]. It depends mainly on deposition temperature and rate.

The critical thickness of YBCO on STO ranges between 15 and 30nm, which corresponds to the limit of elastic deformation in a YBCO film. In this range, growth takes place by a 2D to 2D-3D growth mechanism. Above this range, the growth is 3D and the film is relaxed. Its parameters tend towards those of the bulk. 50nm thick films grown on STO are still partially relaxed, while those on MgO are completely relaxed. In the case of MgO, growth takes place by a straightforward 3D mechanism. This difference comes from the large mismatch between YBCO and MgO ($\delta a_f/a_s = 9.26\%$ and $\delta a_f/a_s = 7.84\%$), as opposed to the small mismatch for STO ($\delta a_f/a_s = 2.17\%$ and $\delta a_f/a_s = 0.64\%$). This explains the formation of a YBCO/STO coherent interface and of a YBCO/MgO semi-coherent interface relaxed by dislocations. Films on MgO present a granular behaviour of the R(T) curve [70] with a tail regime due to growth island GB's.

7.3. Influence of the YBCO growth process on grain boundary structure : thin film bicrystals

There is a feature common to all YBCO thin films epitaxially grown on bicrystal substrates STO, MgO or YSZ: the meandering of the grain boundary. Numerous studies were reported concerning YBCO thin film bicrystals grown on STO bicrystal substrates, with the aim of making bicrystal based Josephson junctions. As YBCO is epitaxially grown on STO, MgO, or YSZ GB bicrystal substrates, knowledge of the bicrystal substrate boundary structure is essential for a perfect control of the process and of the intrinsic characteristics of YBCO junctions.

TEM investigations of YBCO thin films grown on various STO bicrystals with misorientations of 24° , 36° , 53° and 67° were performed by various research teams. [78], [79], [80], [81], [82], [83] From these studies, it follows that the meandering behaviour observed does not depend on the misorientation of the bicrystal, but on the growth of the thin film. Even for small misorientations, thin film samples show GB meandering.

Investigations of GB meandering in YBCO bicrystal thin films grown on MgO and YSZ bicrystal substrates were reported by Miller et al [79] for various misorientations (10° , 24° ,

1
2
3 36.8°, 45°, 53.2° and 67°) as a function of the growth process. These experiments point out
4 the strong dependence of the meandering width upon the growth process. In a more detailed
5 study [84] compared, for a 36.8° GB, the magnitude and wavelength of the meander in off-
6 axis magnetron sputtered thin films grown respectively at a high rate of 0.4nm/mn and at a
7 low rate of 0.16 nm/min. They found that the meandering width decreases as the growth rate
8 decreases. In another study of the influence of low energy (co-evaporation) versus high energy
9 processing (laser ablation) [85], [86], showed, in a near $\Sigma 13$ GB, that meandering decreases
10 strongly for lower growth rates. They also observed an increased faceting of the growth
11 islands and consequently of the meandering. Alarco et al [81] studied microstructures and
12 properties of artificial grain boundaries in epitaxial YBCO thin films grown on [001] tilt YSZ
13 bicrystals. They observed by TEM that a 45° [001] tilt GB also presents some wavyness.
14 They also detected the presence of [100] and [110] orientations in their film. Microstructure
15 and Josephson phenomenology of 45° tilt and twist YBCO artificial GB's were investigated
16 by Tafuri et al [83] who also detected GB meandering.

17
18
19
20
21
22
23
24
25
26
27
28 A detailed study of a 24° misorientated [001] tilt GB grown on a STO bicrystal by laser
29 ablation, combining TEM, high resolution electron imaging (HREM), AFM, low voltage
30 SEM and energy dispersive X-ray spectroscopy (EDS) observations was done by Ayache et al
31 [82]. They determined the 3D grain boundary topography from quantitative analysis of
32 HREM Moire images of the overlapping zones, and deduced a GB growth model. In this
33 study they characterized, on different scales, firstly the orientation of the bicrystal substrate
34 and the surface morphology before deposition, and then the YBCO GB's after growth. Moire
35 analysis determined, from the change in lattice parameters, a variation in the oxygen content
36 along the grain boundary, as well as a variation by 4° of the angle of the GB misorientation.
37 Figure 17a shows a TEM image of a YBCO 24° $\Sigma 13$ [001] tilt GB grown on a STO substrate,
38 exhibiting meandering of the GB plane. The electron diffraction pattern is visible in the insert.
39 Figure 17b shows a HREM image of a portion of the overlapping zones corresponding to the
40 superimposition of grain 1 on top of grain 2 (or vice versa) along the GB, on either side of
41 the GB plane. One can notice the oscillation and faceting of the GB plane.

42
43
44
45
46
47
48
49
50
51
52 The way the GB plane oscillates on either side of the GB line is determined by the underlying
53 substrate. It also meanders all along the GB, changing from a symmetrical to an asymmetrical
54 character, depending on its location along the GB and also on the film thickness. Such a GB
55 oscillation induces strong local changes of the current from one place to another.

56
57
58
59
60
From the strikingly converging results obtained by investigating YBCO growth on top of a
bicrystal, it has become clear that, during film growth, the YBCO grain boundary deviates

1
2
3 from the path defined by the boundary of the underlying substrate. YBCO GB meandering
4 behaviour is related to the nucleation and growth mechanisms of the film. All studies indicate
5 that the extent of the meandering may reach 500nm. These appear as general features which
6 confirm the correlation between island-like growth of the film and magnitude of the GB
7 deviation, as well as the relation between shape and GB faceting. As an example, figure 18
8 shows AFM images of YBCO thin film GB's grown on a $24^\circ \Sigma 13$ [001] tilt GB. Figure 18a
9 corresponds to the AFM image of a thin film made by laser ablation and figure 18b to the
10 AFM image of a film made by co-evaporation using a low deposition rate. They differ by the
11 morphology of the growth-islands which present either square-shaped terraces or blurred
12 faceting. The lower the rate, the larger are the faceted islands. Such island shapes are in
13 accordance with what is expected from the thermodynamic conditions of the deposition.
14 Those presenting a clear faceting correspond to the lower deposition rate, i.e. the one
15 allowing the maximum time for atomic diffusion. The results given in the literature confirm
16 that it is the kinetic factor which governs the growth, and not the epitaxial growth nor GB
17 interfacial energies. At the beginning, the epitaxial growth determines the orientation. As
18 growth proceeds, the driving force for the YBCO grain boundary structure becomes the
19 growth mechanism. Figure 19a schematizes the shape of terraces with the holes formed via
20 island coalescence, and figure 19b shows the model derived from a quantitative analysis of
21 the grain boundary which exhibits clearly an oscillation of the GB plane in the thickness of
22 the film. The extent of the meandering on either side of the GB can vary from 10nm to 500nm
23 depending on the growth conditions. As a result, the growth mechanism alters the epitaxial
24 relationships between the YBCO film bicrystal and STO or MgO bicrystals at the GB plane,
25 where the growth terraces come into contact. This situation becomes conflictual and the
26 growth fronts interpenetrate, leading to alternating domains of overlap. These results could
27 well affect the interpretation of the experiments which have been recently carried out to test
28 the symmetry of the superconducting order parameter, through Josephson coupling
29 measurements on grain boundaries with special orientations [87], [88].

30
31
32
33
34
35
36
37
38
39
40
41
42
43
44
45
46
47
48
49
50 An interesting microstructural study on YBCO bicrystal films grown on MgO substrates by
51 liquid phase epitaxy [89], concerned large single faceted GB's. Various misoriented 4° , 8° ,
52 12° , 16° , 24° , 36° and 45° [001] tilt GB's were analyzed on different scales. TEM
53 observations showed single straight faceting over a length of 10-30 μ m. HREM studies
54 showed that all GB's were faceted on the atomic scale, except the 24° and 36° ones, on the
55 scale of a few nanometers. The experimental $J_c(\Theta)$ curve overlaps that observed in classical
56 thin films (see Figure 28) [90].
57
58
59
60

8. Grain boundary structure and properties

8.1. Grain boundary structure and misorientation

A study of small angle [001] tilt GB's by Tsu et al [91] showed faceting, dislocation structures and heterogeneity on various scales. More recently, TEM-EELS studies of hole concentrations near strongly and weakly coupled GB's associated with YBCO flux-grown bicrystals [33], [92] were performed on small and large angle (001) tilt pre-oriented GB's with misorientations of 7°, 12°, 28° and 31°. The key aspect in this work is that the electromagnetic properties and the coupling character of each of the bicrystals were explicitly determined. It was shown that small angle GB's are strongly coupled and that their structures consist in primary GB dislocations. A slight hole depletion was noted near the GB's. In addition, some high angle, mainly [001] tilt GB's are weakly coupled and some are resistive at $T > 4.2\text{K}$. In the former case, the cation structural width is apparently narrow, although GB's can be broad, exhibiting severely depleted zones. The resistive GB's contain a thin coating layer of a second phase: Cu_2O . The chemical composition at small and high angles shows a slight Cu enrichment at the GB's, in good agreement with the characteristic copper non-stoichiometry found in flux-grown YBCO ceramics [54]. GB enrichment in Cu comes from the flux-growth process. The oxygen hole deficiency zone extends over 20 to 40 nm into each crystal.

A systematic study [93] of the structure of symmetric and asymmetric tilt GB's was carried out using geometrical modelling and particularly the coincidence site lattice (CSL) configuration of the (a-b) and (a-c) types. The first one corresponds to atomic planes containing either a,b lattice parameters, or b,c lattice parameters adjoining the boundary. The YBCO layered structure allows four different types of atomic planes to meet at the interface both for a-b and a-c type boundaries. These are Cu-vacancy-Cu, Ba-O-Ba, Cu-O-Cu and Y-Y atomic planes. In this modelling, the fraction of the continuous superconducting planes and the charge associated with the boundary void configurations were determined as a function of the misorientation angle of the a-b boundaries. The geometrical modelling was extended to describe the distortions, the unbalanced charge and the continuity of the Cu-O planes in the asymmetric GB's, and disclinations as well. The critical current density obtained in terms of the depression of the order parameter, the width, and the coalesced region of the boundary were found to agree with experimental observations. Figure 20 shows the resulting models obtained for $\Sigma 37$, $\Sigma 13$, $\Sigma 5$ large angle grain boundaries (20a, 20b and 20c) with their coalesced configuration. One can point out the distortion of the lattice superconducting a-b planes and the voids at the grain boundary. Another example (Fig 20d) corresponds to the (a-c) type GB, showing continuity of the lattice planes a and c, with a mixture of two types of

1
2
3 structural units at the GB. The continuity of the Cu-O planes responsible for the
4 superconducting current is found to depend on the atomic species occupying the common
5 lattice positions of the two adjoining grains. It also determines the critical current density of
6 the GB's. The distribution of the excess charge at the grain boundary is shown to be important
7 in scattering the superconducting pairs. The necessity of neutrality also leads to cation and
8 anion vacancies at the boundary, in turn leading to non-stoichiometry.

9
10 A HREM study of current HAGB's like $\Sigma 1$ 90° grain boundaries by Jia and Urban [94]
11 showed different types of atomic planes at the interface. Three models have been deduced for
12 thin film (100)/(001) interfaces projected along the [010] direction. These models are shown
13 in figure 21 where figure 21a is the HREM image and figure 21b shows the three models of
14 the grain boundary. In model a, grain 1 shows a (001) CuO_2 plane at the upper grain face, and
15 grain 2 a (100) Y-Ba-O plane at the lower face. In model b, grain 1 shows a (001) Ba-O plane
16 and grain 2 a (100) Cu-O plane; in model c, grain 1 shows a (001) CuO plane and grain 2 a
17 (100) Ba-O-Y-O-Ba plane.

28 29 **8.2. Grain boundary misorientation and oxygen content**

30
31 TEM-EELS (electron energy loss spectroscopy) studies by Zhu et al [95, 96] on YBCO bulk
32 ceramics prepared via solid-solid diffusion allowed the analysis of low and high angle GB's
33 and the measurement of the oxygen stoichiometry of GB's using the oxygen K edge pre-peak.
34 It was found that small angle ($\theta < 10^\circ$) and high angle GB's ($\theta > 10^\circ$) can be either fully
35 oxygenated or oxygen deficient. These results, obtained from 20 GB characterizations and
36 exploited using the coincident site lattice (CSL) model, show that all high angle Σ GB's
37 (from $\Sigma 3$ to $\Sigma 20$) present a departure from perfect orientation varying between 3.24° and
38 10.90° . All high angle $\Sigma 3$, $\Sigma 9$, $\Sigma 10$, $\Sigma 13$ and $\Sigma 26$ boundaries studied by Zhu [97] present an
39 oxygen deficiency near the GB's over a width of about 80 nm on either side of each crystal.
40 Figure 22 shows the variation of oxygen content for high angle grain boundaries close to $\Sigma 10$,
41 $\Sigma 13$ and $\Sigma 26$.

42
43 Studies of [001] tilt GB's in YBCO thin films by HREM, Z-contrast and STEM-EELS [98],
44 [99] showed the important role of symmetry in YBCO high angle CSL $\Sigma 5$ and $\Sigma 17$ GB's.
45 The oxygen content does not change in symmetrical GB's, as shown by the presence of the
46 oxygen K pre-edge peak, which is absent in asymmetrical GB's. Figure 23 reproduces the
47 profiles of the oxygen K pre-edge peak used to quantify the oxygen content in GB's. Figure
48 23a shows the pre-edge peak corresponding to the superconducting O_7 phase and figure 21b
49 shows the oxygen deficiency peak corresponding to the O_6 non-superconducting phase.
50
51
52
53
54
55
56
57
58
59
60

1
2
3 Oxygen deficiency in asymmetrical GB's appears clearly in the spatial profile of the
4 normalized oxygen pre-edge peak [99].
5
6
7

8.3. Grain boundaries in bulk and transport properties

8
9
10 It is well known that the limiting factor for current transport is linked to intergranular GB's
11 which are weakly superconducting areas. In granular superconductors, the current flows
12 through complex paths formed by a junction network connecting the grains. Earlier reviews
13 suggested that the limitation of J_c in YBCO materials had to do with both the lack of effective
14 pinning of magnetic flux lines and with the presence of weak-link boundaries across which
15 the supercurrent is limited. Later, based on studies of thin film GB's exhibiting a dependence
16 of J_c upon misorientation, various authors claimed that not all GB's were suitable for high J_c
17 transport. Even later, some high angle boundaries were found to have a noticeable J_c transport
18 capability [100], [101], [102].
19

20
21 It is difficult to obtain high J_c values with classical ceramics, because of the presence of GB's
22 with random orientations. A large number of GB orientations are present in a classical
23 ceramic from small (4°) to large angles (90°), as well as special coincident site lattice Σ
24 HAGB's. In grain-boundary studies on bulk ceramics [95], found that the coincident-site
25 lattice model allows the characterization of a number of grain boundaries present in YBCO as
26 near CSL sigmas : $\Sigma 13$ (22.6°), $\Sigma 17$ (28.7°), $\Sigma 5$ (36.8°), $\Sigma 29$ (45°) and: $\Sigma 1$ (90°), as [001]
27 tilt grain boundaries. A study of GB geometry and energy, in relation with critical currents in
28 YBCO, analyzed numerous data from the literature and showed that random GB's are not
29 clean and cannot transport the supercurrent, while small angle and some high coincidence
30 GB's are clean and can transport the current [103].
31

32
33 A study combining TEM analysis, electrical and magnetic measurements [25] quantified the
34 influence of sintering conditions on current density. Firstly, the variation of the current
35 density in bulk ceramics shows a strong dependence on grain size. The smaller the grain size
36 is, the higher is J_c . A decrease in grain size leads to an increase in the number of junctions,
37 thus making more percolative paths available for current flow [104]. Secondly, due to the
38 Josephson penetration depth of the current in the junction, the effective surface for current
39 transport is weaker for large junctions than for small ones [105]. Thirdly, microcracks can be
40 formed due to the anisotropy of YBCO grain growth. Microstructural studies displayed
41 microcracks in grains larger than $10\mu\text{m}$ [106], [20]. The effect of microcracks is to break
42 possible pathways for the current, thus leading to a decay of J_c . The observed drop of J_c as
43 the grain size increases (Figure 12) is a combination of the these three phenomena.
44
45
46
47
48
49
50
51
52
53
54
55
56
57
58
59
60

In-situ TEM electrical experiments were carried out for various ceramics [107]. These authors

1
2
3 detected, on large angle near Σ GB's, previously characterized by $I(V)$ measurements, a low
4 attenuation of the supercurrent for HAGB's $\Sigma 29$ and $\Sigma 7$. In particular, they measured across a
5 single GB like $\Sigma 7$ a drop of the grain current $I(V)$ by a factor of 3. As shown by HREM,
6 boundaries which do not contain (ab) planes display a small atomic disorder. These
7 experiments are interesting, but cannot be extended to predict a current in the bulk, due to
8 connections with adjacent GB's. Reliable electrical measurements on a single GB are only
9 possible on perfectly pre-oriented GB's.

10
11
12 On bulk GB bicrystals obtained via a melt-process, several workers [56], [57], [58] managed
13 to produce a large range of misorientations from 1° to 45° , controlling the growth using a
14 thermal gradient and controlling the planarity of the grain boundary bicrystal plane. In a series
15 of [100] tilt grain boundaries, they found a difference in critical current density of nearly two
16 orders of magnitude between small ($\theta < 10^\circ$) and high ($\theta > 20^\circ$) misorientation angles. Figure
17 24 shows the variation of the GB current density with its two regimes [58]. This $J_{c\text{ GB}}$ curve
18 shows a decrease of $J_{c\text{ GB}}$ as a function of the misorientation angle, similar to that seen in
19 figure 12 as a function of grain size. The difference lies in the order of magnitude of J_c : it is
20 10^2 times higher in thin film bicrystals than in bulk ceramics. This is in agreement with the
21 larger number of grain boundaries in ceramics. Compared to thin film bicrystal GB's,
22 displaying various misorientations of the grain boundary plane (as described below), bulk
23 bicrystal GB's have a linear and planar GB plane with a single orientation. Such a bulk GB
24 allows a less ambiguous interpretation of the relationship between microtexture and transport
25 properties.

26 27 28 **8.4. Grain boundary structure and current transport modelling**

29
30
31 The limiting factor for transport properties in GBs is the intergranular critical current density.
32 In many materials J_c is suppressed at grain boundaries by phenomena such as interface
33 charging and electronic band structure bending. Current transport mechanisms through low-
34 angle grain boundaries were investigated [108] by calculation of the solutions of the
35 Ginzburg-Landau equation, which account for the observed rapid decrease of the critical
36 current J_c as a function of the misorientation angle. They proposed a mechanism of
37 progressive superconductivity suppression in GB's as a function of θ , due to an excess ion
38 charge on the GB's which shifts the chemical potential in a layer of the order of the screening
39 length in the vicinity of the GB's. They showed that the $J_c(\theta)$ dependence is mostly
40 determined by the decrease of the current-carrying cross section by insulating dislocation
41 cores and by the progressive local suppression of the superconducting order parameter near
42
43
44
45
46
47
48
49
50
51
52
53
54
55
56
57
58
59
60

1
2
3 the GB's as θ increases. The insulating region near the dislocation cores results from a local
4 strain-induced transition to the insulating antiferromagnetic phase.
5

6
7 When the misorientation increases, the separation of the dislocation cores decreases. At the
8 point where the strain fields around dislocation cores begin to overlap, i.e. at the end of the
9 low angle regime (for large HAGB's), models based on linear elasticity become inapplicable.
10 At this stage, the alternative methodology to describe the grain boundary structure is by
11 structural units as shown by Browning et al [99]. The advantage of such a model is that, once
12 the structural unit has been determined, it is possible to predict the structure of the GB for any
13 orientation. But such a deduction in perovskite oxide GB's is very difficult due to the
14 inhomogeneity along the atomic GB's structure. As an example, Ayache et al [109] found
15 new atomic structural units of a symmetric [001] 67.4° near- $\Sigma 13$ tilt grain boundary in SrTiO_3
16 identified by a quantitative analysis of lattice images, reconstructed electron exit waves, and
17 Z-contrast images. They found evidence for the formation of three new structural units
18 centered either on Sr columns or on TiO columns. This GB presents a multiplicity of
19 structural units (i.e. various stoichiometries along the GB) which contain 4 and 5 columns in
20 coincidence, and the same number of doublets of columns of the same nature in close
21 proximity. These results highlight new interpretations of the formation of grain boundary
22 structural units in perovskite oxide system.
23
24
25
26
27
28
29
30
31
32
33

34
35 Atomic scale modelling of the GB potential in cubic perovskite oxides was developed by
36 Klie et al [110], based on a combination of experiments on 8° and 58° [001] tilt SrTiO_3 GB's
37 and on theoretical calculations. Distance–valence least square analysis and multiple scattering
38 calculations were used to determine the density of the GB states. They showed, for both high
39 and low angle tilt GB's, the validity of the Thomas-Fermi approach of screened charges
40 associated to the classical Schottky model. Figure 25 (a and b) shows the density of states for
41 two SrTiO_3 GB's (pristine). One can see clearly the charge distribution in the dislocation
42 cores for low (a) and high (b) angle GB's. The smallest misorientation corresponds to the
43 largest distance between the dislocations cores avoiding the overlap of the strain field [110].
44 In comparison, figure 25c shows the charge distribution in a 4° [100] tilt boundary in Ca-
45 doped (left) and undoped (right) YBCO [111]. The core centre corresponds to a negative
46 charge.
47
48
49
50
51
52
53
54
55

56 A numerical simulation study of the influence of temperature and interface space charge on
57 the GB conductivity in Ni acceptor-doped SrTiO_3 ceramics [112] showed that the electrical
58 characteristics of these GB's could be deliberately modified by decorating the GB's with
59 suitable dopants (Ni, Ag, Ca).
60

8.5. Grain boundaries in thin films and transport properties

The first studies of transport properties in thin film bicrystals were performed on samples prepared by laser ablation [113]. Various STO bicrystals with misorientation angles ranging from 0° to 35° were produced by melt-processing and used as substrates for growing YBCO bicrystals films in order to study the orientation dependence of the GB critical current. The critical current density across GB's on the (ab) basal plane of YBCO bicrystals was measured at 4.2K as a function of misorientation. The ratio of grain boundary critical current density (J_{cGB}) to average value of the critical current density in the two grains (J_{cG}) was plotted as a function of misorientation (Fig.26). The J_{cGB}/J_{cG} ratio decreases exponentially with increasing GB misorientation.

This curve shows that, even for 0° GB misorientation, J_{cGB}/J_{cG} decreases by a factor of two. This means that, even for a junction free from any misorientation, coupling between the two grains is decreased. Due to the sensitivity of J_c to crystallographic orientation, the coupling is maximum along the crystallographic axis and decreases with increasing GB misorientation. Such a behaviour cannot be related to classical coupling, but rather to pinning. Results obtained from the study of the residual critical current in HTSC bicrystal GB junctions tend to support such an hypothesis [65]. They showed that the residual current increases as the misorientation decreases. In this kind of systems, the residual critical current is attributed to inhomogeneities inside the barrier. The GB model proposed considers a periodic modulation of the order parameter, associated with a periodic structural change element which is consistent with only some of the properties of GB's junctions [114], and also with the presence of a residual current. Within the framework of such a model, defects such as dislocations depress the GB order parameter. A GB can be described as an array of a large number of parallel Dayem bridges [115] separated by normal areas. Figure 27 shows such a grain boundary model schematically.

Magneto-optical studies of flux penetration and critical current density in [001] tilt YBCO thin film bicrystals were made for small misorientation angles ($5^\circ < \theta < 7^\circ$) by Plyanskii et al [116]. They found a characteristic cusp in the flux distribution, which indicates that the critical current density J_{cGB} across the GB is smaller than the J_{cG} of the grain. They used Bean's model to separate the GB contribution from that of the grains. They found that small angle grain boundaries can provide additional flux pinning. This is plausibly associated with GB dislocations which accommodate the GB misorientation.

Another recent work on grain-boundary dissipation in HTSC's by Gray et al [90] re-examined the explanation of the zero field data obtained for thin films and bulk bicrystals

1
2
3 [001] tilt GB's. Their J_{cGB} values are plotted in Figure 28 as a function of the misorientation
4 angle. Both bulk and thin film bicrystals appear to behave in the same way. This work took
5 advantage of microscopically more perfect bicrystals. The explanation is based on the pinning
6 of Josephson junction vortices by the meandering found in thin film GB's. These authors also
7 point out that there is no evidence that J_{cGB} of GB's does not drop with applied magnetic field
8 as quickly as expected from a simple Josephson junction model. Experiments [116], [65] and
9 modelling [117] show that the pinning of vortices is a key process involved in the
10 superconducting behaviour of GB's, as well as in the dissipation in the bulk. The Gurevich
11 and Cooley mechanism implies that the trapped flux can improve the critical current I_c , if it is
12 not governed only by grain boundaries.
13
14
15
16
17
18
19
20
21

22 **8.6. Critical current density and doping of the grain boundaries**

23 The critical current density J_c of the supercurrent which can pass through polycrystalline
24 materials without destroying superconductivity is remarkably small. There have been various
25 attempts to enhance the transport properties of multicrystalline ceramics and to understand the
26 mechanism leading to a reduction of the critical currents at GB's. Appropriate doping of the
27 grains provides a mean of optimizing the transport properties of GB's in HTSC. This is
28 demonstrated in the exemplary case of GB's in bicrystalline Ca- and Co-doped YBCO films
29 [118]. By Ca doping, the critical current density is strongly increased and the normal state
30 resistivity significantly reduced, as compared to the values obtained for equivalent junctions
31 in undoped films.
32
33

34 Hammerl et al [119], investigating YBCO polycrystals, found that the partial replacement of
35 yttrium by doping $YBa_2Cu_3O_{7-d}$ with calcium increased grain boundary J_c values
36 substantially, but only at temperatures lower than 77K. The resulting doped grain boundary
37 suggests a viable approach for producing cost-effective superconducting power cables
38 operating at liquid nitrogen temperature. Recently, Klie et al [111] reported image simulations
39 and spectroscopy at the atomic scale, that demonstrate that in poly-crystalline YBCO, highly
40 strained grain boundary regions contain excess O vacancies, which reduce the local hole
41 concentration. Calculation of Ca and O vacancy formation energies were performed using
42 density-functional theory in the local density approximation. They deduce for bulk YBCO
43 that Ca impurities indeed substitute for Y, but in GB regions under compression and tension
44 they also replace Ba and Cu, relieving strain and suppressing O-vacancy formation. They also
45 used atomic resolution Z-contrast imaging in the STEM to show the arrangement of the cation
46 columns at the grain boundary, in correlation with EELS to probe the concentration of Ca and
47 the local concentration of holes. As an example, figure 29 shows atomic resolution Z-contrast
48
49
50
51
52
53
54
55
56
57
58
59
60

1
2
3 images of an undoped pristine (SrTiO_3) 4° [001] tilt grain boundary and of a Ca-doped 4°
4 [001] tilt YBCO GB [111]. Figure 29a shows dislocation cores in the typical pentagonal
5 arrangement of the GB structural unit. This latter corresponds to one type of structural units
6 found in SrTiO_3 and described by Duscher et al [120]. Figure 29b shows the Y/Ba column
7 pentagonal arrangement in the Ca-doped GB, which encloses three columns, two on the Cu-O
8 and one on the Y/Ba sublattice. Figures 29c and 29d show the scheme of the core structure
9 where EELS probe analysis was performed. Their profiles through positions 1-5 show a high
10 Ca content and less O-deficiency in the doped dislocation cores.

11
12 Another study on the modification of transport properties in low angle GB's via calcium
13 doping of YBCO textured thin films [121], showed an increase of the critical density
14 [$J_{cGB}(\theta)$] by up to 40% and 100% for respectively the 4° and 8° GB's. Considering the
15 Gurevich and Pashitskii model [108] for current transport at low angles, the improvement can
16 be attributed to a reduction of the strain field and the localized charges, leading to a reduced
17 built-in potential in the dislocation cores.

18
19 For 5° [001] tilt GB's, Ca addition is clearly beneficial, particularly when the sample is
20 oxygen-treated to further overdope the sample after growth, as demonstrated by Daniels et al
21 [122]. They showed that Ca-doping decreases excess GB resistance and diminishes the gap
22 between inter- and intra-grain density over a wide field and temperature range. Another study
23 investigated transport properties on low angle YBCO GB's of undoped and doped thin film
24 bicrystals [123] of 4° , 8° , 12° , 16° misorientation angles. They reported that Ca-doped
25 YBCO bicrystal films, with 10% Ca substitution, showed no significant J_c enhancement at
26 77K in zero field, but a strong decrease of J_c at higher magnetic fields due to a reduced
27 irreversibility field at 77K . Ag-doped YBCO films showed increased critical current densities
28 at higher fields and a slightly shifted transition from strong to weak behaviour with respect to
29 undoped YBCO bicrystal films.

30
31 Recently, direct evidence for negative grain boundary potential in Ca-doped and undoped
32 $\text{YBa}_2\text{Cu}_3\text{O}_{7-d}$ was obtained using electron holography in a transmission electron microscope
33 [124]. They found a reduction of negative charge at grain boundary dislocations in Ca-doped
34 YBCO, as compared to undoped YBCO, and particularly a significant decrease of the size of
35 the perturbed region in the Ca-doped samples (see Figure 25). This appears to be the principal
36 mechanism for the improved interfacial superconductivity.

37
38 Very recently, statistical thermodynamics and kinetics were applied to study the origin and
39 evolution of space charge and band-bending effects at low angle [001] tilt GB's and the
40 effects of Ca doping upon them [125]. Atomistic simulations, using shell models of
41 interatomic forces, were used to calculate the energetics of various relevant point defects.

1
2
3 They found that segregation of calcium is strongly determined by the strain field, and that the
4 nature of the space charge is closely related to the oxygen content. Doping calcium at small
5 angle YBCO tilt GB's leads to an increase of J_c through an increase of the hole content,
6 which enhances negative potential regions due to the segregation of calcium, and helps to
7 passivate disorder at the boundary.
8
9

10 11 12 13 **8.7. Grain boundaries: from the bulk to thin films**

14 Table 3 summarizes the various types of ceramics investigated in the field of YBCO
15 superconducting grain boundaries. It indicates also the GB quality, i.e. either clean or
16 degraded (oxygen deficiency or cationic stoichiometry change) for small and high angle
17 GB's.
18

19 Figure 28 reproduces the results taken from the literature, concerning the variation of J_c as a
20 function of the misorientation angle in YBCO [001] tilt bulk [58], [126] and thin film [127],
21 [128], [129] grain boundary bicrystals. The black symbols correspond to J_{cGB} in thin films
22 and the white ones to bulk bicrystals. Grain boundaries, both in bulk and in thin films, have
23 been improved with high quality materials allowing reliable measurement of the physical
24 properties. Comparison of GB's J_{cGB} in the bulk and in thin films indicates clearly a similar
25 behaviour as a function of misorientation. The J_c values in films are larger by a factor of 10^2
26 than those for a perfectly defined bulk GB's, even though they have, on the atomic scale, a
27 perfect GB plane linearity. The reason for such a behaviour lies in the pinning of the vortices
28 along the GB plane [90]. In thin films, it is the growth island configuration which induces the
29 high current density. This latter has its origin in the high pinning energy due to the film
30 microstructure, i.e. dislocations at the interfaces between growth islands (Figure 17). These
31 defects have a suitable size, of the order of the coherence length, so as a suitable orientation
32 for pinning vortices. Comparing an equal GB misorientation in a bulk bicrystal and in a thin
33 film bicrystal, the additional J_c observed is only due to the film growth. Finally, J_{cGB}
34 determined by the misorientation itself is the same for bulk and thin films. On this basis
35 Mannhart et al [130] devised their experiment for the creation of magnetic flux by single
36 grain boundaries in YBCO.
37
38
39
40
41
42
43
44
45
46
47
48
49
50
51
52

53 In thin films, the critical current path across a grain boundary varies with the local
54 misorientation. It can be represented by a diagram (fig. 30) which shows the combination of
55 symmetrical and asymmetrical faceting on either side of the GB plane. With reference to
56 calculations based on the influence of $d_{x^2-y^2}$ symmetry in device applications of HTSC grain
57 boundary junctions, Mannhart et al [130] modelled the GB current density as a function of the
58
59
60

1
2
3 misorientation, taking into account the GB geometry. In their model the GB plane is vertical,
4 which is unrealistic from the point of view of previously quoted experimental studies. J_c is
5 calculated considering various GB geometries: symmetrical GB, asymmetrical GB, and
6 another model taking into account the OP $d_{x^2-y^2}$ symmetry and the vertical faceting of the GB
7 plane. These GB models are represented in figure 31a and the results of the calculation in
8 Figure 31b, which includes also the experimental data from Dimos et al [113]. None of these
9 calculations reproduces the experimental data in thin films. Based on the knowledge of the
10 GB plane structure, and taking into account the pinning contribution for small angle GB's,
11 new calculations should be done to fit the experimental results obtained on well-defined grain
12 boundaries. An extensive review of the nature of GB's in HTSC's can be found in Babcock
13 and Vargas [131].
14
15
16
17
18
19
20
21
22
23

24 The results of TEM-EELS studies of hole concentrations near strongly and weakly coupled
25 grain boundaries in electromagnetically characterized YBCO bicrystals show that the
26 electronic structure of the boundary region differs from that of the bulk [92]. It is substantially
27 wider than both the YBCO coherence length and the structural and compositional width of the
28 GB, as suggested by HRTEM imaging and cation non-stoichiometry studies. These results
29 also suggest a continuous transition from a strongly to a weakly coupled GB character. The
30 very recent results on the modification of transport properties in low angle GB's via calcium
31 doping [121] show the role of impurities on the electronic structure and particularly the space
32 charge effect. The improvement of J_c can be attributed to a reduction of the strain field and
33 the localized charges at the GBs. Nevertheless, calculation and experiments performed by
34 Klie et al. [111] on Ca doped YBCO demonstrate that ionic radii are more important than
35 their electronic valences for enhancing J_c .
36
37
38
39
40
41
42
43
44
45
46

47 9. Conclusion

48
49 All the data reviewed give evidence that grain boundaries in YBCO materials cannot be
50 understood without having available specific information about their local composition,
51 structure, ionic and electronic state. They confirm that studies of bicrystals are crucial for
52 HTSC development. As a general rule, the observations are consistent with the predominance
53 of current fluxes in the (001) superconducting planes of HTSC materials. Consequently, some
54 high angle GB's can transmit a reasonably high supercurrent, provided they correspond to a
55 coincidence relationship between adjacent crystals and also provided their configuration is
56 compatible with an easy propagation of Cooper pair electrons in the CuO_2 (ab) planes.
57
58
59
60

1
2
3 For small angle GB misorientations ($\theta < 10^\circ$), the pinning contribution has to be taken into
4 account in the models, in addition to the $d_{x^2-y^2}$ symmetry of the order parameter. These
5 implications are contained in the weak-link behaviour for large angle grain boundaries.
6 Experiments and modelling also show that the pinning of vortices is a basic mechanism which
7 governs the superconducting behaviour of GB's, so as the dissipation in the bulk.
8 Accordingly, $J_{c(GB)}$ is determined by the misorientation itself, thus being the same for the bulk
9 and for thin films. The current density difference $(J_{cGB})_{\text{film}} - (J_{cGB})_{\text{bulk}}$ is only due to the
10 growth of the film and to the induced structure of the GB plane.
11
12
13
14
15
16
17

18 Acknowledgements

19 My very special thanks to Mr. Michel Gasgnier for his contribution throughout the time of our
20 collaboration and especially right now for his positive and constructive criticisms while re-
21 reading the manuscript. My thanks go also to Bernard Lang for his kind and efficient help in
22 correcting my English writing.
23
24
25
26
27

28 References

- 29
30 [1]. WU, M. K., ASHBURN, J. R., TORN, C. J., HOR, P. H., MENG, R. L., GAO, L, HUANG, Z. J., WANG. Y.
31 Q and CHU. C. W., 1987, Phys. Rev. Lett., **58**, 908.
32
33 [2]. MAEDA, H., TANAKA, Y., FUKUTOMI, M. and ASANA. T., 1988, Jpn. J. Appl. Phys. Pt. 2, **27**,
34 L209.
35
36 [3]. SHENG, Z. Z and HERMANN. A. M., 1988, Nature (London) **332**, 55.
37
38 [4]. GROSS, R., 1993, In Interfaces in High-Tc superconducting systems, ed. SL. Shinde, DA
39 Rudman, Springer-Verlag, New York., 176.
40
41 [5]. BARONNET, A and PAGANO, S., 1994, J. Supercond. 7, **2**, 375.
42
43 [6]. SPECHT, E. D., SPARKS, C. J. DHERE, A. G., BRYNESTAD, J., CAVIN, O. B., KROEGER, D. M. and
44 OYE, H. A., 1988, Phys. Rev. B**37**, 7426.
45
46 [7]. TSUEI, C.C., KIRTLEY, J.R., CHI, C.C., YU-JAHNES, L.S., GUPTA, A., SHAW, T., SUN. J.Z. and
47 KETCHEN, M.B., 1994, Phys. Rev. Lett., **73**, 593.
48
49 [8]. SIGRIST, M. and RICE, T. M., 1992, J. Phys. Soc. Japan, **61**, 4283.
50
51 [9]. ALARIO-FRANCO, M. A., CAPONI, J. J., CHAILLOUT, C. and CHENEVAS, J., 1987, Mat. Res. Bull.
52 **22**, 1685.
53
54 [10]. ALARIO-FRANCO, M. A., CAPONI, J. J., CHAILLOUT. C., CHENEVAS, J. and MAREZIO, M., 1988,
55 Mater.Res. Soc. Proc. **99**, 41.
56
57 [11]. VAN TENDOLOO, G., ZANDBERGEN, H. W. and AMELINCKX, S., 1987, Solid State Commun, **63**,
58 603.
59
60 [12]. CHAILLOUT, C., ALARIO-FRANCO, M. A., CAPONI, J. J., CHENEVAS, J., HODEAU, J. L. and
MAREZIO, M., 1987, Phys. Rev. B**36**, 7118.

- 1
2
3 [13]. BEYERS, R and SHAW, T. M., 1989, Solid State Physics, Vol **42**, 135.
4 [14]. CEDER, G., 1994, Molecular Simulation, **12**, 141.
5 [15]. MATIC, V.M., MILIC, M. and LAZAROV, N.DJ., 2000, Physica C, 339, 27.
6 [16]. AMBROSCH-DRAXL, C., KORZHAVYI, P. A. and JOHANSSON, B., 2000, Physica C, **341-348**, 1997.
7 [17]. AYACHE, J., GASGNIER, M., BOIRE, P. and WICKER, A., 1991, Journal of the European Ceramic
8 Society, Euro-Ceramics II, vol 3, Eds. G. Ziegler, H. Hausner, Deutsche Kremische
9 Gesellschaft, 2215.
10 [18]. BOIRE, P, AYACHE, J., CHATEAU. C. and LEGER, J.M., 1992, J. Mat. Sci. Eng., **B14**, 169.
11 [19]. AYACHE, J., BOIRE, P., FERT, A.R., BOZEC. X., NAN CHEN and ROUTBORD. J.L., 1992,
12 Supercond. Sci. Technol. **5**, 634.
13 [20]. SABRAS, J., DOLIN, C., AYACHE, J., MONTY, C., MAURY, R and FERT, A.R., 1990, IIB89, J.
14 Phys., Suppl au n°1, **51**, 1035.
15 [21]. ROTHMAN, S.J., ROUTBORT, J.L and BAKER, J.E., 1989, Phys. Rev. **B40**, 8852 .
16 [22]. TU, K. N., YEH, N. C., PARK, S. I. and TSEI, C. C., 1989, Phys. Rev. **B39**, 419.
17 [23]. ROUTBORT, J.L and ROTHMAN, S.J., 1989, DIF 89 Aussois, NATO, ASI France.
18 [24]. LEGROS, C., HAUT, C., PONSONNET-MORA, L. and AYACHE, J., 1999, J. Eur. Ceram. Soc **19** (2)
19 165-173.
20 [25]. AYACHE, J., SABRAS, J., GASGNIER, M., MONTY, C., MAURY. R., BOZEC, X., FERT. A.R,
21 REDOULÈS, J.P., SNOECK, E. and ROUCAU, C., 1990, J. Less .Com. Met., **164 & 165**, 152.
22 [26]. PANDEY, R. K., GILBERT, G.R., KIRK, W. P., KOBIELA, P. S., CLEARFIELD, A. and SQUATTRITO,
23 P. J., 1988, J. Supercond., **1**, 45.
24 [27]. ASLAN, M., JAEGER, H., SCHULZE, K., FRISCH, A. and PETROW, G., 1990, J. Am. Ceram. Soc.
25 **73**, 2, 450.
26 [28]. ALFORD, N. M., BUTTON, T. W., POLLARD, R. J. and MCCARTNEY, D. G., 1989, J. Appl. Phys.,
27 **66**, 5930.
28 [29]. GINN, P., CHEN, W., ZHU. N., LAMAGAN, M. and BALCHANDRIAN, U., 1990, Appl. Phys. Lett.,
29 **57**, 1455.
30 [30]. AYACHE, J., PELLERIN, N. and ODIER, P., 1993, Europ. Cer. Soc, Proceeding 3rd ECR'S Madrid,
31 Vol **2**, 485.
32 [31]. BARBUT, N., AYACHE, J., CHATEIGNIER, D. BOURGAULT, D., TOURNIER, R., GOTOR, F.J., GERMI,
33 P. and PERNET, M., 1994, Physica C, **235-240**, 348.
34 [32]. PELLERIN, N., ODIER. P., SIMON. P. and CHATEIGNIER, D., 1994, Physica C, 222, 133.
35 [33]. BABCOCK, S.E. and LARBALESTIER, D.C., 1994, J. Phys. Chem. Solids, **55**, 1125.
36 [34]. ZHANG, X. F., 1998, Supercond. Sci. Technol. **11**, 1391.
37 [35]. AYACHE, J. and GASGNIER, M. ,1989, Intern. Conf. Supercond "ICMAS 89", Paris, 145.
38 [36]. GOLDSCHMIDT, D., 1989, Phys. Rev. **B39**, 2372.
39 [37]. GOLDSCHMIDT, D., 1989, Phys. Rev. **B39**, 9139.
40 [38]. ROSENBLATT, J., RABOUTOU, A., PEYRAL, P and LEBEAU, C., 1990, Rev. Phys. Appl . **25**, 73.
41
42
43
44
45
46
47
48
49
50
51
52
53
54
55
56
57
58
59
60

- 1
2
3 [39]. MAURY, R., FERT, A. R., REDOULÈS, J. P., AYACHE, J., SABRAS, J. and MONTY, C., 1990, *Physica*
4 *C*, **167**, 591.
5
6 [40]. CHEN, D. X., SANCHEZ, A., NOGUES, J. AND MUOZ, J. S. (1990), *Phys. Rev. B* **41**, 9510.
7
8 [41]. DERSCH, H. and BLATTER, G., 1988, *Phys. Rev. B* **38**, 16, 11391.
9
10 [42]. MURAKAMI, M., 1992, *Supercond. Sci. Technol.* **5**, 185.
11
12 [43]. SALAMA, K. and LEE, D., 1994, *Supercond. Sci. Technol.* **7**, 177.
13
14 [44]. GERVAIS, M., ODIER, P. and COUTURE, J. P., 1991, *Mater. Sci. Eng. B* **8**, 287.
15
16 [45]. AYACHE, J., PELLERIN, N. and ODIER, P., 1994, *Supercond. Sci. Technol.*, **7** 655.
17
18 [46]. AYACHE, J., GOTOR, F.J., PELLERIN, N. and ODIER, P., 1997, *J. Mater. Res.*, Vol **12**, N°2 338.
19
20 [47]. GOYAL, A., ALEXANDER, K. B., KROEGER, D. M., FUNKENBUSH, P. D. and BURN, S. J., 1993,
21 *Physica C* **210**, 197.
22
23 [48]. KIM, J. S. and GASKELL, D. R., 1994, *J. Am. Ceram.* **77**, 753.
24
25 [49]. KRABBES, G., BIEGER, W., WIESNER, U., RITSCHER, M. and TERESINK, T., 1993, *J. Sol. State.*
26 *Chem.* **103**, 420.
27
28 [50]. LEE, B. J. and LEE, D. N., 1991, *J. Am. Ceram.* **74**, 78.
29
30 [51]. WONG-NG, W. and COOK, L. P., 1994, *J. Am. Ceram.* **77**, 1883.
31
32 [52]. TRETAKOV, D., YU, D. and GOODILIN, E. A., 2000, *Russian Chemical Reviews.* **69** (1) 1.
33
34 [53]. GOTOR, F.J., PELLERIN, N., ODIER, P., CAZY, E., BONNET, J.P., FERT, A. and AYACHE, J., 1995,
35 *Physica C* **247** 252.
36
37 [54]. ODIER, P., GOTOR, F.J., PELLERIN, N., LOBBO, R.P.S., DEMBINSKI, K., AYACHE, J. NOEL, H.,
38 *POTEL, M., CHAMINADE, J.P. and COLLIN. G., 1998, Mat. Sci. Eng., B* **52** 117.
39
40 [55]. PELLERIN, N., GOTOR, F.J., ODIER, P., AYACHE, J., FERT, A., CAZY, E. and BONNET, J.P., 1994,
41 *Physica C* **235-240**, 381.
42
43 [56]. FIELD, M.B., CAI, X.Y., BABCOCK, S.E. and LARBALESTIER, D.C., 1993, *IEEE Trans. of Appl.*
44 *Super.*, **3**, 1479.
45
46 [57]. DELAMARE, M.P., WALTER, H., BRINGMANN, B., LEENDERS, A. and FREYHARDT, H.C., 2000,
47 *Physica C*, **329**, 160.
48
49 [58]. TODT, V. R., ZHANG, X. F., MILLER, D. J., ST. LOUIS WEBER, M. and DRAVID, V. P., 1996, *Appl.*
50 *Phys. Lett.*, **69**, 24, 3746.
51
52 [59]. DIMOS, D., CHAUDHARI, P. and MANNHART, J., 1990, *Phys. Rev.*, **B 41**, 4038.
53
54 [60]. CHAUDHARI, P., MANNHART, J., DIMOS, D., TOURI, C.C., CHI, J., OPRYSKO, M.M. and
55 *SCHEUERMANN, M., 1988, Phys. Rev. Lett.* **60**, 1653.
56
57 [61]. MILETTO GRANOZZO, F., SALLUZZO, M. and SCOTTI DI UCCIO, U., 2000, *Phys. Rev. B*, **61**, 756.
58
59 [62]. AYACHE, J., CONTOUR, J.P., DOLIN, C., DROUET, M. and REVELOSONA, D., 1997, *J. Alloys.*
60 *Compounds.*, **251**, 185.
[63]. AYACHE, J., CONTOUR, J.P., CHENU, C., DROUET, M., DURAND, O and MAGIS, M., 1999,
Interface Controlled Materials (M. Rühle and H. Gleiter Editors) **Vol.9**, 249.
[64]. HUANG, Y., MERKEL, K. L., MOECKLY, B. H. and CHAR, K., 1999, *Physica C* **314**, 36.

- 1
2
3 [65]. SARNELLI, E., CHAUDHARI, P. and LACEY, J., 1993, Appl. Phys. Lett., 62, n° 7, 777.
4
5 [66]. OGAWA, T. , 1999, Physica C, **313**, 305.
6
7 [67]. OGAWA, T. 1999, Physica C, **320**, 135.
8
9 [68]. PATHAK, L.C., MISHRA, S.K., DAS, S.K., BHATTACHARYA, D. and CHOPRA, K.L., 2001, Physica
10 C, **351**, 295.
11 [69]. KIM, S.J., GRISON, X., AYACHE, J., LESUEUR, J. and LALU, F. 2003, J. Cryst. Growth. **249**, issues
12 1-2, 186.
13
14 [70]. LESUEUR, J., APRILI M., GRISON, X., KIM, S. J. and AYACHE, J., 1998, proceedings of SPIE
15 Congress, San Diego.
16
17 [71]. KIM, S. J., AYACHE, J., GRISON. X., LESUEUR, J., APRILI, M. and LALU, F., 1998, proceedings of
18 SPIE congress, San Diego.
19
20 [72]. STREIFFER, S.K., LAIRSON, B.M., EOMS, C.B., CLEMENS, B.M., BRAVMAN, J. C. and GEBALLE,
21 T.H., 1991, Phys. Rev., **B43**, 16, 43.
22
23 [73]. RAMESH, R., HWANG, D.M., BARNER, J.B., NAZAR, L., RAVI, T.S., INAM, A., DUTTA, B., WU,
24 X.D. and VANKATESAN, T., 1990, *J. Mat. Res.*, **5**, n° 4, 704.
25
26 [74]. WILLIAMS, E.J. and STOBBS, W.M., 1993, Physica C, **208**, 96.
27
28 [75]. MARSHALL, A. F. AND RAMESH, R., 1994, in Interfaces in High-Tc superconducting systems.
29 Editors. Shindé. S. L. and Rudman. D. A., 71.
30
31 [76]. TIETZ, L.A. and CARTER, C.B., 1991, Physica C, **182**, 241.
32
33 [77]. GRANOZIO, F.M., SALLUZZO, M., SCOTTI DI UCCIO, U., MAGGIO-APRILE, I. and FISCHER, O.,
34 2000, Phys. Rev.B **61**, 1, 756.
35
36 [78]. TRAEHOLT, C., WEN, J.G., ZANDBERGEN, H.W., SHEN, Y. and HILGENKAMP, J.W.M., 1994,
37 Physica C, **230**, 425.
38
39 [79]. MILLER, D.J., ROBERTS, T.A., KANG, J.H., TALVACCHIO, J., BUCHHOZ, D.B. and CHANG, R.P.H.,
40 1995, Appl. Phys. Lett., **66**, 2561.
41
42 [80]. SEO J.W., KABIUS B., DÄHNE U., SCHOLEN A. and URBAN K., 1995, Physica C, **245**, 25.
43
44 [81]. ALARCO, J.A., OLSSON, E., IVANOV, Z.G., WINKLER, D., STEPANTSOV, E.A.; LEBEDEV, O.I.,
45 VASSILIEV, A.L., TZALENCHUK, A.YA. and KISELEV, N.A., 1995, Physica C, **247**, 263.
46
47 [82]. AYACHE, J., THOREL, A., LESUEUR, J. and DAHMEN, U., 1998, J. Appl. Phys., **84**, 9 4921.
48
49 [83]. TAFURI, F., MILETTO GRANOZIO, F., CARILLO, F., DI CHIARA, A., VERBIST, K. and VAN
50 TENDELOO, G., 1999, Phys. Rev. B **59**, n° 17, 11523.
51
52 [84]. ZHANG, X. F., MILLER, D. J. AND TALVACCHIO, J., 1996, J. Mater. Res., vol 11, 1, 2440.
53
54 [85]. PASSERIEUX, G. , 2002, Thesis janvier 2002, Orsay, France.
55
56 [86]. AYACHE, J., PASSERIEUX, G., LESUEUR, J. and LARTIGUE. KORINEK, S., 2005, Physica C., to be
57 published.
58
59 [87]. TSEI, C.C., KIRTLEY, J.R., RUPP, M., SUN, J.Z., GUPTA, A., KETCHEN, B., WANG, C.A., REN,
60 Z.F., WANG, J.H. and BHUSHAN, M., 1996, Science, **271**, 329.
[88]. LESUEUR, J. APRILI, M., GRISON, X. AYACHE, J., KIM S. J. and THOREL, A., 1999, EdP Sciences,

- 1
2
3 J. Phys. IV, Pr4, 207.
4
5 [89]. WEN, J. G., TAKAGI, T AND KOSHIZUKA, N., 2000, Supercond. Sci. Technol. **13**, 820
6
7 [90]. GRAY, K.E., MILLER, D.J., FIELD, M.B., KIM, D.H. and BERGHUIS, P., 2000, Physica C, **341-348**,
8
9 1397.
10 [91]. TSU, I.F., WANG, J.L., KAISER, K.L. and BABCOCK, S.E. 1998, Physica C. **306**, issues 3-4, 163.
11 [92]. BABCOCK, S.E., CAI, X.Y., LARBALESTIER, D.C., SHIN, D.H., ZHANG, N., ZHANG, H., KAISER
12 D.L. and GAO Y., 1994, Physica C, **227**, 183.
13 [93]. JAGANNADHAN K AND NARAYAN.J, 1991, Materials Science and Engineering., **B8**, 201
14 [94]. JIA.C. L AND URBAN K., 1993, interface science, **1**, 291
15 [95]. ZHU, Y.Z., WANG, Z.L. and SUENAGA, M., 1993, Phil. Mag. **A 67**, n° 1, 11.
16 [96]. ZHU, Y.Z., CORCORAN, Y.L. and SUENAGA, M. 1993, Interface Science **1**, 361.
17 [97]. ZHU, Y. Z., 1996, Materials Science Forum, vol **207-209**, 377.
18 [98]. BROWNING, N.D., CHISHOLM, M.F. and PENNYCOOK, S.J., 1993, Interface science **1**, 309.
19 [99]. BROWNING, N.D., BUBAN, J.P., NELLIST, P.D., NORTON D.P., CHISHOLM, M.F. and PENNYCOOK,
20 S.J., 1998, Physica C, **294**, 183.
21 [100]. CHAN, S. W., HWANG, D. M and NAZAR, L., 1989, J. Appl. Phys. **65**. 4719.
22 [101]. CHAN, S. W., HWANG, D. M., RAMESH, R., SAMPERE, S. M., NAZAR, L. AND GERHRARDT, R
23 and PRUNA, P., 1989, High Temperature Superconductor Thin Films : Processing,
24 Characterization and Applications. Edited by Stockbaur. R. AIP proceeding 200, New
25 York.
26 [102]. BABCOCK, S.E., CAI, X.Y. and LARBALESTIER, D.C., 1990, Nature **347**, 6289.
27 [103]. CHAN, S.W., 1996, Materials Science Forum, Vols **207-209**, 79.
28 [104]. LARBALESTIER, D. C. et al, 1988, Physica C, **153-155** 1580.
29 [105]. SENOUSI, S. OUSSENA, M., AGUILLON, C. and TREMBLAY, P., 1988, J. Phys., **C8, 12**, 49 2099.
30 [106]. SMITH, D.S., SUASMORO, S., GAULT, C., CAILLAUD, F. and SMITH, A., 1990, Rev. Phys. Appl.
31 **25**, 90.
32 [107]. LAVAL, J. Y., DROUET, M., SWIATNICKI, W., GRADYS, E., SCHIFFMACHER, G., MONOT, I and
33 DESGARDIN, G., 1996, Mat. Sci.Forum, Vols **207-209**, 737.
34 [108]. GUREVICH, A. AND PASHITSKII, 1998, Phys. Rev. **B57**, 21, 13878.
35 [109]. AYACHE, J., KISIELOWSKI, C., KILAAS, R., PASSERIEUX, G. AND LARTIGUE-KORINEK, S.,
36 (2005) Journ. of Mater. Sci. **40** 3091.
37 [110]. KLIE, R. F., BELEGGIA, M., ZHU, Y., BUBAN, J. P. AND BROWNING, N.D., (2003), Phys. rev.
38 **B68**, 214101.
39 [111]. KLIE, R. F., BUBAN, J. P., VARELA, M., FRANCESCHETTI, A., JOOSS, C., BROWNING, N.D.,
40 PANTELIDES, S. T. AND PENNYCOOK, S. J., 2005, NATURE, 435, 475.
41 [112]. HAGENBECK, R. AND WASER, R., (1998), Journ. of Appl. Phys., **83**, 4, 2083.
42 [113]. DIMOS, D., CHAUDHARI, P., MANNHART, J. and LEGOUES, F.K., 1988, Phys. Rev. Lett., **61**,
43 n°2, 219.
44
45
46
47
48
49
50
51
52
53
54
55
56
57
58
59
60

- 1
2
3 [114]. CHAUDHARI, P. 1991, *Physica C* **185-189**, 292.
4
5 [115]. DAYEM, A. H. and WIEGAND, J. J., 1967, *Phys. Rev.* **155**, 419.
6
7 [116]. PLYANSKII, A.A., GUREVICH, A., PASHITSKI, A.E., HEINIG, N.F., REDWING, R.D., NORDMAN,
8 J.E. and LARBALESTIER, D.C., 1996, *Phys. Rev. B* **53**, 8687.
9
10 [117]. GUREVICH, A. and COOLEY, L. D., 1994, *Phys. Rev.* **B50**, 13563.
11
12 [118]. MANNHART, J., BIELEFELDT, H., GOETZ, B., HILGENKAMP, H., SCHMEHL, A., SCHNEIDER, C.
13 W. AND SCHULZ, R. R., 2000, *Physica C* **341-348**, 1393.
14
15 [119]. HAMMERL, G., SCHMEHL, A., SCHULZ, R. R., GOETZ, B., BIELEFELDT, H., SCHNEIDER, C. W.,
16 HILGENKAMP, H. AND MANNHART, J., (2000), *Nature* **407**, 162.
17
18 [120]. DUSCHER, G. BUBAN, J.P. BROWNING, N.D. CHISHOLM, M.F. PENNYCOOK, S.J., 2000, *Interface*
19 *Science*, **8**, 199 .
20
21 [121]. GUTH, H., KREBS, H. U., FREYHARDT, H. C. AND JOOSS, CH., (2001), *Phys. Rev.* **B64**, 140508.
22
23 [122]. DANIELS, G. A., GUREVICH, A. AND LARBALESTIER, D. C., (2000), *Appl. Phys. Lett.* **77**, 20,
24 3251.
25
26 [123]. HOLZAPFEL, B., VEREBELYO, D., CANTONI, C., PARANTHAMAN, M., SALES, B., FEENSTRA, D.
27 C. AND NORTON, D. P., 2000, *Physica C* **341-348**, 1431.
28
29 [124]. SCHOFIELD, M. A., BELEGGIA, M., ZHU, Y., GUTH, K. AND JOOSS, C., 2004, *Phys. Rev.*
30 *Lett.* **92**, 19, 195502.
31
32 [125]. SU, H AND WELCH, D. O., 2005, *Supercond. Sci. Technol.*, 18 24.
33
34 [126]. FIELD, M.B., LARBALESTIER, D.C., PARIKH, A. S. and SALAMA, K., 1997, *Physica C* **280**, 221.
35 and FIELD, M.B.(Thesis).
36
37 [127]. IVANOV, Z. G., NILSSON, P.A., WINKLER, D., ALARCO, J.A., CLEASON, T., STEPANTSOV, E.A.
38 and TZALENCHUK, A.Y., 1991, *Appl. Phys. Lett.* **59**, 3030.
39
40 [128]. HEINIG, N. F., REDWING, R. D., TSU, I. F., GUREVICH, A., NORDMAN, J. E., BABCOCK, S. E., and
41 LARBALESTIER, D. C., 1996, *APPL. PHYS. LETT.*, **69**, 577 and HEINIG, N. F. (THESIS).
42
43 [129]. STEEL, D. G., HETTINGER, J. D., MILLER, D. J., YUAN, F., GRAY, K. E., KANG, J. H. AND
44 TALVACCHIO, J., 1996, *Appl. Phys. Lett.*, **68**, 120.
45
46 [130]. HILGENKAMP H., MANNHART J. and MAYER, B., 1996, *Phys. Rev.B* **53**, 21, 14586.
47
48 [131]. BABCOCK, S.E. and VARGAS, J.L., 1995. *Annu. Rev. Mater. Sci.*, **25**, 193.
49
50
51
52
53
54
55
56
57
58
59
60

Figure Captions

Figure 1: The various types of superconducting ceramics synthesized during the past decade with their respective J_c values: classical bulk ceramics, melt-textured bulk ceramics, bulk bicrystals, thin film bicrystals, thin films and single crystals. Note that the three bottom configurations are governed by controlled orientations.

Figure 2: Representation of a S/I/S junction with its characteristics for the Low T_c and High T_c superconductivity mechanisms.

Figure 3: (a) Structural unit-cell of the (123) phase showing CuO_2 planes and Cu-O chains. (b) Based on the $d_{x^2-y^2}$ symmetry of the superconducting order parameter, a schematic diagram of the strong coupling along [100] and [103] orientations, as opposed to the weak coupling along [001] and [110].

Figure 4: (a) Tetragonal and orthorhombic unit-cells of the (123) phase. (b) Evolution of the lattice parameter as a function of the oxygen deficiency d for various oxygen partial pressures. Note the change in the transition for temperatures between 798K and 943K [6].

Figure 5: Ternary phase diagram of the $\text{BaO-Y}_2\text{O}_3\text{-CuO}$ system showing the various possible secondary phases (132), (211).

Figure 6: Structural phase diagram of the (123) phases displaying the effect of oxygen partial pressure and of temperature on the formation of the (123) oxygen stoichiometric phase [6].

Figure 7: (7a) Oxygen diffusion depth profiling on a ceramic polished with a small angle ($\theta = 1.56^\circ$, $T = 823\text{K}$, $p\text{O}_2 = 22\text{kPa}$) exhibiting the presence of microcracks.

(7b) Ionic image obtained with O^{18} showing the anisotropy of oxygen diffusion.

(7c) Arrhenius plots of volume and grain boundary diffusion in ceramics along (ab) planes and parallel to the c axis in a single crystal. Full triangles up and down represent respectively the coefficient of volume diffusion in the c direction and in (ab) planes [21]. Diamonds represent the diffusion coefficient in polycrystals [23]. Squares and stars represent respectively volume diffusion and grain boundary diffusion [20]. Crosses represent the chemical diffusion coefficient taken from [22].

1
2
3
4
5 **Figure 8** : R(T) measurements on A_0 , A_1 , B_0 and B_1 samples sintered under various
6 conditions. The transition width becomes larger as T_c decreases, revealing a low oxygen
7 content, a low homogeneity in the ceramic and the presence of secondary phases at grain
8 boundaries.
9
10

11
12
13 **Figure 9** : (a) TEM image of ceramic A_1 showing a grain surrounded by several clean GB's .
14 (b) : HREM lattice image of a small angle (4°) GB exhibiting (001) planes. (c) : TEM image
15 of a clean triple junction showing twinning inside the grains. (d) HREM lattice image of some
16 faceted GB exhibiting (001) planes in one grain.
17
18
19
20
21

22 **Figure 10** : TEM and HREM lattice images of ceramic B_0 exhibiting the change of a high
23 angle grain boundary (a) from a symmetrical faceted GB (b) to an asymmetrical one (c)
24 near an intergranular defect. Both GB's have a misorientation close to CSL $\Sigma 13$ (67° - 69°).
25
26
27
28

29 **Figure 11** : Optical micrographs (a), SEM (b), TEM image and electron diffraction patterns
30 (c and d) for ceramic B_1 , exhibiting morphologies resulting from the grain size gradient
31 produced by the sintering. Note that twins formed in the external part of the ceramic are
32 completely relaxed (left part of figure c) and have an oxygen content close to O_7 as
33 measured by the splitting of the 110 reflections (insert in diffraction pattern (c)). Twins of the
34 inner part of the ceramic are of the ferroelastic type (left part of figure d). They are not
35 completely relaxed by the phase transformation as deduced from the absence of splitting of
36 the 110 reflections (right part of figure d) and their oxygen content is close to $O_{6.5}$.
37
38
39
40
41
42
43
44
45

46 **Figure 12** : Critical current density J_c measured as a function of the grain size in bulk
47 ceramics. A_0 , A_1 , B_0 and B_1 samples correspond to hot-press sintering and sample (C) to a
48 low density material made by classical sintering.
49
50
51
52

53 **Figure 13** (a) Polarized optical image showing two large domains with a low misorientation
54 of about 10° , observed in a YBCO melt-textured ceramic synthesized under magnetic field.
55 (b) : TEM micrograph of (a) exhibiting coherent and incoherent twins crossing a line defect.
56 This growth defect, filled with liquid during (123) growth, keeps the same orientation, parallel
57 to the (001) superconducting planes. (c) : Optical micrograph of a YBCO melt-textured
58 ceramic grown on a Y_2O_3 polycrystalline substrate. This image shows four different domains
59
60

1
2
3 with a large GB misorientation in its centre. Characteristic clean interfaces are formed
4 between two (211) precipitates and (123) phases as seen in figure d.
5
6
7

8 **Figure 14 :** (a) Polarized light micrograph of a melt-textured ceramic grown on a Y_2O_3
9 substrate exhibiting white bands in the ceramic microstructure, and a 90° HAGB in its centre.
10 Light lines correspond to (110) and (-110) twin planes. A non-uniform distribution of the
11 twin widths can be observed. (b) : TEM micrograph of the same GB showing faceting along
12 (100) and (110) planes. There are regions with 90° tilt symmetrical and asymmetrical GB's.
13
14
15
16

17
18 **Figure 15 :** TEM image of a (123) phase / (211) precipitate interface damaged due to the
19 presence of carbon impurities in the MgO substrate and due to carbon diffusion in the liquid.
20
21
22

23
24 **Figure 16 :** YBCO Thin films grown by co-evaporation respectively on a $SrTiO_3$ (a, b, and c)
25 and on a MgO substrate (d, e and f). (a and d) AFM images showing the growth islands.
26 (b) and (e) : TEM planar view image which shows large areas of the same [001] orientation in
27 films on STO, and various GB misorientations around the [001] direction with rotation angles
28 of 35° , $30,6^\circ$ and $62,7^\circ$ (visible by the twin rotation) for MgO. Both films exhibit 90° GB's
29 corresponding to twinning of the (ab) superconducting planes. (e) and (f) : Moires of the 100
30 and 010 reflections of the (123) phase with the substrates. One can notice that those present
31 on STO (c) show a residual strain in the (123) film appearing in chevron- shaped Moires with
32 various d-spacings, while those formed on MgO keep a constant value, indicating full
33 relaxation of the film.
34
35
36
37
38
39
40
41
42

43 **Figure 17 :** (a) TEM image of a YBCO $24^\circ \Sigma 13$ [001] tilt GB grown on a STO substrate,
44 exhibiting meandering of the GB plane. The electron diffraction pattern is visible in the
45 insert. (b) : HREM image of part of the overlapping zones corresponding to the superposition
46 of grain 1 on top of grain 2, or vice versa, along the YBCO GB. Note the faceting.
47
48
49
50

51
52 **Figure 18 :** AFM image of the same YBCO $24^\circ \Sigma 13$ [001] tilt GB. (a) corresponds to a laser
53 ablated thin film of 120nm thickness ; (b) co-evaporated thin film of 50nm thickness, grown
54 using a low deposition rate. The morphology of the growth-islands presents either square -
55 shaped growth terraces or not very clear faceting. Notice a 20 nm wide area with a weak
56 contrast of the island shapes, corresponding to the region of overlapping.
57
58
59
60

Figure 19 : (a) schematic representation of the terrace shape and of the holes due to island coalescence. (b) : model of moires at the grain boundary based on HREM quantitative analysis. The lateral extension of GB meandering on either side of the grain boundary plane depends on the growth conditions. It may vary from 10nm to 500nm.

Figure 20 : Models of large angle grain boundaries (a, b and c) : $\Sigma 37$, $\Sigma 13$, $\Sigma 5$ grain boundaries with coalesced configuration and exhibiting discontinuity of a-b lattice planes at the GB ; (d) $\Sigma 5$ (a-c) type GB showing continuity of lattice planes a and c [93].

Figure 21 : HREM image of $\Sigma 1$ 90° (100)/(001) interface projected along the [010] direction; (a) ,(b), (c): the three models of the grain boundary . **Model a :** grain 1 shows a (001) CuO_2 plane at the upper face, and grain 2 a (100) Y-Ba-O plane at the lower face. **Model b :** grain 1 shows a (001) Ba-O plane and grain 2 a (100) Cu-O plane. **Model c :** grain 1 shows a (001) CuO plane and grain 2 a (100) Ba-O-Y-O-Ba plane [94].

Figure 22 : Variation of oxygen content and lattice parameter in the vicinity of high angle grain boundaries corresponding to near $\Sigma 10$, $\Sigma 13$ and $\Sigma 26$ GB's. They present a departure from the perfect orientation varying from 3.24° to 10.90° [97].

Figure 23 : (a) EELS profile of the oxygen K pre-edge peak corresponding to the superconducting O_7 phase; (b): oxygen peak deficiency corresponding to the O_6 non-superconducting phase. (c) : Quantitative analysis of the normalized oxygen pre-peak showing oxygen deficiency in an asymmetrical GB (stars represent symmetrical and circles asymmetrical GB's) [100].

Figure 24 : Variation of the current density J_{CGB} of grain boundaries as a function of the misorientation angle between 1° and 45° in YBCO melt-grown bulk bicrystals [58].

Figure 25 : (a and b) Density of states for these two SrTiO_3 GB's (pristine). Notice the charge distribution in the dislocation cores for the low (a) and high (b) angle GB's. The smallest misorientation corresponds to the largest distance between the dislocations cores avoiding the overlap of the strain field [110]. (c) Charge distribution in a 4° [100] tilt boundary in Ca-doped (left) and undoped (right) YBCO [123].

Figure 26 : Variation of current density J_c as a function of GB misorientation in YBCO thin

1
2
3 film bicrystals [113].
4
5

6
7 **Figure 27:** Representation of a superconducting GB as an array of a large number of parallel
8 Dayem bridges simulating superconducting regions (B) separated by normal or non-
9 superconducting regions (A).
10
11

12
13 **Figure 28 :** Variation of current density J_c of bulk and thin film bicrystals as a function of
14 GB misorientation [91].
15
16

17
18 **Figure 29 :** Atomic resolution Z-contrast images of a pristine 4° [001] tilt grain boundary in
19 undoped and Ca-doped YBCO. (a) dislocation core with the typical pentagonal arrangement
20 of structural units found in SrTiO_3 . (b) Ca-doped YBCO GB where the Y/Ba pentagonal
21 column arrangement encloses three columns, two on the Cu-O and one on the Y/Ba sublattice.
22 (c and d) diagram of the core structure where EELS analysis was performed [111].
23
24
25
26
27

28
29 **Figure 30 :** Representation of grain boundaries found in thin films containing a combination
30 of symmetrically and asymmetrically faceted GB's. The critical current I_c across the grain
31 boundary changes locally between null and a maximum value depending on the local
32 crystallographic orientation of the GB faceting.
33
34
35

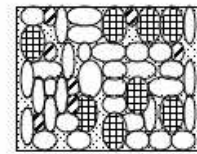
36
37 **Figure 31 :** (a) Model of the various GB geometries used for calculation; (b) Results from
38 calculations by Mannhart et al [130] compared with experimental data [113].
39
40
41
42
43
44
45
46
47
48
49
50
51
52
53
54
55
56
57
58
59
60

Tables

Table 1 : $\text{YBa}_2\text{Cu}_3\text{O}_{7-d}$ structures, related oxygen contents and critical temperatures. For $0.15 < d < 0.6$ various oxygen vacancies ordering occur.

Table 2 : Superconducting values for melt-textured YBCO ceramics prepared with a thermal gradient on a MgO substrate single crystal (sample D) and on a polycrystalline Y_2O_3 substrate (sample E).

Table 3 : GB's relative quality and J_c values for YBCO bulk, thin films, single and bicrystals.

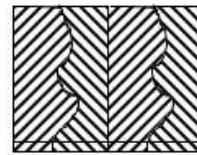


Classical ceramics

$$J_c < 10^3 \text{ A/cm}^2$$

Polycrystals

Solid-solid
Diffusion

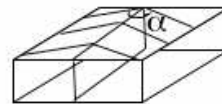


Melt textured ceramics

$$10^4 < J_c < 10^5 \text{ A/cm}^2$$

On polycrystalline substrates:
Y₂BaCuO₅, Y₂O₃, MgO, LaAlO₃

Solid-liquid
Diffusion

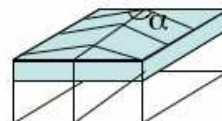


Bulk bicrystals

$$J_c = f(\alpha)$$

From YBCO Melt ceramics

Solid-liquid
Diffusion

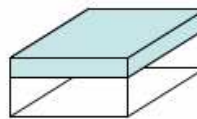


Thin film bicrystals

$$J_c = f(\alpha)$$

Grown on bicrystal substrates:
SrTiO₃, MgO, Y-ZrO₂

Solid-gas
reaction

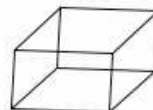


Thin films

$$10^6 < J_c < 10^7 \text{ A/cm}^2$$

On single crystal substrates:
SrTiO₃, MgO, LaAlO₃

Solid-gas
reaction

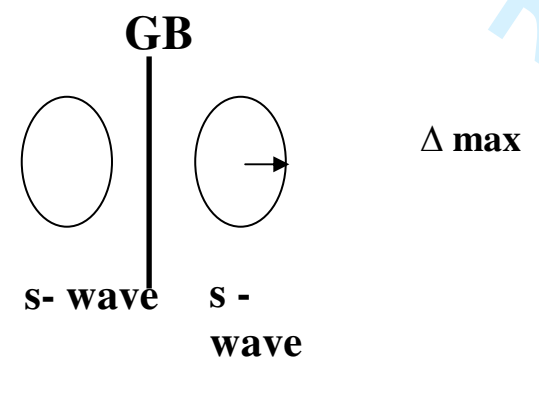


Single crystals

$$10^4 < J_c < 10^5 \text{ A/cm}^2$$

Solid-liquid
Diffusion
Flux growth

Figure 1

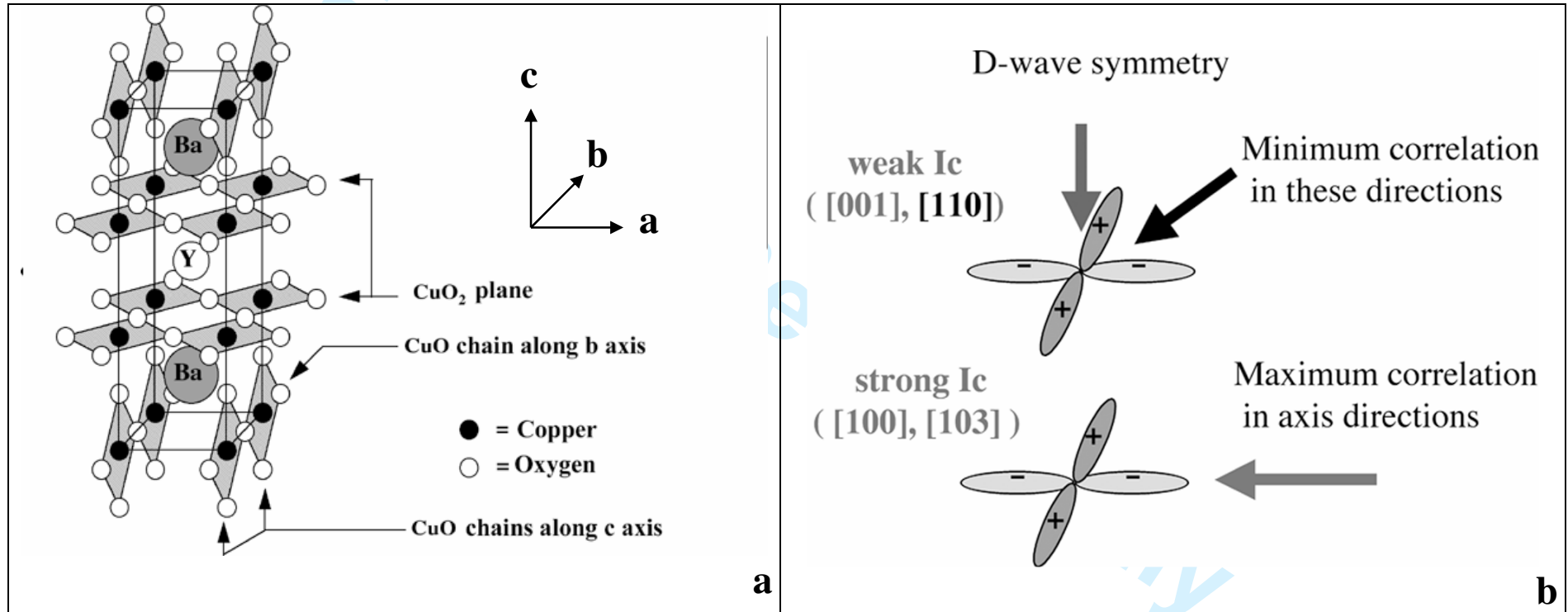


[010]

Figure 2

1
2
3
4
5
6
7
8
9
10
11
12
13
14
15
16
17
18
19
20
21
22
23
24
25
26
27
28
29
30
31
32
33
34
35
36
37
38
39
40
41
42
43
44
45
46
47

Figure 3



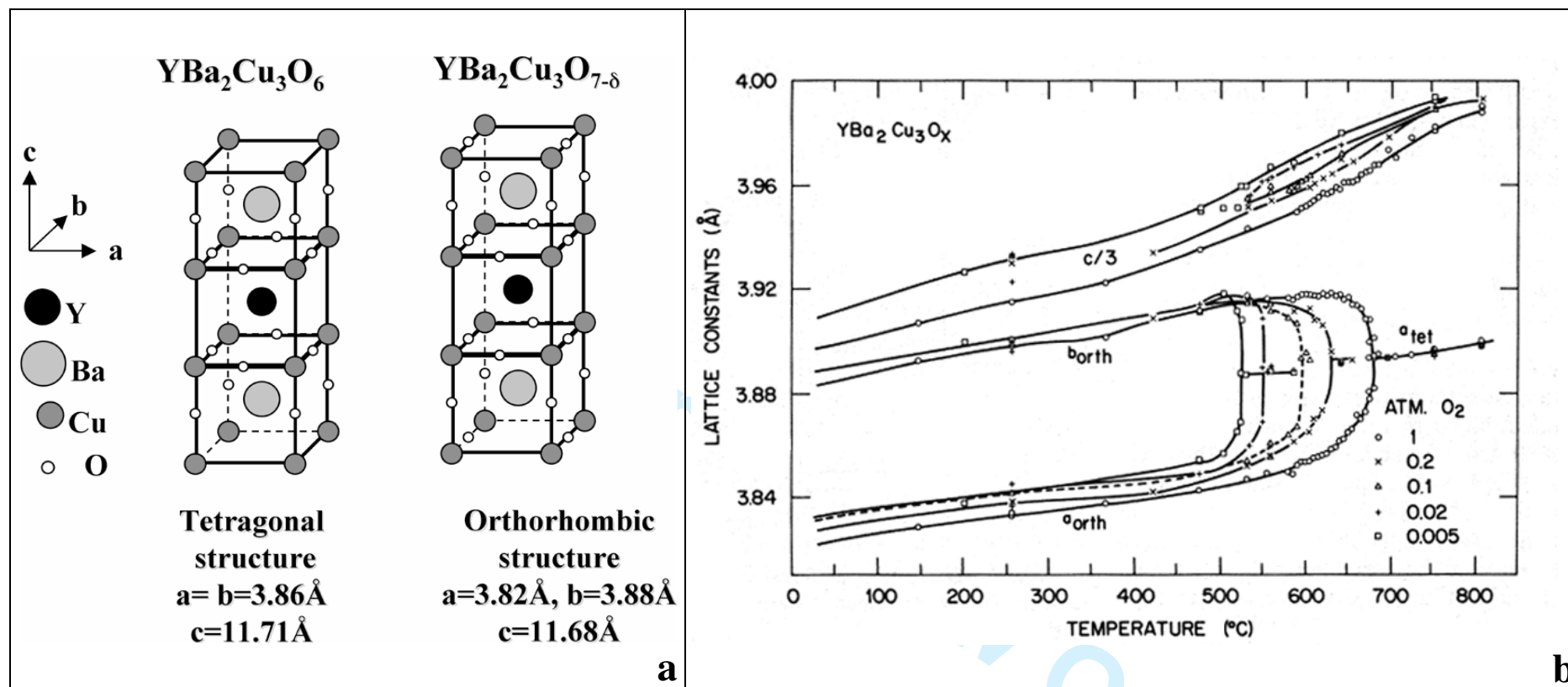
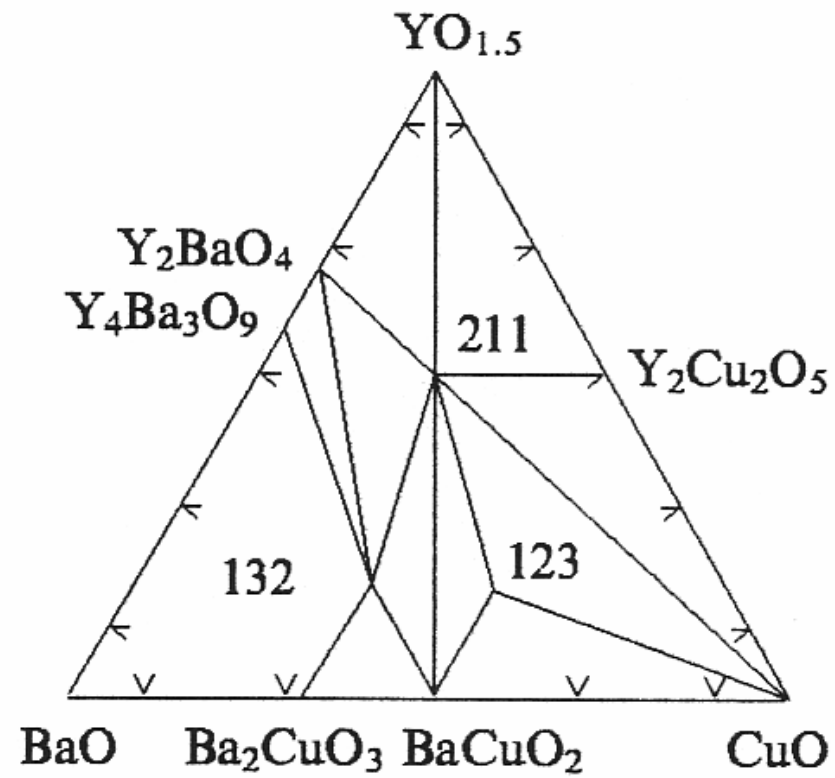


Figure 4

**Figure 5**

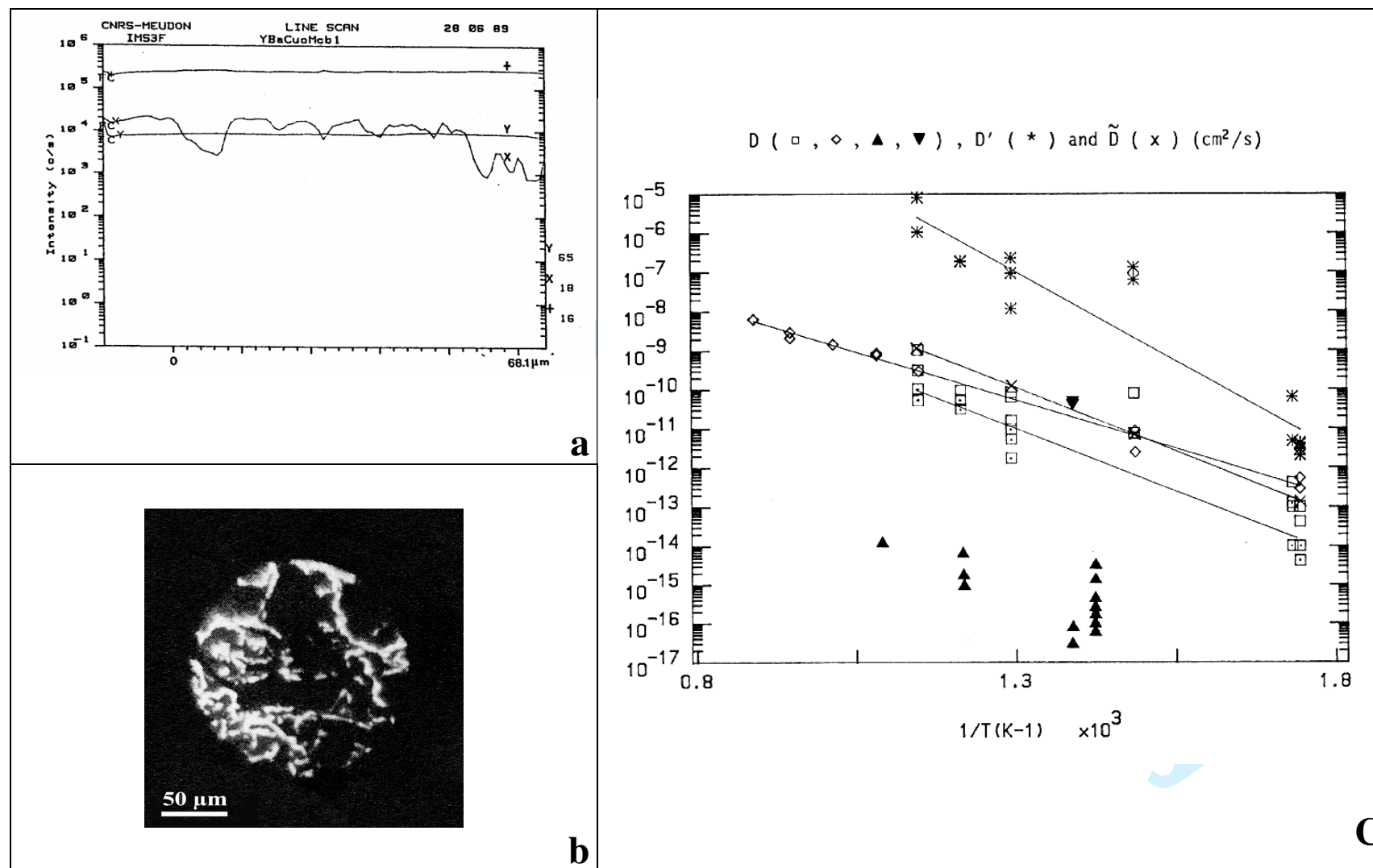


Figure 7

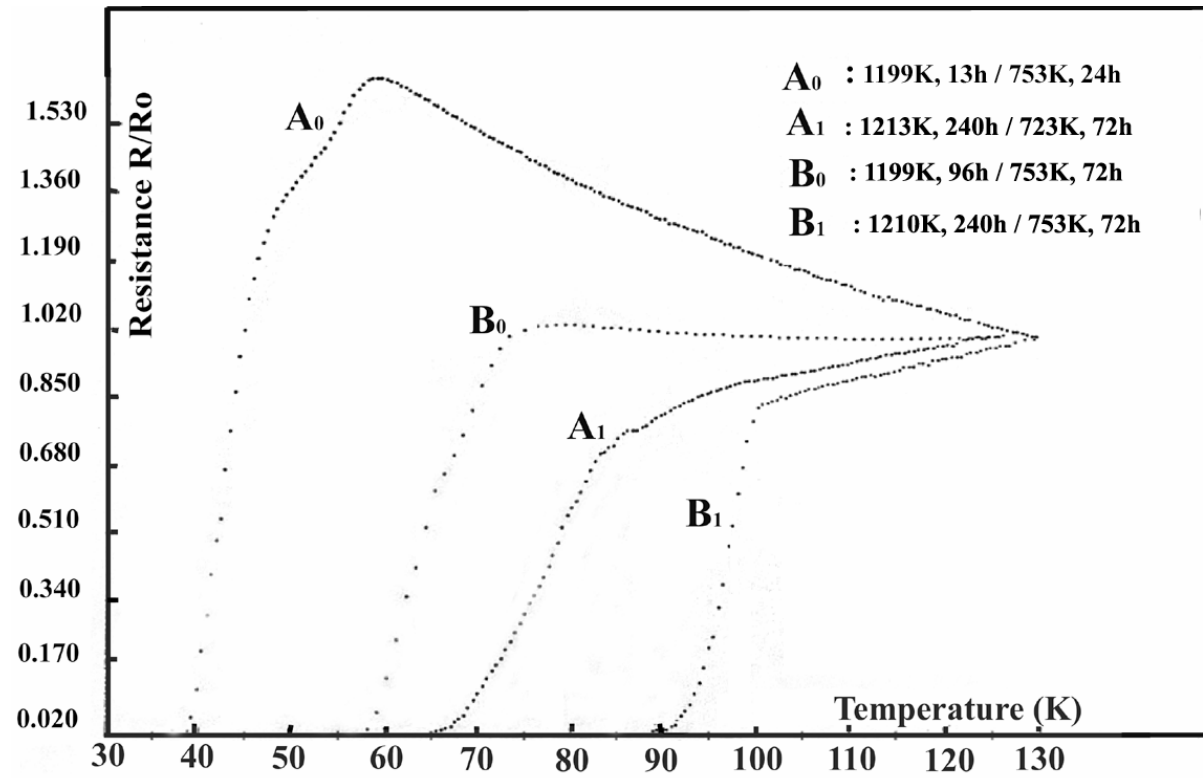
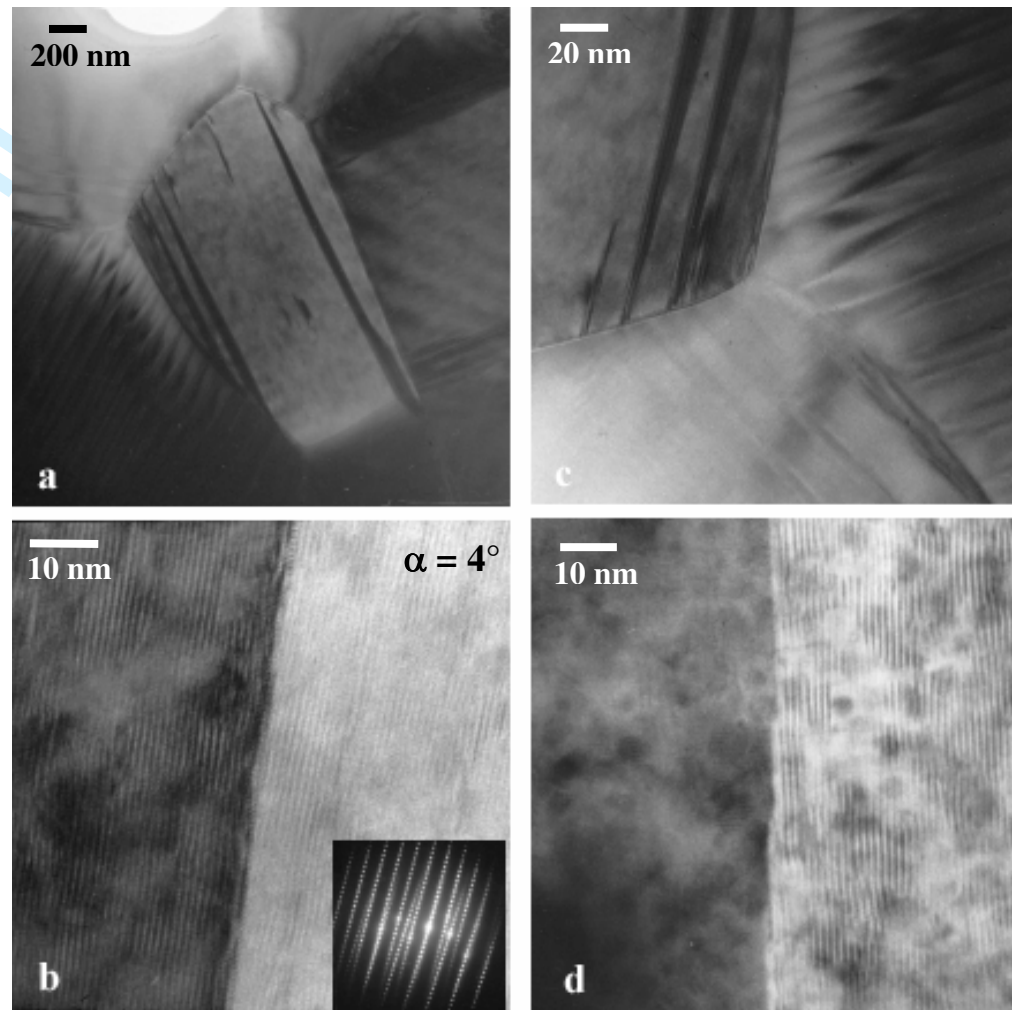


Figure 8

1
2
3
4
5
6
7
8
9
10
11
12
13
14
15
16
17
18
19
20
21
22
23
24
25
26
27
28
29
30
31
32
33
34
35
36
37
38
39
40
41
42
43
44
45
46
47

**Figure 9**

1
2
3
4
5
6
7
8
9
10
11
12
13
14
15
16
17
18
19
20
21
22
23
24
25
26
27
28
29
30
31
32
33
34
35
36
37
38
39
40
41
42
43
44
45
46
47

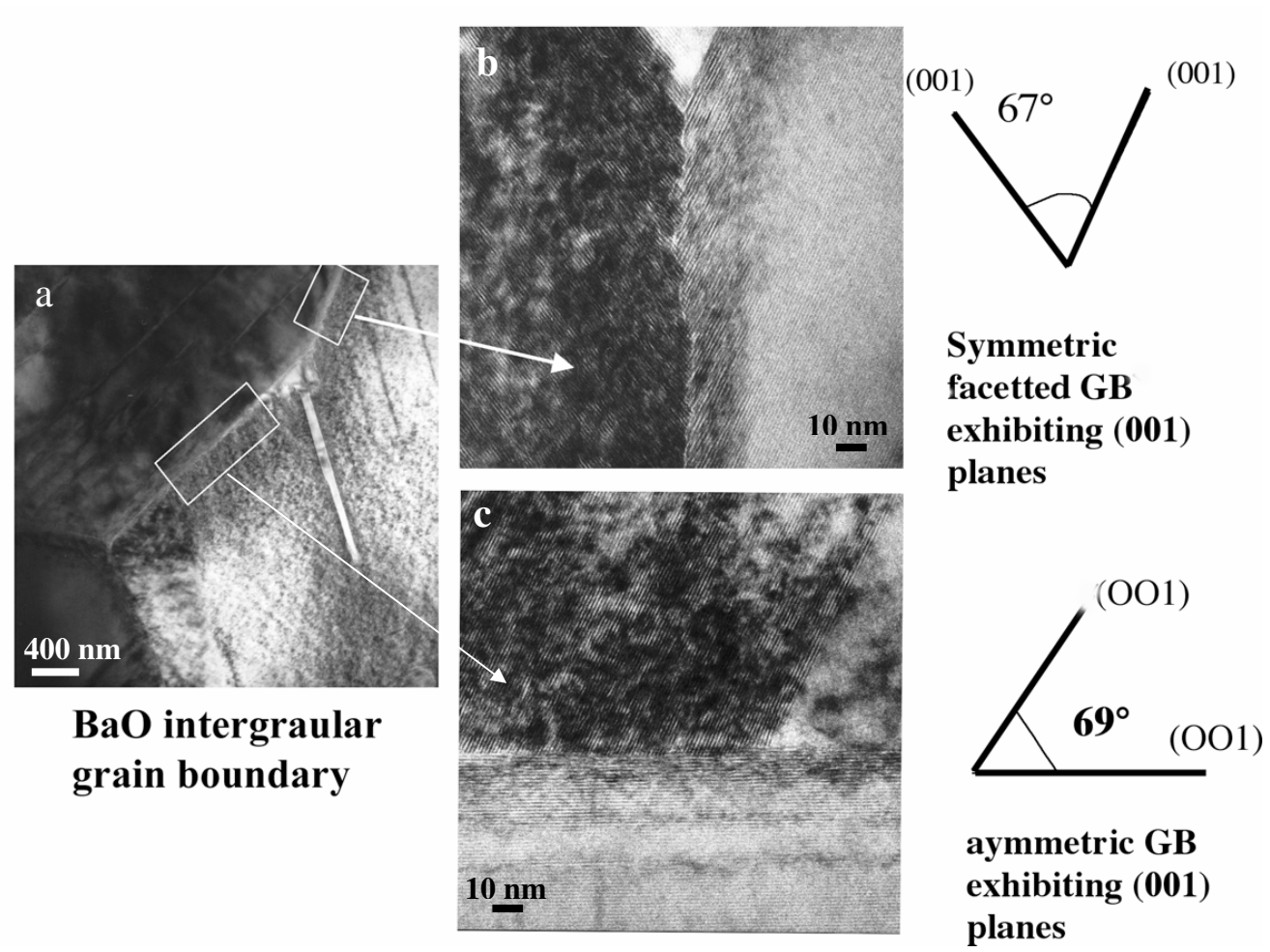


Figure 10

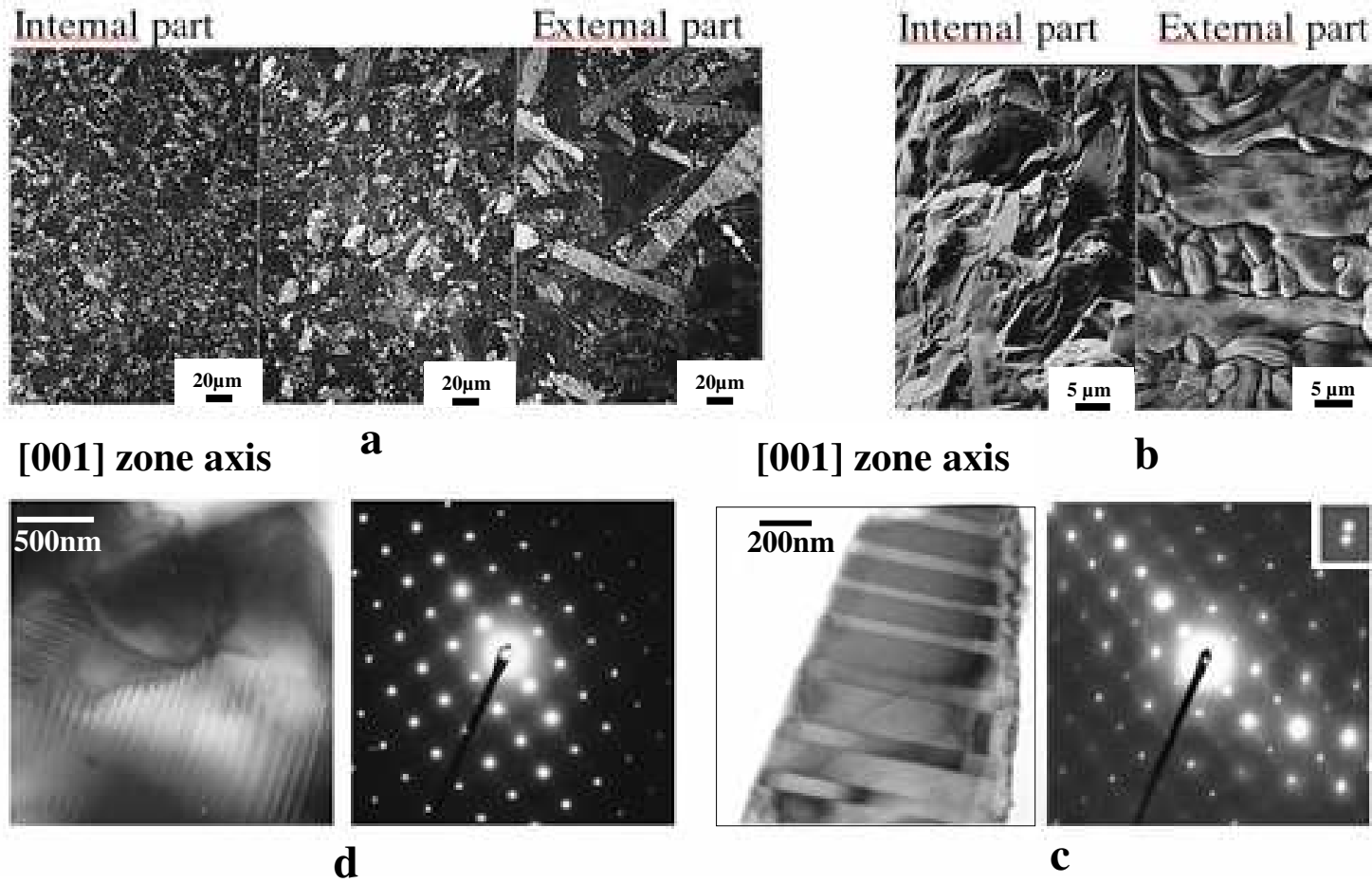


Figure 11

1
2
3
4
5
6
7
8
9
10
11
12
13
14
15
16
17
18
19
20
21
22
23
24
25
26
27
28
29
30
31
32
33
34
35
36
37
38
39
40
41
42
43
44
45
46
47

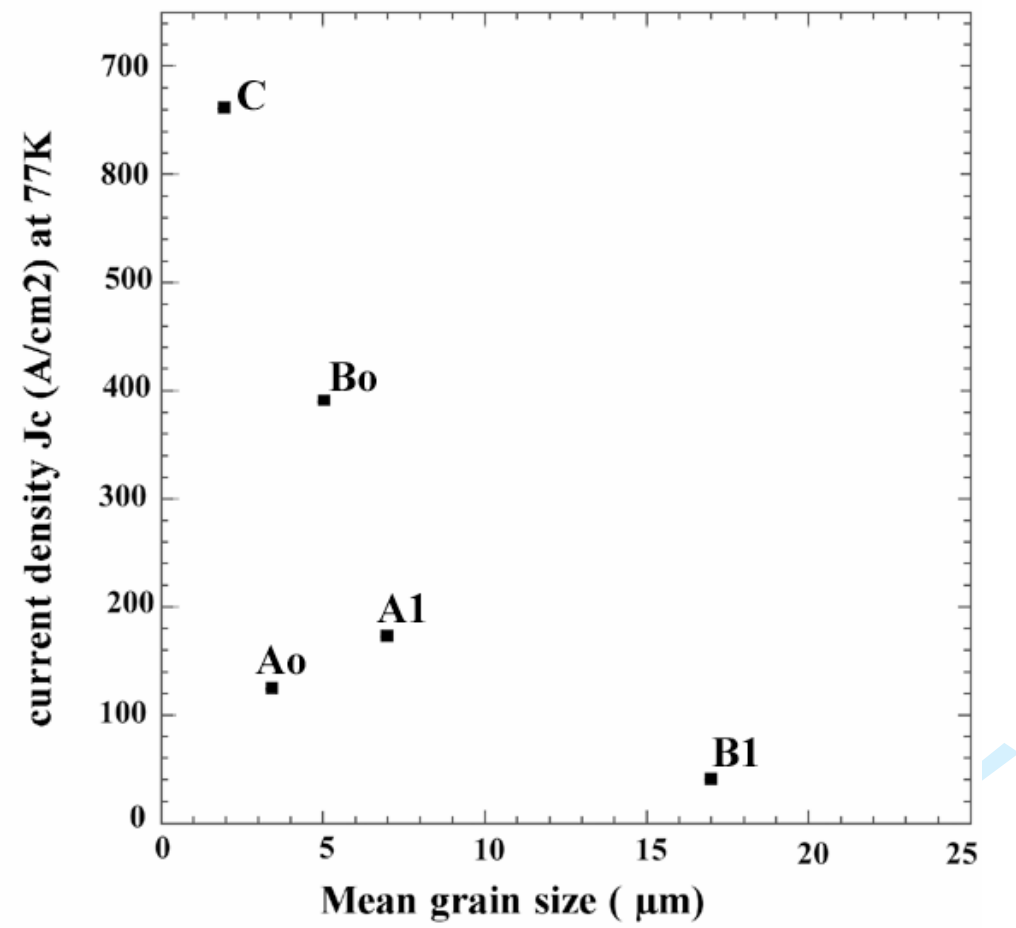
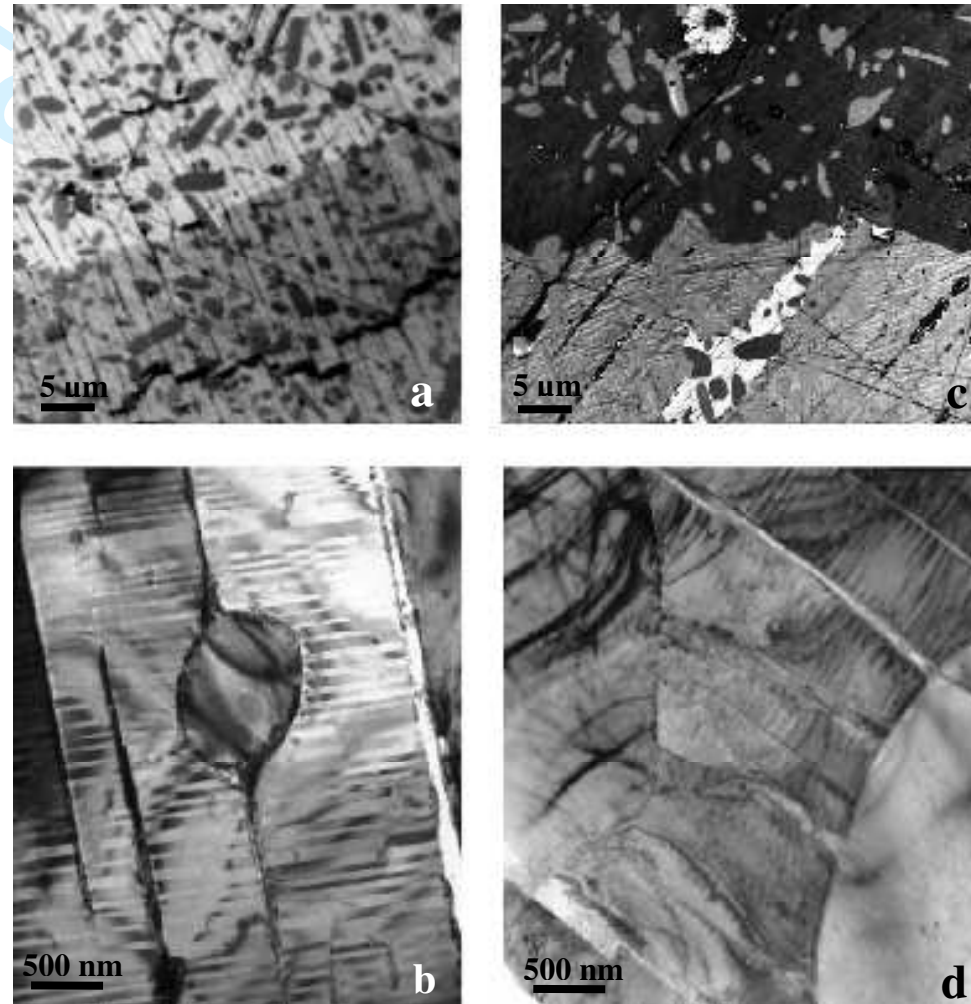


Figure 12

Figure 13

1
2
3
4
5
6
7
8
9
10
11
12
13
14
15
16
17
18
19
20
21
22
23
24
25
26
27
28
29
30
31
32
33
34
35
36
37
38
39
40
41
42
43
44
45
46
47

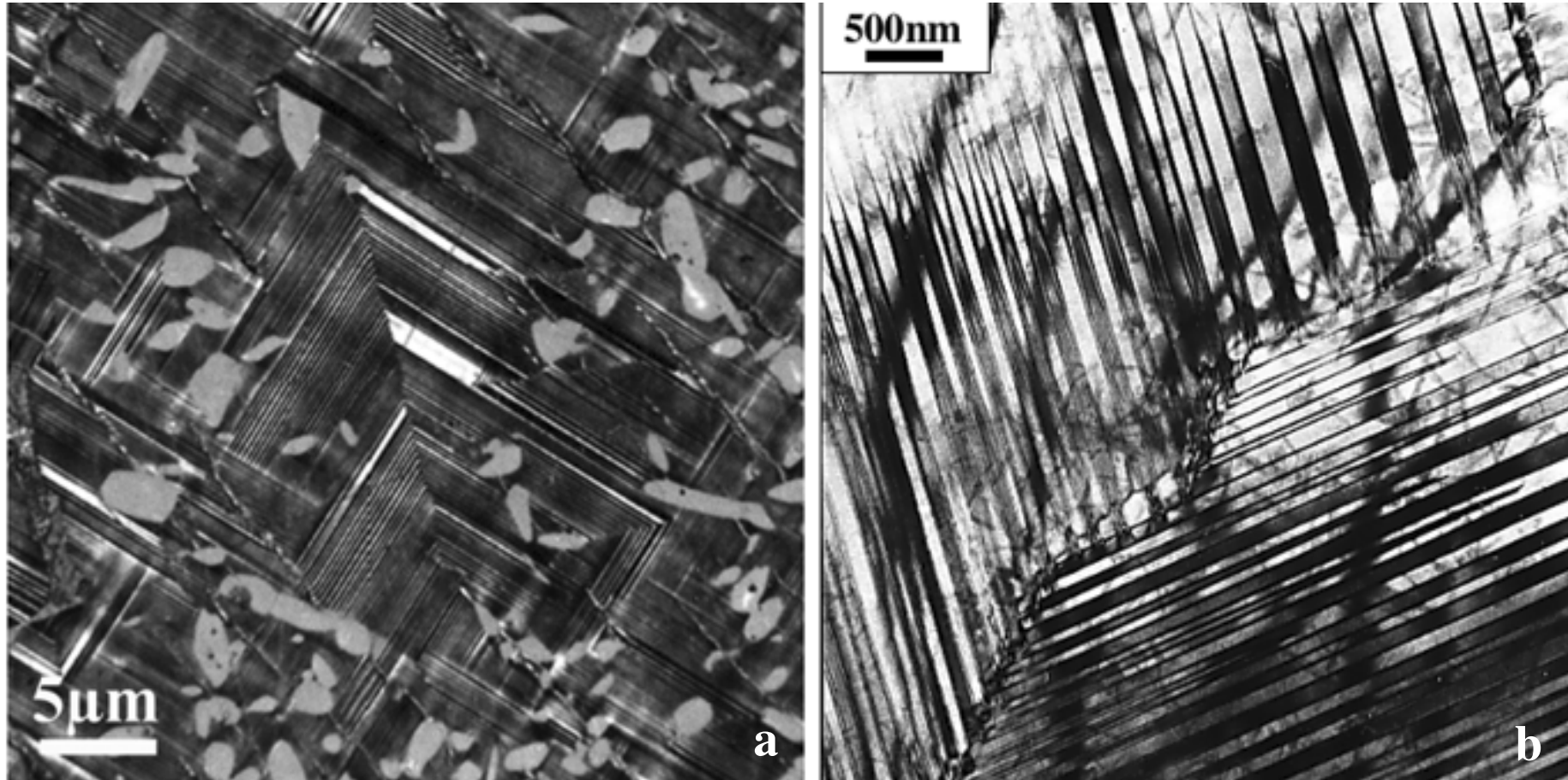


Figure 14

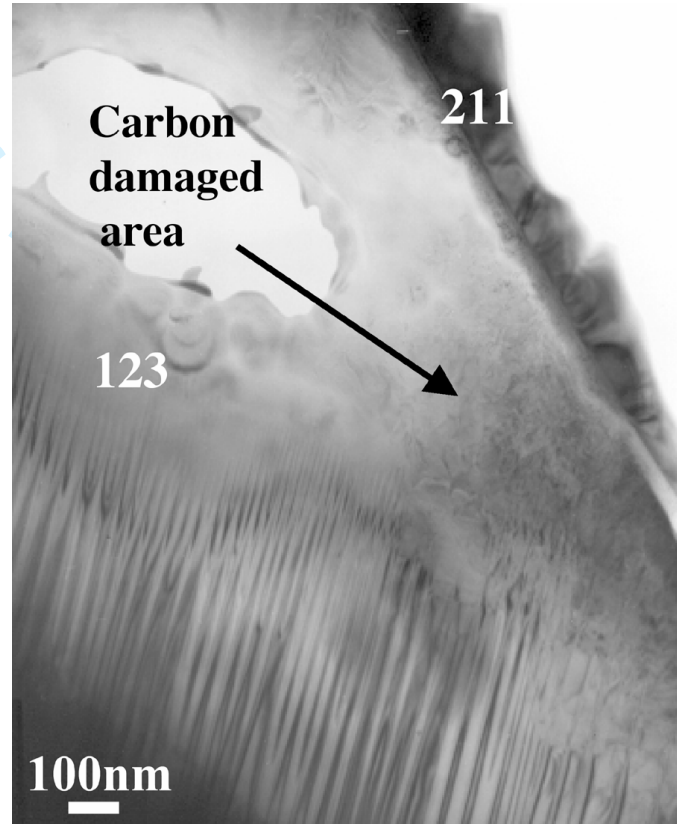


Figure 15

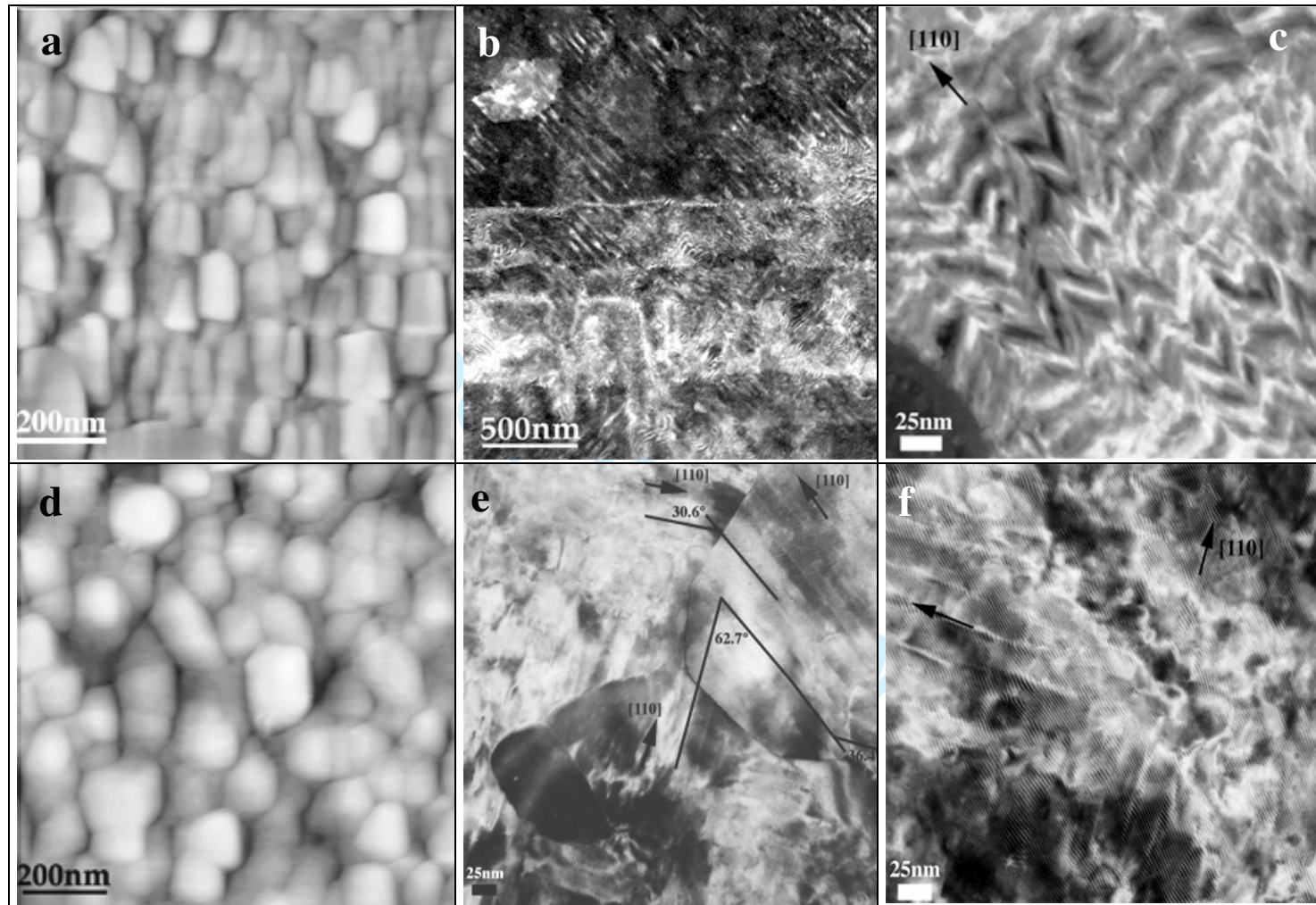


Figure 16

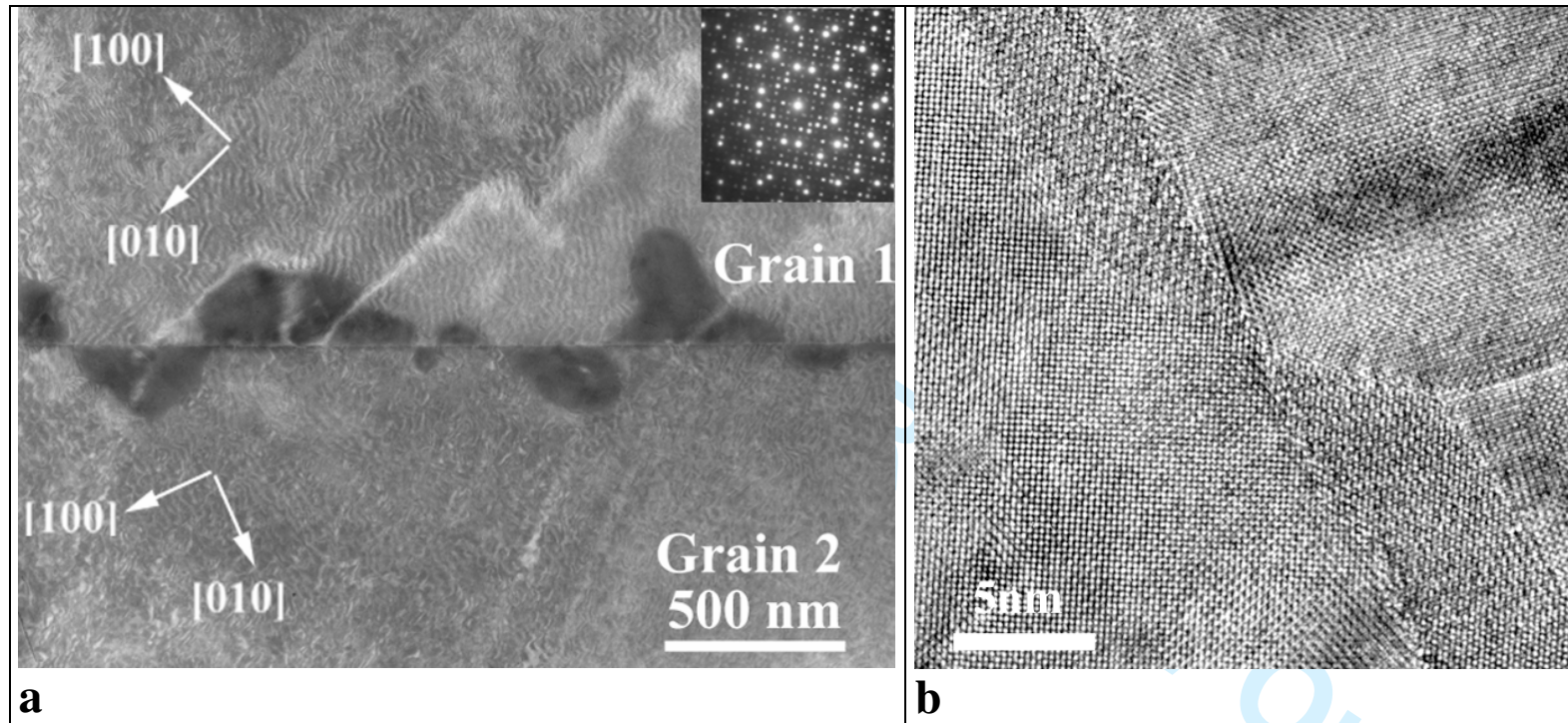


Figure 17

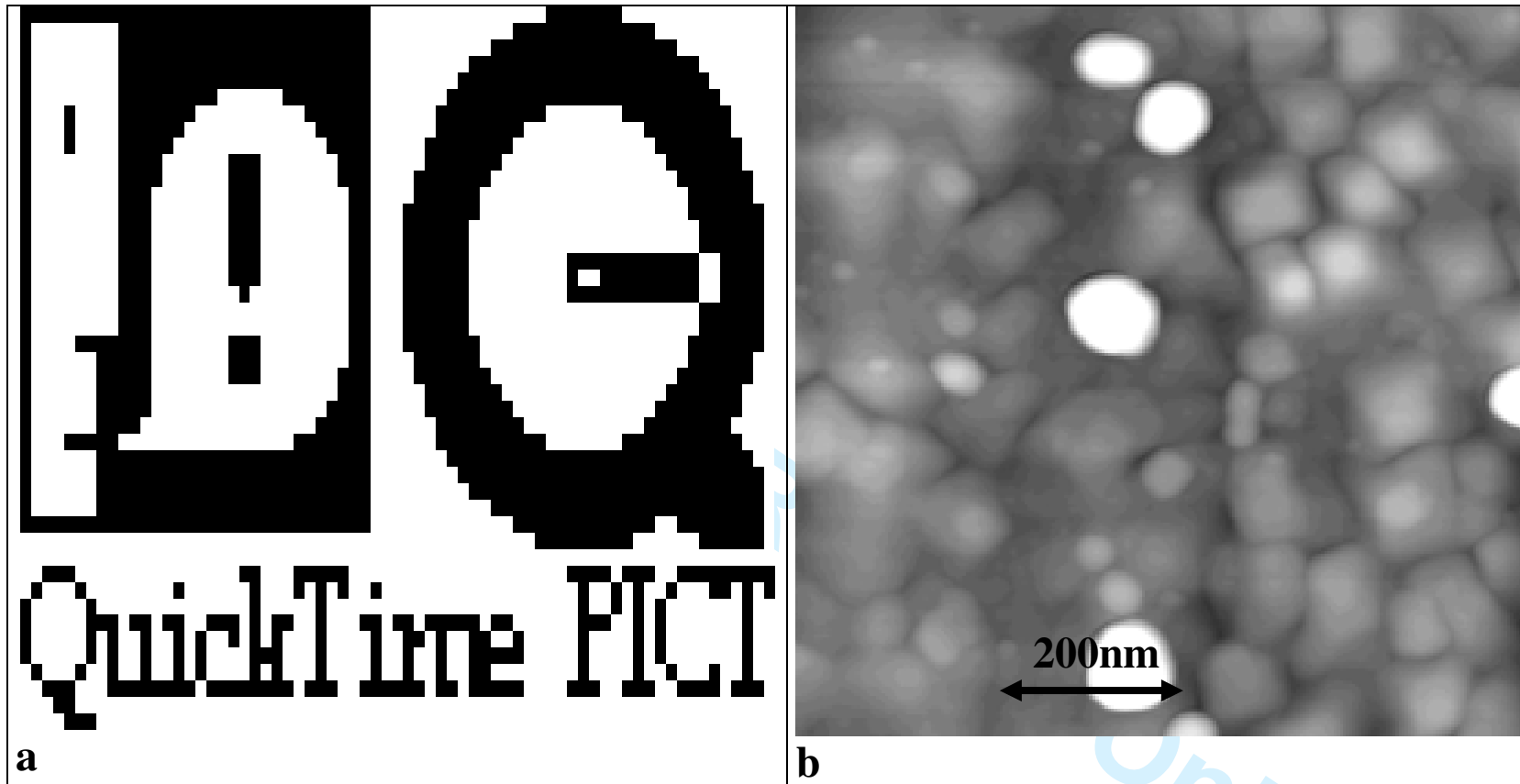


Figure 18

1
2
3
4
5
6
7
8
9
10
11
12
13
14
15
16
17
18
19
20
21
22
23
24
25
26
27
28
29
30
31
32
33
34
35
36
37
38
39
40
41
42
43
44
45
46
47

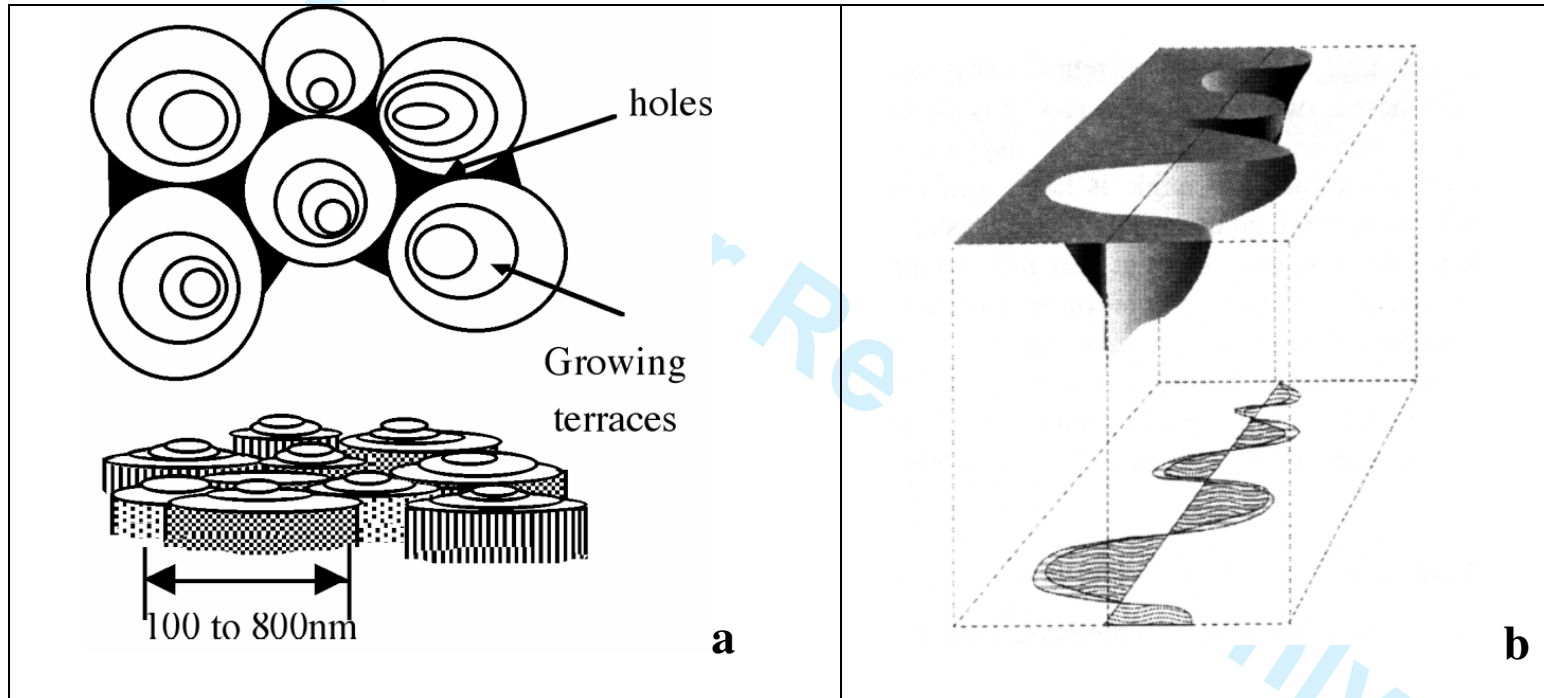


Figure 19

1
2
3
4
5
6
7
8
9
10
11
12
13
14
15
16
17
18
19
20
21
22
23
24
25
26
27
28
29
30
31
32
33
34
35
36
37
38
39
40
41
42
43
44
45
46
47

1
2
3
4
5
6
7
8
9
10
11
12
13
14
15
16
17
18
19
20
21
22
23
24
25
26
27
28
29
30
31
32
33
34
35
36
37
38
39
40
41
42
43
44
45
46
47

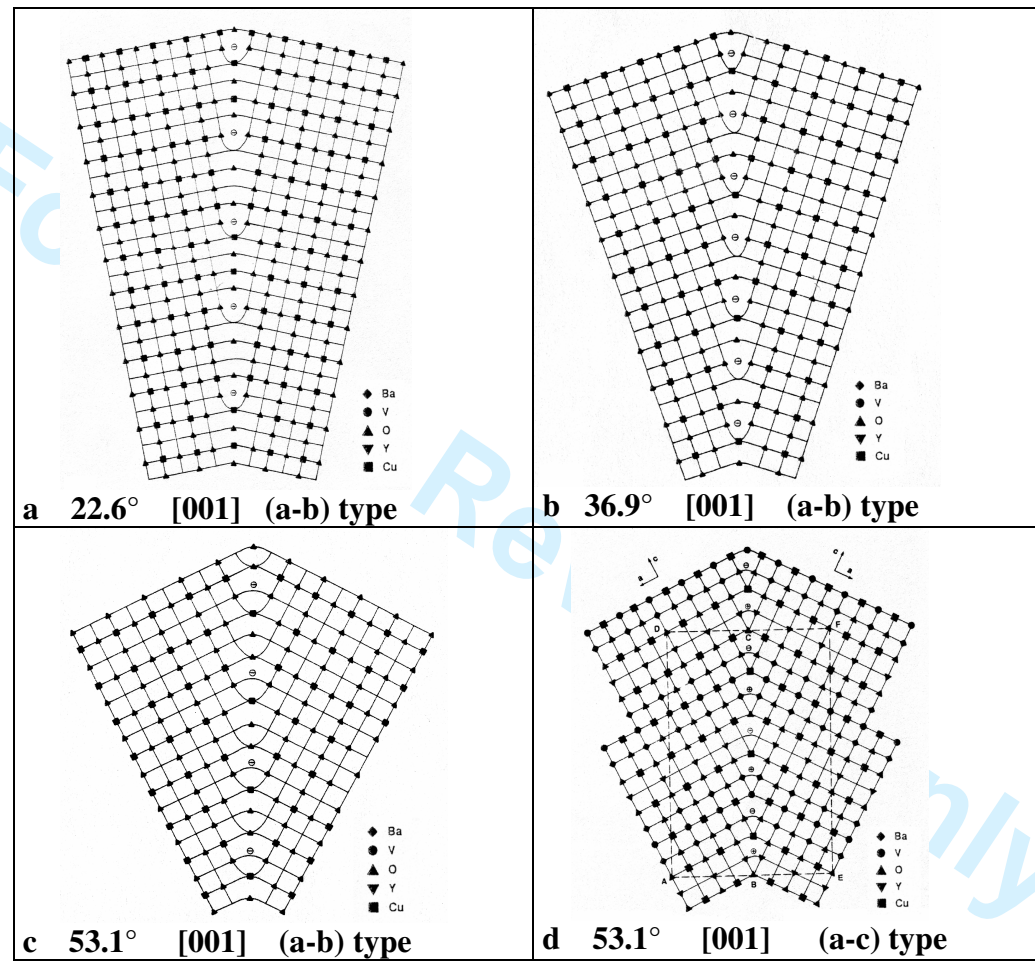


Figure 20

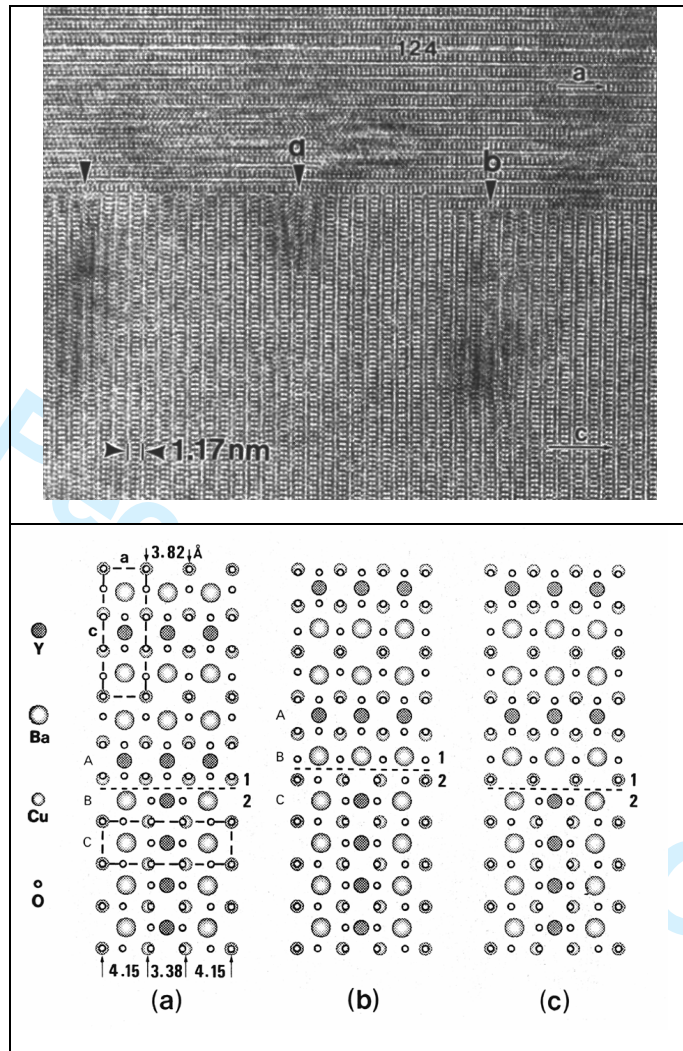


Figure 21

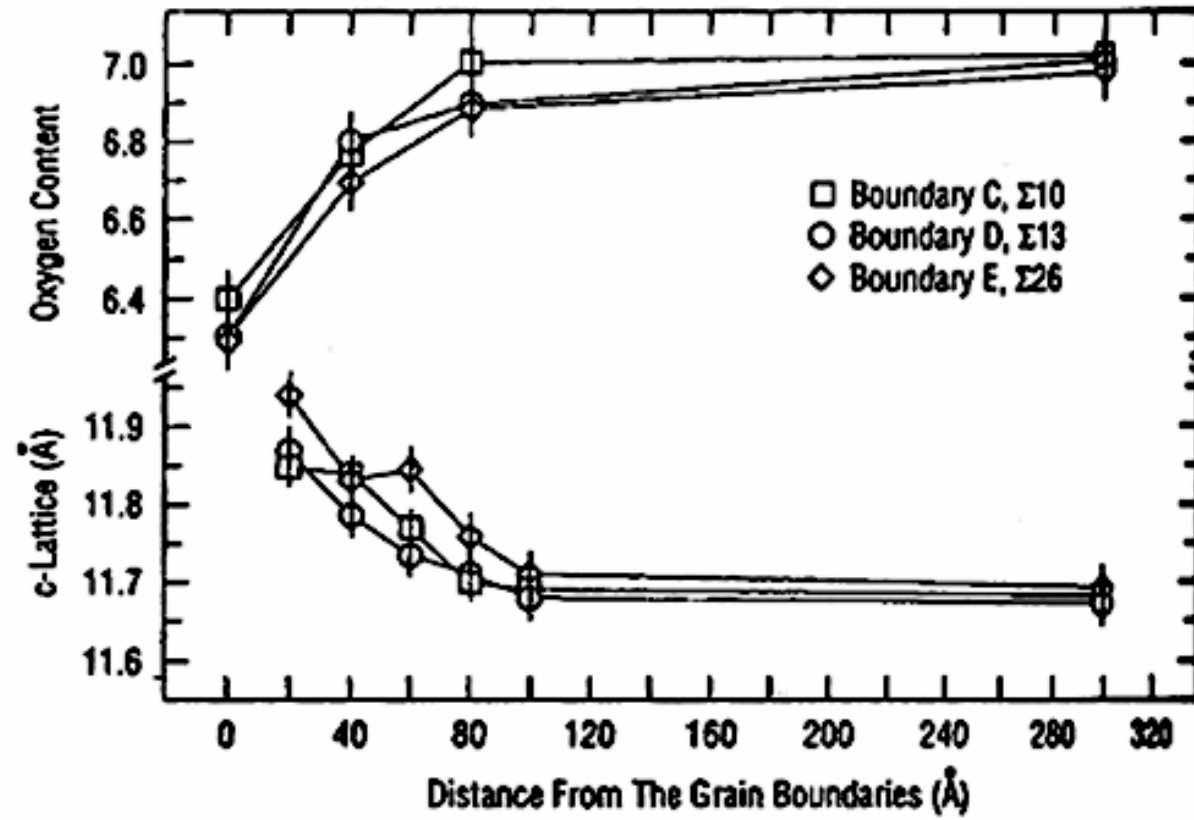


Figure 22

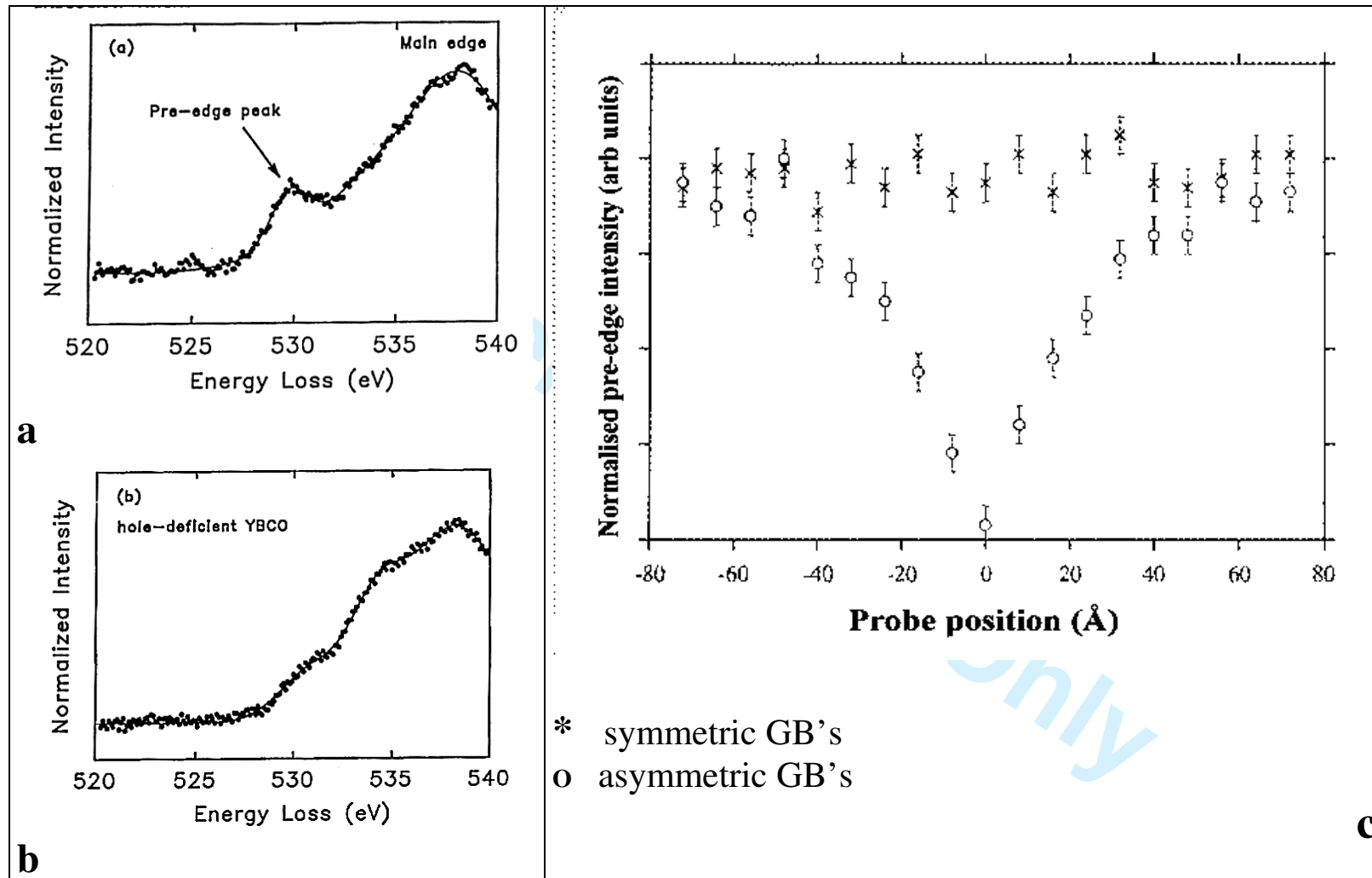


Figure 23

1
2
3
4
5
6
7
8
9
10
11
12
13
14
15
16
17
18
19
20
21
22
23
24
25
26
27
28
29
30
31
32
33
34
35
36
37
38
39
40
41
42
43
44
45
46
47

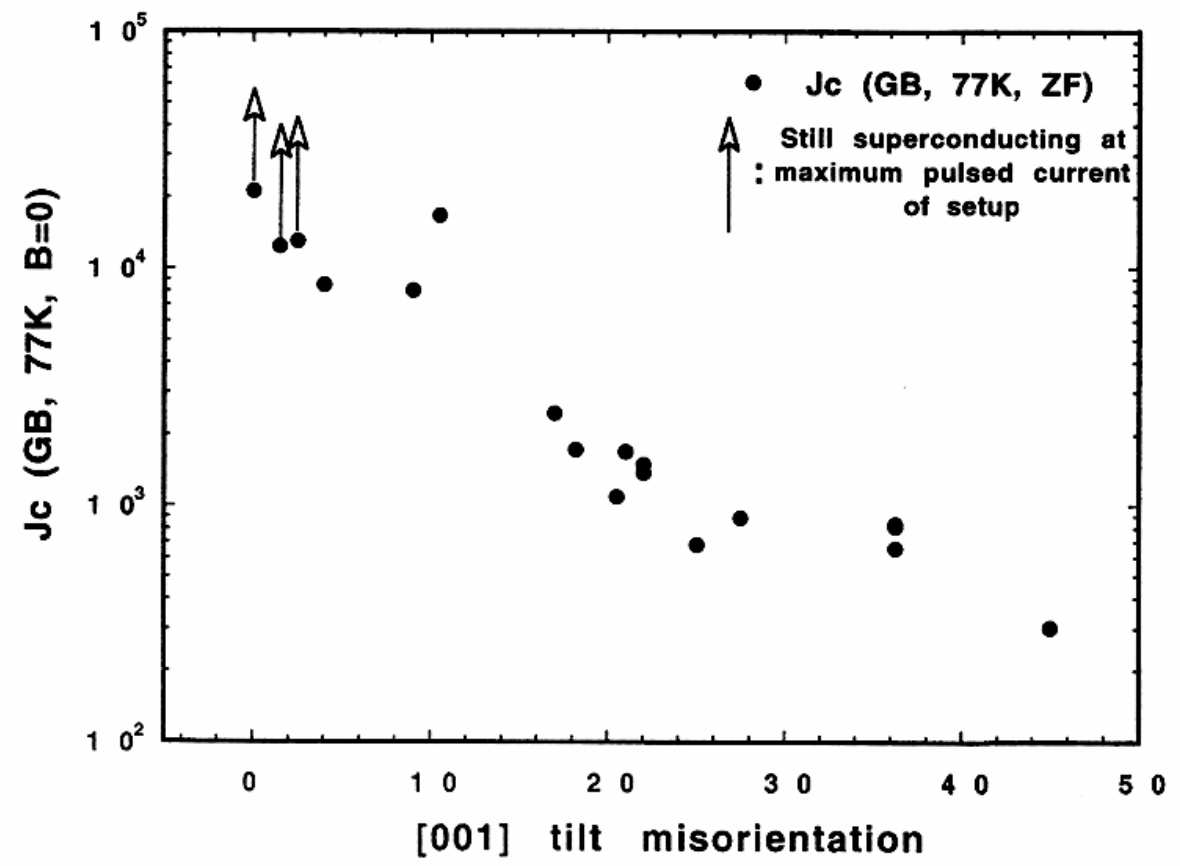
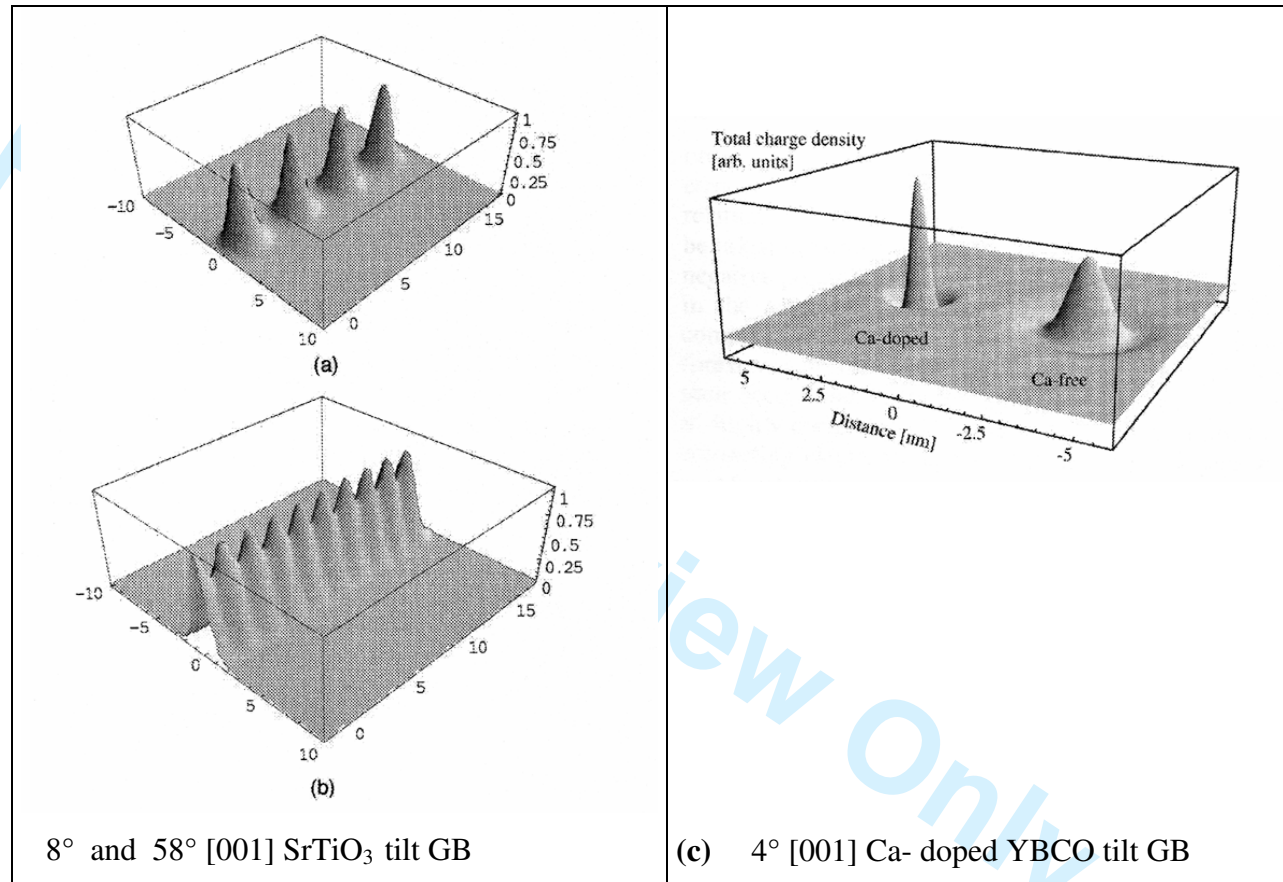


Figure 24

**Figure 25**

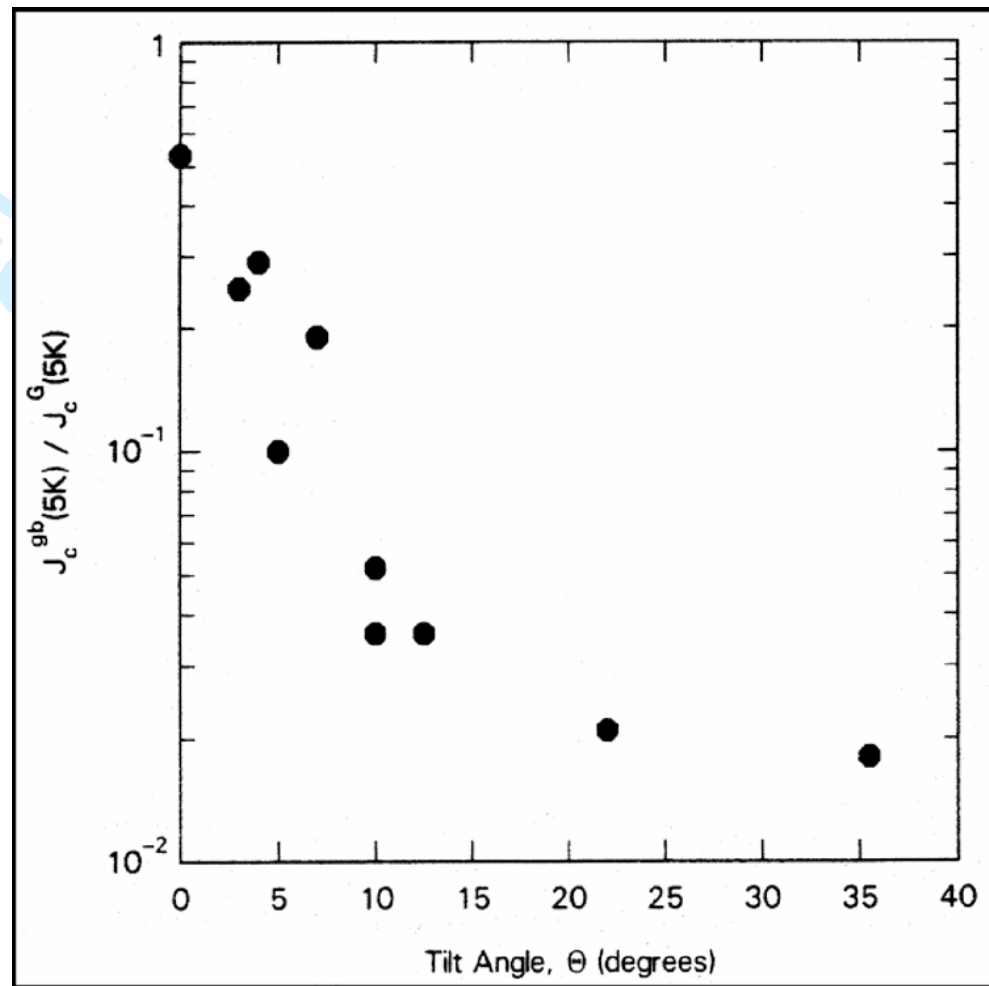


Figure 26

1
2
3
4
5
6
7
8
9
10
11
12
13
14
15
16
17
18
19
20
21
22
23
24
25
26
27
28
29
30
31
32
33
34
35
36
37
38
39
40
41
42
43
44
45
46
47

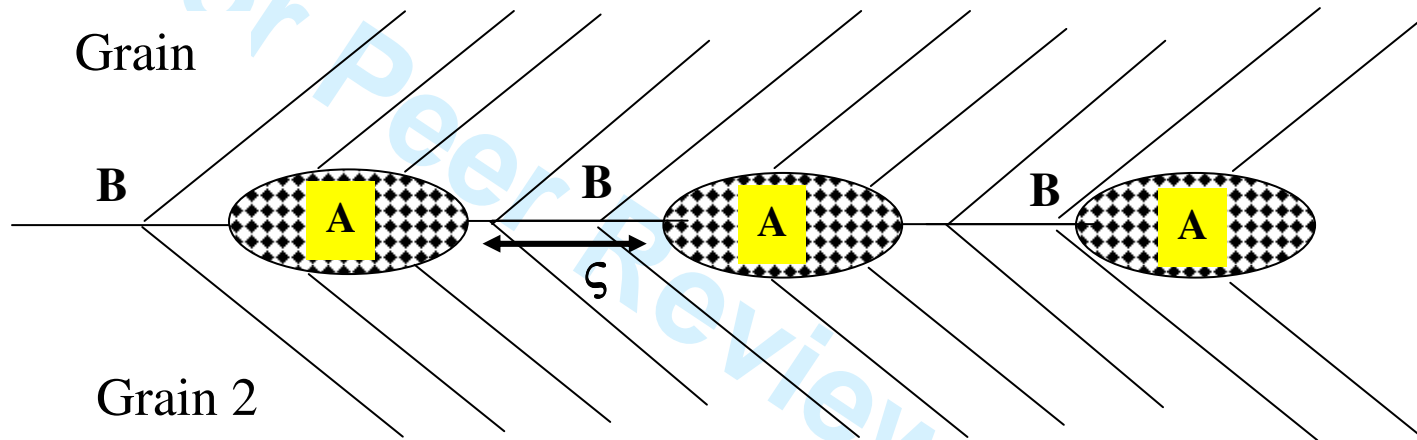


Figure 27

1
2
3
4
5
6
7
8
9
10
11
12
13
14
15
16
17
18
19
20
21
22
23
24
25
26
27
28
29
30
31
32
33
34
35
36
37
38
39
40
41
42
43
44
45
46
47

1
2
3
4
5
6
7
8
9
10
11
12
13
14
15
16
17
18
19
20
21
22
23
24
25
26
27
28
29
30
31
32
33
34
35
36
37
38
39
40
41
42
43
44
45
46
47

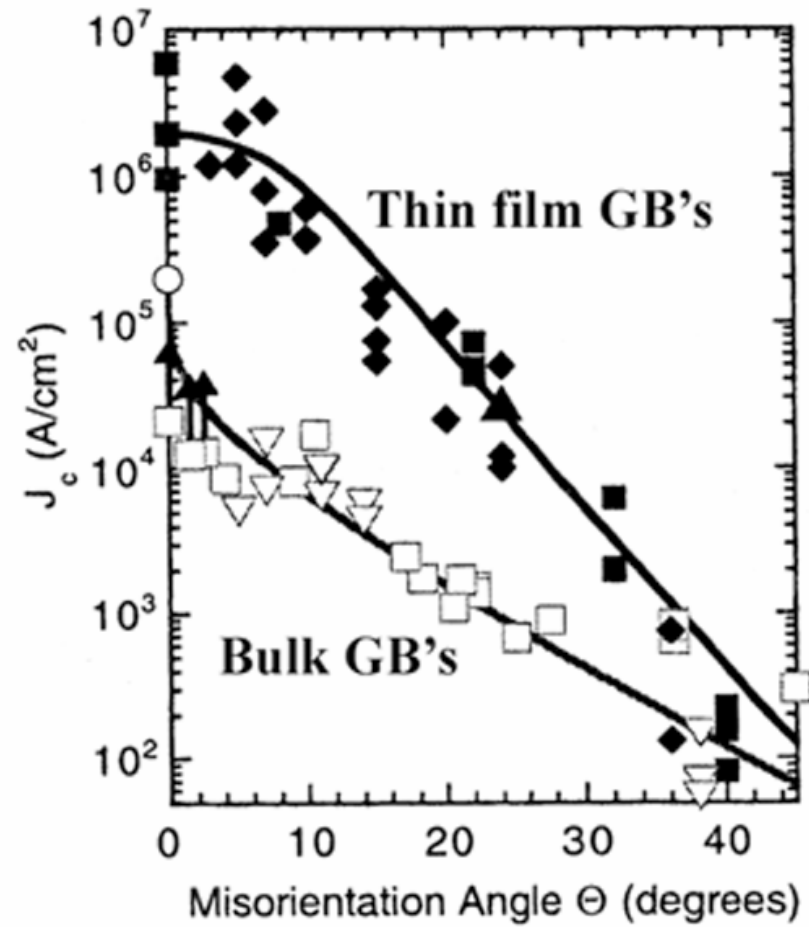


Figure 28

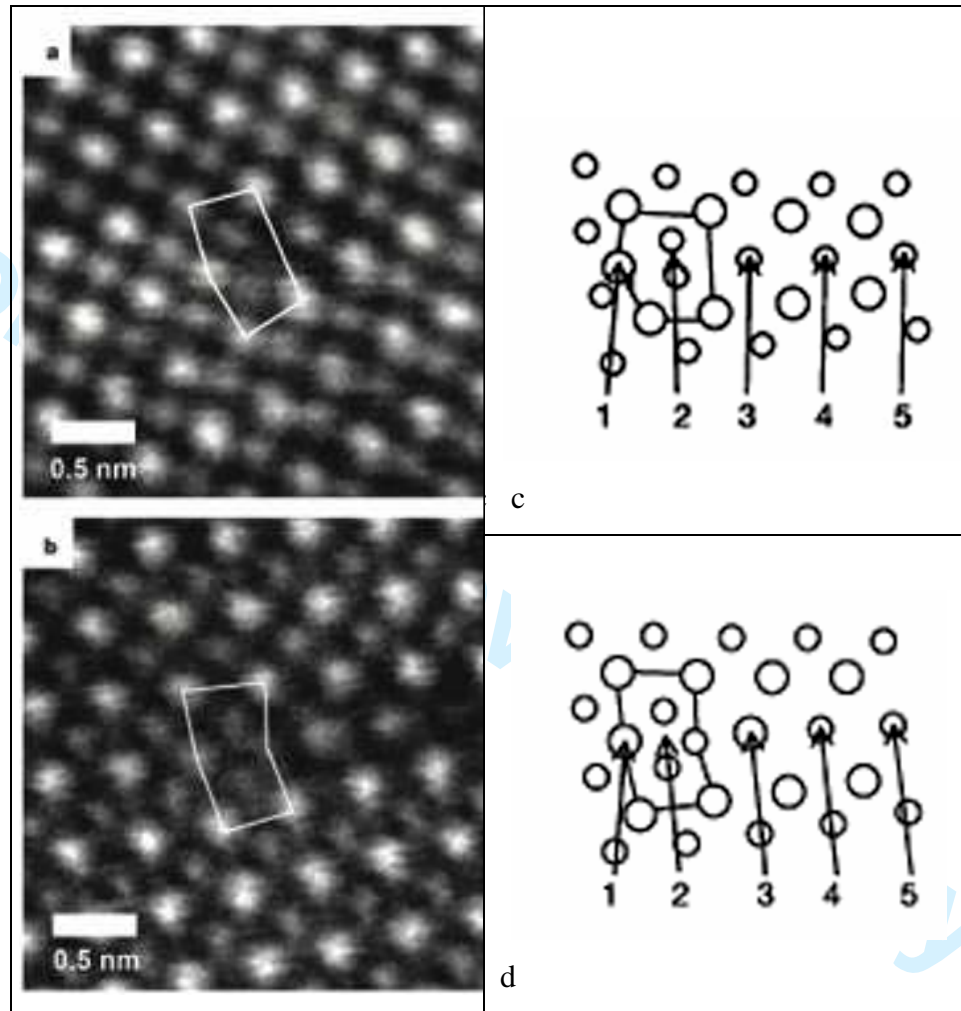
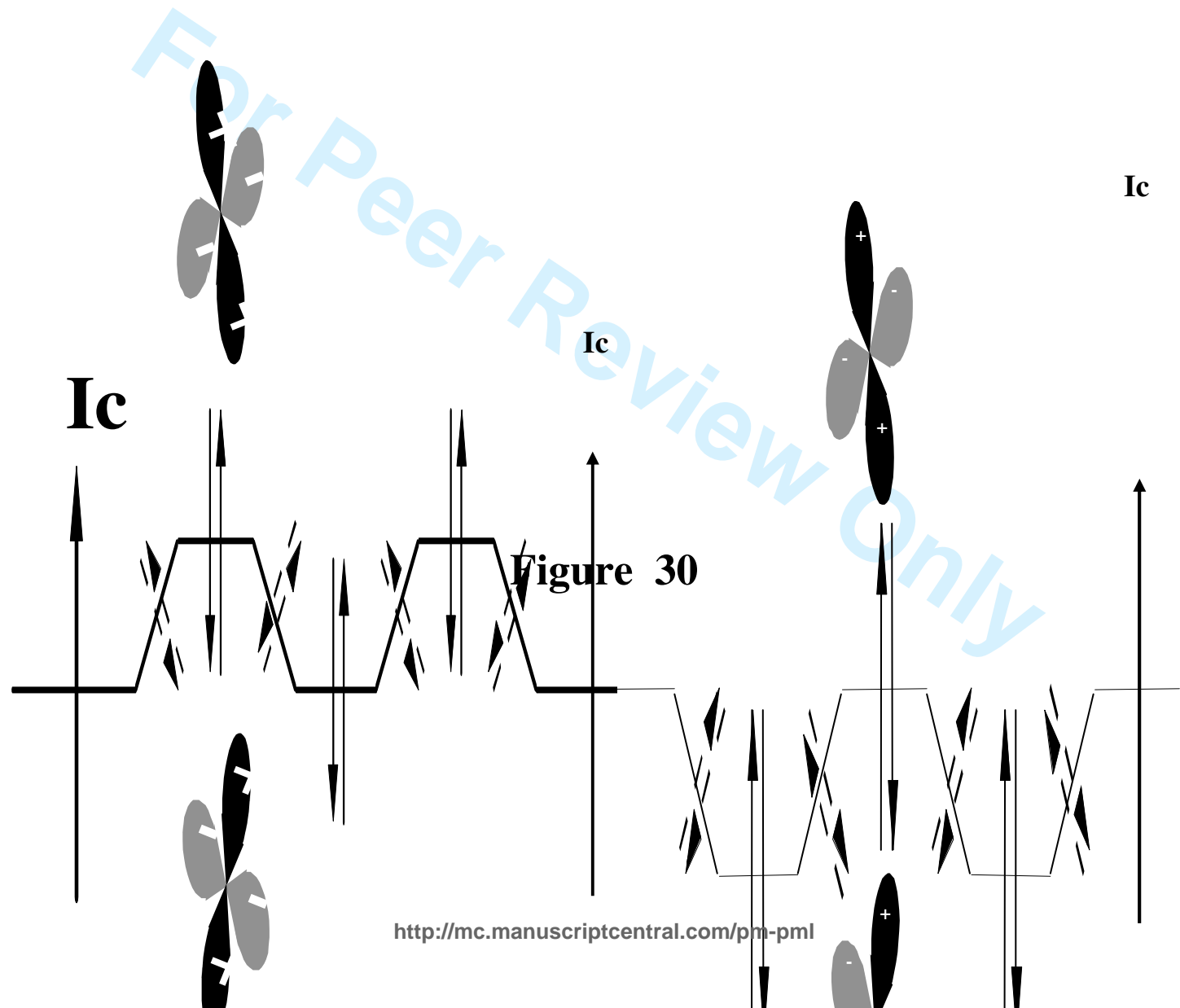
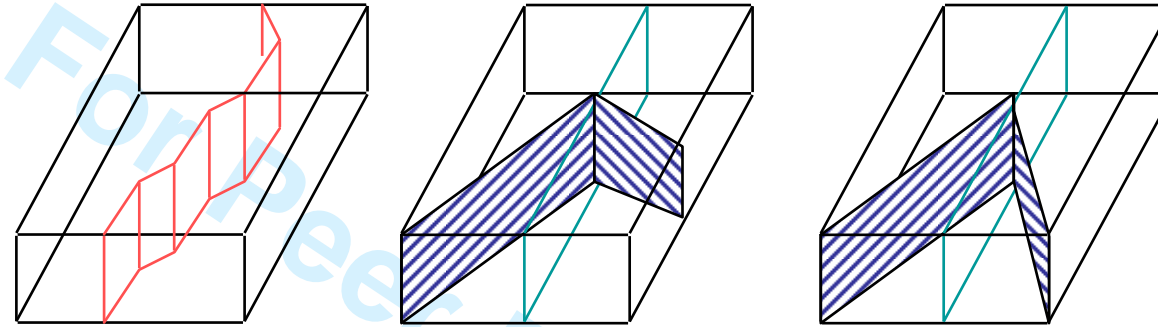


Figure 29

1
2
3
4
5
6
7
8
9
10
11
12
13
14
15
16
17
18
19
20
21
22
23
24
25
26
27
28
29
30
31
32
33
34
35
36
37
38
39
40
41
42
43
44
45
46
47

1
2
3
4
5
6
7
8
9
10
11
12
13
14
15
16
17
18
19
20
21
22
23
24
25
26
27
28
29
30
31
32
33
34
35
36
37
38
39
40
41
42
43
44
45
46
47





**Facetted
GB plane**

Asymmetric GB

Symmetric GB

Figure 31a

1
2
3
4
5
6
7
8
9
10
11
12
13
14
15
16
17
18
19
20
21
22
23
24
25
26
27
28
29
30
31
32
33
34
35
36
37
38
39
40
41
42
43
44
45
46
47

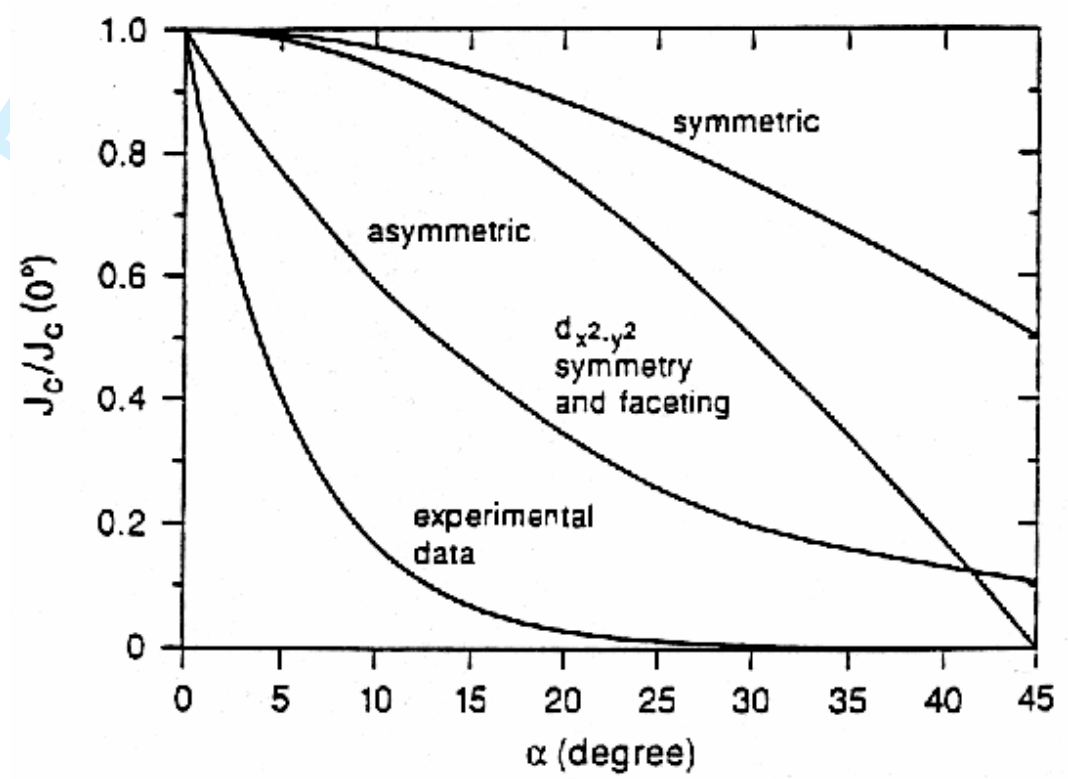


Figure 31b

1
2
3
4
5
6
7
8
9
10
11
12
13
14
15
16
17
18
19
20
21
22
23
24
25
26
27
28
29
30
31
32
33
34
35
36
37
38
39
40
41
42
43
44
45
46
47

YBCO Structures	Oxygen contents	T_c (K)	Lattice Parameters (nm)
Ortho I	O₇ - O_{6.9}	91	a=0.382 b=0.388 c=1.168 + oxygen ordering*
Ortho II	O_{6.97}	maximum T_c=92	
Ortho II	O_{6.6} - O_{6.7}	60	a=b=0.386 c=1.171 + oxygen ordering*
Tetragonal	O_{6.5} - O_{6.4}	0	
*oxygen ordering occurs between O_{6.85} and O_{6.4}			

Table 1

SAMPLES	SUBSTRATES	211 GRAIN SIZES	T _c (K)	Δ T _c (K)	J _c A/cm ² at 77K
D	MgO	<1μm to 5μm	82	13	0 (H//c) ~0
E	Y₂O₃	2μm to >25μm	91,5	1	1.4 10 ⁴ (H//c= 1T) 3.5 10 ⁴ (H//c = 0)

Table 2

YBCO	Type of material	Low angle GB	Large angle GB	Special Σ GB	J _c A/cm ²
------	------------------	--------------	----------------	--------------	----------------------------------

system			<10°		10°<θ< 90°		20°<θ< 90°		
			Clean	Degradated	Clean	Degradated	Clean	Degradated	
Solid-solid diffusion reaction	Bulk classic Ceramic		Yes	No	Some	Some	Some	Some	$J_c < 10^3$
	Thin films grown on single crystal substrate SrTiO ₃ , MgO		Yes	No	Yes	No	Yes	No	$10^6 < J_c < 10^7$
	GB thin film grown on bicrystal SrTiO ₃		Yes	No	Yes	No	Yes	No	$J_c = f(\alpha)$
Solid-liquid diffusion reaction	Single crystal : Twins (110)		-----	-----	-----	-----	Yes	-----	$10^5 < J_c < 10^6$
	Bulk bicrystals		Yes	-----	Yes	-----	Yes	-----	$J_c = f(\alpha)$
	Melt-textured Without substrate	under magnetic field	Some	Some	Some	Some	-----	-----	$10^4 < J_c < 10^5$
	Melt-textured with substrate	Y ₂ O ₃ ceramic	-----	-----	Some	Some	-----	-----	$10^4 < J_c < 10^5$
Y ₂ BaCuO ₅ Ceramic (211)		-----	-----	Some	Some	-----	-----	$10^4 < J_c < 10^5$	
	Single crystal MgO	Some	Some	No	Yes	-----	-----	$J_c \cong 0$	

Table 3

For Peer Review Only

1
2
3
4
5
6
7
8
9
10
11
12
13
14
15
16
17
18
19
20
21
22
23
24
25
26
27
28
29
30
31
32
33
34
35
36
37
38
39
40
41
42
43
44
45
46
47